UNIVERSITY OF CALIFORNIA, SAN DIEGO

Chemical Resonance Effects in Surface-enhanced Raman Scattering of Nucleic Acid-Silver Composites

A dissertation submitted in partial satisfaction of the

requirements for the degree of Doctor of Philosophy

in

Chemical Engineering

by

Lindsay M. Freeman

Committee in charge:

Professor Yeshaiahu Fainman, Chair
Professor Donald Sirbuly, Co-Chair
Professor Sadik Esener
Professor Michael Sailor
Professor Andrea Tao

2016

The dissertation of Lindsay M. Freeman is approved, and it is acceptable in quality and form for publication on microfilm and electronically:

_____

_____

_____

_____

Co-Chair

_____

Chair

University of California, San Diego

2016

DEDICATION

This thesis is dedicated to Dick Freeman, my grandfather.

EPIGRAPH

"Reason, observation, and experience; the holy trinity of science"

-Robert Green Ingersoll

TABLE OF CONTENTS

LIST OF ABBREVIATIONS

Å	Angstrom
AgIFs	Silver island films
ALD	Atomic layer deposition
Al_2O_3	Aluminum oxide
BF	Bright field
CT	Charge-transfer
DFT	Density functional theory
DNA	Deoxyribonucleic Acid
DSM	Double stretching mode
FEM	Finite element modeling
FF	Far field
FM	Fluorescence microscopy
FWHM	Full width at half maximum
HOMO	Highest occupied molecular orbital
LSPR	Localized surface plasmon resonance
LUMO	Lowest unoccupied molecular orbital
NA-Ag	Nucleic acid-silver composites
NF	Near field
NRS	Normal Raman scattering
NSL	Nanosphere lithography
PML	Perfectly matched layer

RBM	Ring breathing mode
RRS	Resonance Raman scattering
RSF	Random silver films
SEM	Scanning electron microscope
SERS	Surface-enhanced Raman spectroscopy
SNR	Signal-to-noise ratio
SPR	Surface plasmon resonance
SRCS	Simulated Raman correlation spectroscopy
SSM	Single stretching mode
TD-DFT	Time-dependent density functional theory
TMA	Trimethylaluminum

LIST OF FIGURES

LIST OF TABLES

ACKNOWLEDGEMENTS

I would like to thank my Ph.D. advisor and mentor, Professor Yeshaiahu Fainman, who has provided me with tremendous support over the past several years. I thank him for giving me the guidance I needed to succeed and the flexibility to pursue my research topic. I would also like to thank my undergraduate advisor, Professor Andrea Armani, who is my inspiration and reason for getting my Ph.D. I would like to thank all of my committee members: Professor Fainman, Professor Sirbuly, Professor Esener, Professor Sailor, and Professor Tao. I am thankful for the support I received from the Ultrafast Nanoscale Optics group, particularly from Dr. Lin Pang who was my mentor during the entirety of my graduate career. I am also thankful for the collaborations I had within my group, including with Brandon Hong, Alexei Smolyaninov, and Janelle Shane.

I am so grateful for the support my friends and family provided to me for the duration of my time in graduate school. My parents, Richard and Danette Freeman, have been amazing supporters my entire life and I could not have completed my journey without them. My sisters, Kristle Freeman Steinberg and Brittany Freeman, have given me the emotional support I needed to succeed. My partner, Elizabeth Kleinschmidt, has been by my side through graduate school and helped me overcome the many challenges that I have faced. Our dog, Sherlock Skywalker, has been a great therapeutic fluffy during times of stress. I am also thankful for my extended family, which has provided me much needed love and care. My grandparents, Dick and Jane Freeman, gave me a second home in California that I am eternally grateful for.

My friends have been incredibly important to my success in graduate school and I am forever appreciative of their presence in my life. I have had so many wonderful moments with my friends from the University of Southern California and UC San Diego that I will never forget. I take comfort in remembering the times I spent with JAATT, the PLL research group, the Burning Kernels, the wolf pack, and the Graduate Student Association. In particular, I want to thank my graduate school friends Josh Villanueva, Jonathan Monk, Mimi Wang, Vineeta Singh, Olivia Simpson, Gregory Wagner, and Matthew Bergman for being there with me for the past 5 years of graduate school. I am also appreciative of the interactions I have had with the students, staff, and faculty here at UC San Diego. The journey has been amazing and I am forever indebted to the great individuals I have crossed paths with.

Chapter 3 and 4, in part, is a reprint that the dissertation author was the principal researcher and author of. The material appears in *Scientific Reports*. (**L.M. Freeman**, A. Smolyaninov, L. Pang, Y. Fainman, "Simulated Raman correlation spectroscopy for quantifying nucleic acid-silver composites" *Scientific Reports*, 6, 23535, 2016.)

Chapter 5 and 6, in part, is a reprint that the dissertation author was the principal researcher and author of. The material appears in *ACS Nano*. (**L.M. Freeman**, L. Pang, Y. Fainman, "Maximizing the electromagnetic and chemical resonances for surface-enhanced Raman spectroscopy of nucleic acids" *ACS Nano*, \8, 8, 8383-8391, Aug. 2014.)

VITA

2010 Bachelor of Science, University of Southern California

2012 Master of Science, University of California, San Diego

2016 Doctor of Philosophy, University of California, San Diego

PUBLICATIONS

L. M. Freeman, A. Smolyaninov, L. Pang, Y. Fainman, "Simulated Raman correlation spectroscopy of nucleic acid-silver composites" *Scientific Reports*, 6, 23535 (2016).

L. Pang, H. M. Chen, **L. M. Freeman**, Y. Fainman, Chapter 8 "Optofluidics", in: Photonics: Scientific Foundations, Technology and Applications, III, John Wiley & Sons, Inc, Hoboken, NJ (2015).

A. Smolyaninov, L. Pang, **L. Freeman**, M. Abashin, Y. Fainman, "Broadband metacoaxial nanoantenna for metasurface and sensing applications", *Optics Express*, **22** (19), 22786-22793 (2014).

L. Pang, **L. M. Freeman**, H. M. Chen, Q. Gu, Y. Fainman, Chapter 14 "Plasmonics in imaging, biodetection and nanolasers" in: Modern Plasmonics, Handbook of Surface Science, North-Holland (2014).

L. M. Freeman, L. Pang, Y. Fainman, "Maximizing the electromagnetic and chemical resonances of surface-enhanced Raman scattering for nucleic acids" *ACS Nano*, **8** (8), 8383-8391 (2014).

L. Pang, H. M. Chen, **L. M. Freeman** and Y. Fainman, "Optofluidic devices and applications in photonics, sensing and imaging" *Lab on a Chip*, **12** (19), 3543-3551 (2012).

L. M. Freeman, A. M. Armani, "Photobleaching of Cy5 conjugated lipid bilayers determined with optical microresonators", *Journal of Selected Topics in Quantum Electronics*, **18** (3), 1160-1165 (2012).

L. M. Freeman, S. Li, Y. Dayani, H-S. Choi, N. Malmstadt, A. M. Armani, "Excitation of Cy5 in self-assembled lipid bilayers using optical microresonators", *Applied Physics Letters* **98** (14), 143703 (2011).

FIELDS OF STUDY

Major Field: Chemical Engineering

Studies in Chemical Engineering and Electrical Engineering

Professor Yeshaiahu Fainman

ABSTRACT OF THE DISSERTATION

Chemical Resonance Effects in Surface-enhanced Raman Scattering of Nucleic Acid-Silver Composites

by

Lindsay M. Freeman

Doctor of Philosophy in Chemical Engineering

University of California, San Diego, 2016

Professor Yeshaiahu Fainman, Chair

Professor Donald Sirbuly, Co-Chair

Although surface-enhanced Raman spectroscopy (SERS) has been a valuable tool for chemical detection, the understanding of the contributions of the chemical enhancement effect in nucleic acid-silver composites remains limited. Nucleic acid-silver composites have unique optical properties such as fluorescence and enhanced Raman generation, and thus need to be further analyzed and characterized.

In this dissertation, the static polarizability chemical effect is used to determine the preferential binding sites of nucleic acids to silver nanoparticles. The binding configuration dictates the optical properties, so it is imperative to determine which atoms are binding to the silver structures. Time-dependent density functional theory simulations are used to calculate the Raman frequencies of several systems and are then quantitatively compared to experimental measurements. The approximate composition of the binding sites for each nucleic acid to silver films is determined using the simulated Raman correlation spectroscopy process.

In the second part of the dissertation, the charge-transfer effect in nucleic acid-silver composites is harnessed in order to selectively enhance or reduce the SERS signals via wavelength selection. Depending on the molecular properties of the nucleic acids, the optimal excitation wavelength shifts from visible to near-infrared. The properties can be taken advantage of to better control the systems under study. The charge-transfer effect is further understood by utilizing a thin film of aluminum oxide to prevent electron transfer from occurring, and thus enabling the calculation of the order of magnitude of the charge-transfer effect.

The characterization of nucleic acid-silver composites is imperative to fully understanding the unique and exciting properties that these systems provide. While SERS has been limited in terms of DNA detection or sequencing, the restrictions have been caused by insufficient information. This dissertation offers additional information on the systems and explains the discrepancies seen in previous measurements of nucleic acid-silver composites.

Chapter 1

Introduction

1.1. Plasmonics

The field of nanoscience, arising from the intersection of chemistry, material science, and engineering, has become incredibly well-studied in the past 20 years and contributed to vapid growth in the areas of biosensing [1–3], energy storage [4,5], telecommunications [6,7], and light manipulation [8,9]. Biosensing, which has been previously dominated by traditional methods such as enzyme-linked immunosorbent assay [10] and fluorescence probing [11], has experienced a surge in interest of alternative methods as researchers have looked for sensitive and specific detection techniques that do not rely on fluorophores or other bulky labels. Nanoengineered materials and devices offer tremendous potential in the advancement of novel biosensing and chemical detection methods.

A particularly intriguing field under study for the advancement of sensors is plasmonics, in which surface plasmons generate strong, localized electromagnetic fields on the surface of nanometallic structures [12]. Surface plasmons are electron oscillations at the interface of a dielectric (e.g. air) and metal (e.g. gold, silver) with the systematic properties, such as dielectric constants and geometrical shape, determining how the surface plasmons move. The discovery of surface plasmons and thus the field of plasmonics has generated significant interest due to the ability to control and manipulate light [9]. In terms of biosensing, plasmonics has led to the exploration and implementation of surface plasmon resonance (SPR) sensing [13,14] and surface-enhanced Raman spectroscopy (SERS) [15,16], two applications that have had a tremendous impact on chemical detection. In this dissertation, we explore the

chemical enhancement effect of SERS as it pertains to nucleic acid-silver composites. Nucleic acid-silver composites have demonstrated unique and exciting optical properties [17], and here we seek to further understand their tremendous potential.

1.2. Motivation

The foundation for plasmonics and its application of SERS has been steadily built the past 40 years, with interest in SERS skyrocketing the past 20 years as more efficient nanoscale materials are designed specifically for SERS [18]. SERS was discovered in the late 1970's when electrochemically roughened metal electrodes generated massive Raman scattering enhancement [19–21], paving the way for improved Raman signal detection. Because Raman scattering is the inelastic scattering of light when photons interact with molecules, the resulting signal is inherently weak and difficult to detect. The identification of Raman enhancement in SERS immediately became of great interest due to its potential, eventually demonstrating single-molecule detection [22,23] and real-time biological sensing [24]. However, the field of SERS has always been immersed in some controversy due to the various enhancement effects present in the phenomenon, including the electromagnetic [25] and chemical enhancement effect [26]. Because of the various parameters and factors that affect the enhancement of the Raman signal, there has been extensive discussion on the multiple enhancement mechanisms and how they are interrelated.

While the majority of SERS publications are focused on the electromagnetic enhancement effect caused by the localized surface plasmons, a smaller subset of SERS research is on the chemical enhancement effect. The electromagnetic effect is

responsible for the most significant order of magnitude enhancement (~10^4-10^8), while the chemical enhancement effect, less impactful at order of magnitude enhancement (~10-10^3), has often been overlooked due to its complexity. Despite the favoritism towards studying the electromagnetic enhancement effect, the chemical enhancement effect is incredibly important due to its dependence on the molecular and electronic structure. Thus, fully understanding the consequences of the chemical enhancement effect is crucial to realizing the complete potential of SERS.

When SERS was first initially observed, the cause of the Raman signal enhancement was not immediately identified. During the 1980's, two theories predominantly emerged: the electromagnetic enhancement and the chemical enhancement. The electromagnetic enhancement theory is based on the knowledge of surface plasmons and explains the massive Raman signal enhancement as a result of the localized electromagnetic fields confined within nanoscale metallic structures. The chemical enhancement is an increase in the Raman signal caused by chemical effects, including charge-transfer, molecular resonance, or static polarizability. Upon further review, it became known that both effects have a considerable impact on the resulting Raman signal, with the electromagnetic effect leading to greater enhancement. However, the chemical effect is still very important because the chemical effect selectively increases or decreases the Raman signal depending on the molecule, and thus can be harnessed to gain a greater understanding of the system under study. This important realization has led to many developments in utilizing the chemical enhancement effect to its full abilities, such as when metal-molecule-metal

nanosystems were fabricated to enable tunneling of the charge-transfer to achieve maximum overall SERS enhancement [27].

The importance of the chemical enhancement has led to several advancements in the past decade. Researchers have been interested in understanding how the chemical enhancement varies among system to system, and how the individual chemical enhancement effects (charge-transfer, static polarizability, and molecular resonance) determine the experimental outcomes. Some notable, recent advances include the work of Sun *et al.* who visualized the charge-transfer mechanism in SERS and tip-enhanced Raman spectroscopy (TERS) [28] and of Schatz *et al.* who calculated the approximate static chemical enhancement for benzene functionalized to silver and gold [29]. Another exciting area is analyzing the chemical enhancement effect during single-molecule SERS (SM-SERS) experiments. Salvarezza *et al.* recently showed the dependence of the SM-SERS signal on the reduction and oxidation electrochemical cycles and discussed the effect of changing the electron tunneling distance [30]. The chemical enhancement effect can yield a tremendous amount of essential information, and its potential is now being realized.

As discussed, the chemical enhancement effect plays a critical role in experimentally measured Raman signals. Of particular interest in this dissertation is the chemical enhancement effect of nucleic acid-silver composites (NA-Ag). These systems are extremely interesting due to their unique optical properties in the visible range. For example, silver nanoparticles that have been functionalized with DNA strands have fluoresced at visible excitation wavelengths despite DNA strands having

fluorescence absorption and emission in the ultraviolet range [31,32]. The fluorescence is caused by the charge-transfer between the molecular orbitals of the nucleic acids and the silver particles, generating new electronic transitions in the visible range. The modulation of these electronic properties are of interest in the application of SERS, in which the excitation wavelength can have a unique interaction with the NA-Ag systems that leads to enhanced or reduced Raman intensity modes. The focus of this dissertation is to exploit the optical and electronic properties of these systems and understand how the chemical enhancement of SERS can be implemented to further advance the knowledge of such systems.

1.3. Outline of Dissertation

This dissertation begins with a review of Raman scattering and an elaborate description of the multiple effects of SERS in Chapter 2. The fundamentals of Raman scattering are explored with a Jablonski diagram. The electromagnetic effect is explained in terms of the Mie scattering theory, with a detailed outline of Maxwell's equations. The chemical enhancement effect is categorized by charge-transfer, static polarizability, and molecular resonance and each are further explained. A brief description of previous work on SERS of NA-Ag systems is provided.

Chapter 3 begins with an explanation of the static polarizability effect of SERS and how the polarizability of the system has an impact on the resulting Raman signal. The chapter introduces time-dependent density functional theory (TD-DFT) as it pertains to Raman mode intensity calculations. The importance of the Raman static polarizability as it pertains to NA-Ag systems is highlighted by simple simulations.

Several NA-Ag systems are then analyzed for each nucleic acid (adenine, cytosine, guanine, and thymine), with multiple binding sites of each nucleic acid selected to bind to a silver nanoparticle structure. Raman frequency mode calculations are performed and shown for each system and are directly compared to experimental Raman measurements of nucleic acids functionalized to silver films.

The simulated Raman correlation spectroscopy (SRCS) process is introduced in Chapter 4, in which the TD-DFT Raman simulations are quantitatively compared to experimental measurements. The Raman data are applied in order to determine the composition of the preferential binding sites for each system. The SRCS process is described in detail and demonstrates excellent correlation when applied to NA-Ag systems.

Beginning in Chapter 5, the charge-transfer effect is implemented to generate differing chemical enhancement factors for two systems: Cytosine-Ag and Guanine-Ag. Two excitation wavelengths are experimentally used for Raman measurements to preferentially enhance the Raman signatures of one system over the other. The generation of the electronic transitions is confirmed by absorption spectroscopy measurements and the corresponding simulations.

Chapter 6 further demonstrates the effect the charge-transfer effect has on NA-Ag systems, in which an atomic layer of aluminum oxide is used to eliminate electron transfer from occurring. The prevention layer removes the chemical enhancement for the systems, and supports the findings in Chapter 6 that there is a wavelength dependence on NA-Ag systems.

Chapter 7 concludes the dissertation with a discussion of the research findings and the future direction of this work. Areas of interest for future work include implementing the SRCS process for understanding binding dependence on concentration and using the charge-transfer resonance to analyze DNA strands.

Chapter 2

Background on Raman Spectroscopy

2.1. Raman Spectroscopy

There is an array of methods that exist for chemical analysis, including fluorescence microscopy [33–37], ultraviolet visible spectroscopy [38–42], infrared spectroscopy [43–46], and Raman spectroscopy [47–51]. While fluorescence and ultraviolet visible spectroscopy offer strong signals with high signal-to-noise ratios and ease of data acquisition, the extremely broad full width half maximum (FWHM) of the signals limits the accuracy of the identification. Infrared absorption spectroscopy has narrow mode profiles and thus is better for chemical identification, but is dependent on the dipole of the molecule and thus cannot identify diatomic molecules [52]. Raman spectroscopy offers a highly accurate method of chemical analysis with unique molecular fingerprint identification [53]. With the discovery of plasmonic enhancement for SERS [19–21], Raman spectroscopy began to fulfill its potential as an informative spectroscopy method. In this chapter, the background of Raman spectroscopy and SERS is discussed, followed by an explanation of the electromagnetic and chemical enhancement effects and their relation to nucleic acid-silver composites.

Raman scattering is a phenomenon caused by inelastic light scattering off of a molecule, in which photons interacting with the molecule either lose (Stokes) or gain (Anti-Stokes) energy based on the molecular structure. Raman scattering was discovered by Nobel Laureate C.V. Raman in 1928 when he demonstrated that violet light scattering with liquid emits both violet light (Rayleigh scattering) and green light (Raman scattering) [54,55]. The vast majority of photons, when interacting with the

liquid droplets, were elastically scattered at the same incident wavelength. However, a small portion of the photons, approximately one in ten million, were inelastically scattered at a different wavelength. Raman recognized that the shift in wavelength is dependent on the molecular composition of the liquid droplet, and thus information could be extracted by monitoring this energy change. Eventually, this powerful tool was harnessed in order to identify chemicals in the form of Raman spectroscopy, as the photonic interaction with molecules and corresponding inelastic scattering yields powerful information about the molecule of interest.

The Raman effect can be described by a Jablonski diagram as shown in Figure 2.1. As incident light interacts with the molecule, the molecule is excited to a virtual state. Generally, the molecule relaxes back down to the ground state and thus emits photons at the same incident wavelength. However, the molecule can also relax to a rotational and vibrational energy state that is higher than the ground state level, and thus emits photons with longer wavelengths (Stokes shift). Additionally, the molecule can occasionally be in a higher rotational and vibrational state before excitation, and the interaction with photons excites the molecule to a virtual state and then relaxes to the ground state level. In this case, energy is gained from the higher vibrational state to the ground state and the molecule emits photons with shorter wavelengths (Anti-Stokes shift).

The changes in energy contain unique and rich information pertaining to the molecular structure, as the change can be measured as a frequency shift from the incident energy. Molecules have several unique vibrational frequency modes

depending on the molecular bond lengths, strengths, and angles, and so measuring these changes in frequency yields a molecular fingerprint that can be used for chemical identification. Raman scattering is dependent on the induced dipole, in which the dipole moment (μ) can be defined as:

$$\mu = \alpha E \qquad (2.1)$$

where α is the polarizability of the molecule and E is the applied electric field. As an electric field is applied to a molecule, the electrons surrounding the atoms can be distorted and cause an induced dipole. When a molecule is then excited by an incident electromagnetic field, the induced dipole scatters light at an optical frequency

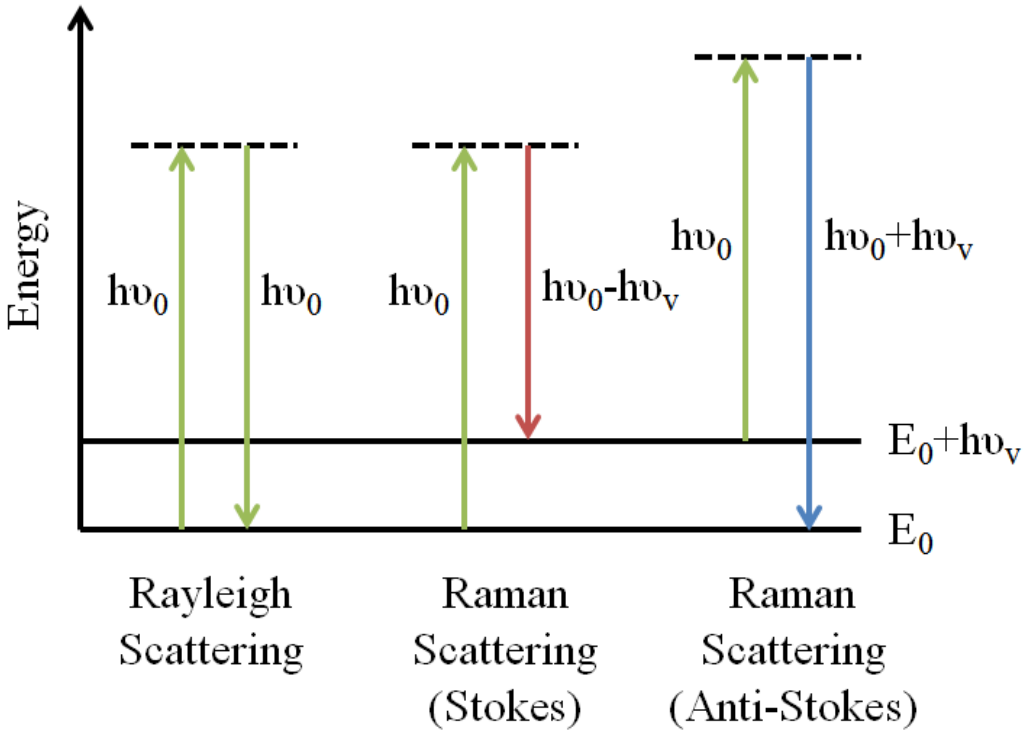

Figure 2.1. Jablonski Diagram of Rayleigh and Raman scattering. Energy diagram showing Rayleigh (elastic) scattering and Raman (inelastic) scattering. The two types of Raman scattering, Stokes and Anti-Stokes, are shown.

dependent on the polarizability and internal motion of the molecule, generating additional frequencies. The change in polarizability during the vibration can be defined as:

$$\frac{d\alpha}{dQ_i} \neq 0 \qquad (2.2)$$

where Q is the normal coordinate of the vibrational mode i. Thus, for a vibrational mode to be Raman active, there must be a change in the polarizability of the frequency mode. The intensity of an active Raman band is a function of the polarizability derivative, in which a greater change in the polarizability of the mode produces a higher Raman intensity. Thus, the Raman signature is a description of the various

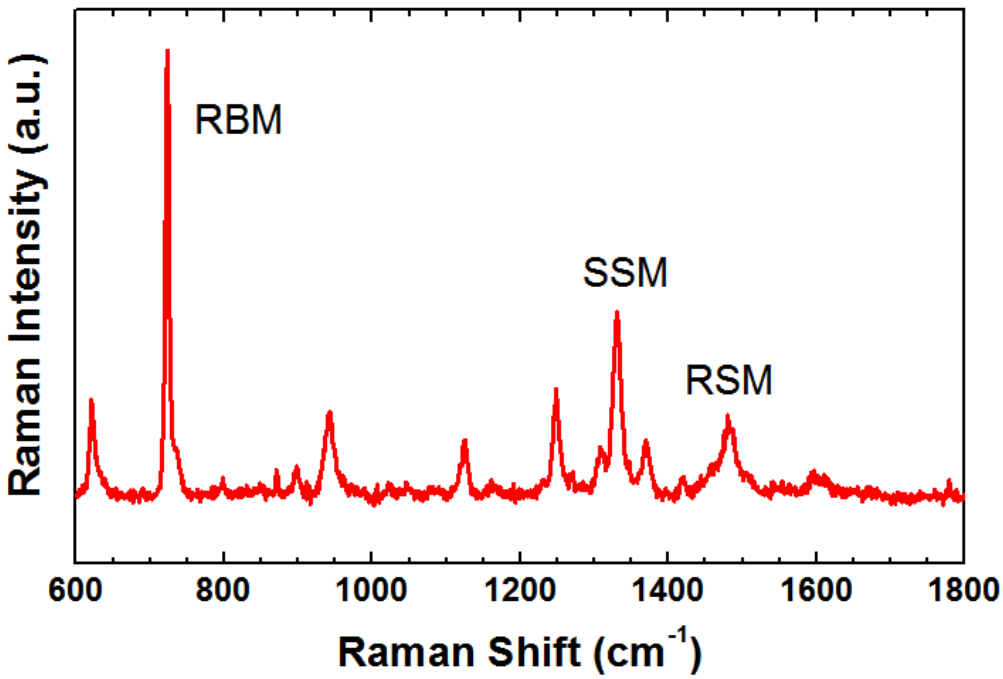

Figure 2.2. Raman frequency modes of adenine. Raman spectrum of bulk adenine powder with the ring breathing mode (RBM), single stretching mode (SSM) and ring stretching mode (RSM) labeled.

Raman frequency modes and their corresponding intensities. As an example, the normal Raman scattering (NRS) spectrum for bulk powder of adenine can be found in Figure 2.2.

In this Raman spectrum for adenine, the spectral peaks represent the unique molecular frequency modes. The intensities of each mode correspond to the strength of the frequency mode, with mode enhancement dependent on factors such as polarizability. For adenine, strong frequency modes include the ring-breathing-mode (RBM, ~725 cm^{-1}), the single stretching mode (SSM, ~1335 cm^{-1}) and the ring stretching mode (RSM, ~1485 cm^{-1}). The intensity of these modes provide the molecular fingerprint for adenine, and enables the characterization of adenine by analyzing this spectrum.

The necessity to understand molecular structure has enabled consistent growth in the field of Raman spectroscopy, as the spectroscopic method led to significant scientific findings including the characterization of diamond films [56,57], understanding of phonon interactions in graphene [58,59], and detection of chemicals [60,61]. However, while this technique offers many benefits, Raman spectroscopy has remained limited due to the stringent experimental requirements. When photons interact with a molecule, the majority are elastically scattered at the same energy as the excitation light resulting in extremely low signals that were difficult to detect and required expensive equipment. Due to the difficult nature of Raman signal acquisition, the technical field experienced significant friction and

became underutilized until the discovery of surface-enhanced Raman spectroscopy (SERS).

2.2. Surface-enhanced Raman Spectroscopy

Surface-enhanced Raman spectroscopy (SERS) was discovered in the late 1970's [19–21] as an improved version of Raman spectroscopy, in which nanoscale metallic materials that support surface plasmons enable massive field enhancement of the local electromagnetic field [25]. The first demonstration of SERS was on roughened metal surfaces, in which massive Raman signal enhancements of pyridine were found on silver electrodes [62]. While the original mechanism of SERS was not immediately well understood, the interest in Raman spectroscopy experienced a dramatic increase as measurable Raman signals on low concentrations became realized. The discovery reduced the need for idealistic and expensive experimental equipment and simplified the process for measuring Raman signals. The SERS spectrum of guanine, in comparison to the normal Raman spectrum (NRS) of the isolated molecule, is shown in Figure 2.3.

Though the highly impactful findings of SERS generated great interest in the field, the mechanism behind SERS was not initially clearly understood. Thus, various groups sought to fully understand the physical phenomenon causing the Raman signal enhancement and explain the dramatic increase in photons that were being measured. Two mechanisms were proposed: electromagnetic enhancement and chemical enhancement. The electromagnetic enhancement is caused by the surface plasmons

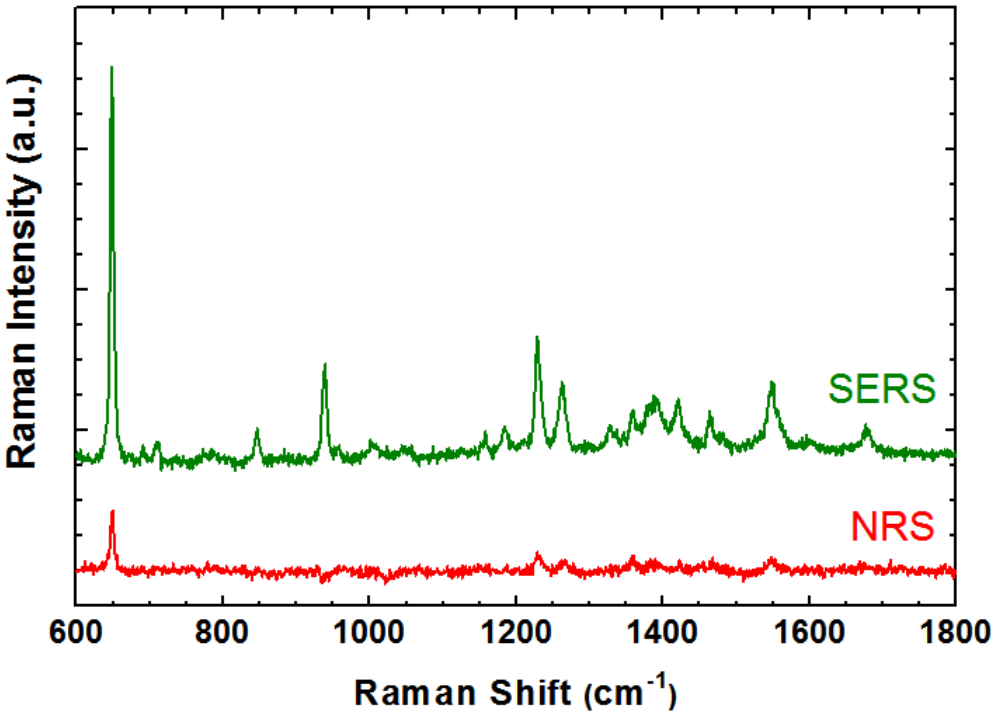

Figure 2.3. SERS and NRS of guanine. The surface-enhanced Raman spectrum on and normal Raman spectrum of guanine, showing enhancement caused by the electromagnetic enhancement of silver island films.

propagating on the nanometallic devices, in which matching the plasmonic frequency localizes the collective oscillations of surface plasmons [12]. By focusing the intensity of light into a very small volume at the location of the molecules, the inelastic scattering signals can be greatly enhanced without increasing laser power.

Additionally, researchers discovered a chemical enhancement caused by the charge-transfer effect. The charge-transfer effect is when electrons transfer from the metallic surfaces to the orbitals of the molecule, creating electronic transitions that can be excited when the energy is resonant with the band gap [63]. The energy difference between the highest occupied molecular orbital (HOMO) and lowest unoccupied

molecular orbital (LUMO) is relatively high for isolated molecules (~4 eV), and thus needs ultraviolet light to excite the electronic transition. However, the interaction between the HOMO and LUMO of the molecule with the Fermi level of the metal surface creates a new electronic transition that requires less energy to excite, leading to a resonance effect in the visible to near-infrared wavelength range.

2.3. Electromagnetic Enhancement

Plasmonic devices offer many unique and beneficial attributes, including their ability to generate the electromagnetic enhancement in SERS experiments. The original SERS experiments were performed on roughened electrodes [20,64,65], which are surfaces that support localized surface plasmon resonances (LSPR) due to their nanoscale metallic features. Additional SERS substrates include silver or gold nanoparticles [66–68], bowties [69], metacoaxial nanoantennas [70], and spherical nanoshell structures [71]. Here, we detail the mechanisms responsible for the electromagnetic enhancement effect in SERS experiments and how the dielectric constants and geometrical structures determine the localized field.

The electromagnetic enhancement is a result of the plasmonic resonance in nanoscale metallic materials, in which incident light excites localized surface plasmons on the surface of the metal. To support surface plasmon excitations, the metal must have specific dielectric properties which are commonly found in coinage metals such as silver and gold. The dielectric function is defined as:

$$\epsilon(\omega) = \epsilon_{\infty}\left(1 - \frac{\omega_p^2}{\omega^2 + i\gamma_0\omega}\right) \qquad (2.3)$$

where ϵ is the dielectric function of the metal, ϵ_∞ is the dielectric function of the surrounding material, ω is the excitation frequency, ω_p is the plasmon resonance frequency, and γ_0 is the damping coefficient. The real and imaginary parts of the dielectric function can be defined as:

$$Real[\epsilon(\omega)] = \epsilon_\infty(1 - \frac{\omega_p^2}{\omega^2+\gamma_0}) \qquad (2.4)$$

$$Imag[\epsilon(\omega)] = \frac{\epsilon_\infty \omega_p^2 \gamma_0}{\omega(\omega^2+\gamma_0^2)} \qquad (2.5)$$

To match the plasmon resonance frequency, the ideal conditions are to have a negative large real dielectric function and a small imaginary dielectric function ($Imag[\epsilon(\omega)]$~0). Thus, gold and silver are ideal plasmonic materials because, in the visible wavelength range, they have a large, negative real part of the dielectric function and a small imaginary dielectric function. In addition to gold and silver, the metal aluminum can support surface plasmons in the ultraviolet excitation range due to its dielectric properties. In addition to the dielectric properties, the size of the features dictates whether or not the material supports surface plasmons, in which the size of the sphere must be smaller than the excitation light wavelength. Thus, nanoscale gold and silver devices are ideal SERS substrates for optimal electromagnetic enhancement.

The other factor for determining electromagnetic field enhancement for optimal surface plasmon propagation is geometrical shape. There are two main geometrical features that promote the highest localized field: the coupling effect and lightening rod effect. The coupling effect is caused by multiple nanometallic shapes

that couple light in between each other, with the electric field scaling with a decrease in the gap between the two shapes. The other effect, the lightening rod effect, is caused by plasmons localizing at sharp and narrow tips of nanoscale materials.

Based on the electromagnetic field enhancement mechanisms, ideal SERS substrates have sharp, narrow features and closely packed arrays. The bowtie structure, in which two triangles couple between each other in a bowtie formation, have shown to detect single molecule fluorescence based on their massive signal enhancement. Silver island films, as shown in Figure 2.4, have similar features in which triangular prisms couple photons between each other.

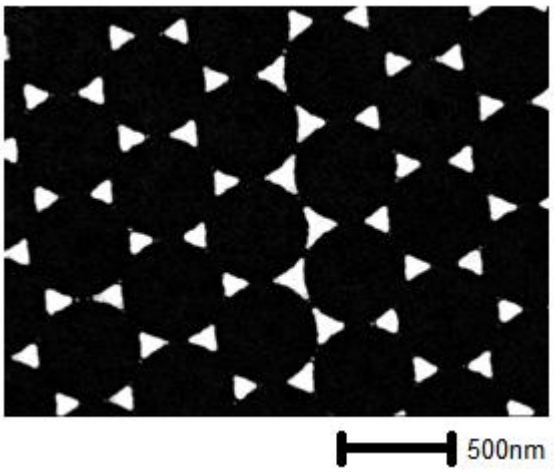

Figure 2.4. SEM of AgIFs. Scanning electron microscope image of silver island films that have high electromagnetic field enhancement.

These SERS substrates have paved the way for exciting and revolutionary discoveries, including using SERS to map the electromagnetic enhancement of metal films [72], detect self-assembled monolayers (SAMs) [73], and image cancer cells [74]. The electromagnetic effect of SERS has had a profound impact on the field

of Raman spectroscopy, enabling significant advancement in chemical sensing and biodetection. Despite the many accomplishments in the field, research is still on-going to find more effective and efficient SERS substrates that are easily fabricated and offer consistent enhancement.

2.4. Chemical Enhancement

While the majority of research in SERS has been focused on the electromagnetic effect, there is an additional chemical effect that generates enhancement by exciting the electronic transitions formed by the transfer of electrons between the metal and the molecules. Because the chemical effect leads to an enhancement of approximately 10 to 10^3 compared to the electromagnetic enhancement of 10^4 to 10^8 [25,75], the chemical resonance has often been overlooked. However, the chemical enhancement becomes particular important because of its dependence on molecular structure as the electromagnetic enhancement is chemically non-selective. For example, the SERS enhancements of nitrogen and carbon monoxide gas adsorbed to identical metal surfaces have been reported to differ by a factor of 200. Therefore, the chemical enhancement can be utilized to further understand the systems under study when controlling and accounting for the electromagnetic contribution.

The enhancement generated by chemical attributes is composed of three effects: the charge-transfer effect, static polarizability, and molecular resonance. The processes provide cumulative chemical enhancement to reach an order of magnitude up to 10^3. The charge-transfer effect is the resonance effect occurring when the

excitation wavelength matches the resonance of the electronic transitions generated by the transfer of charge between the molecules and metal. The static polarizability effect is a nonresonant mechanism that is dependent on the molecular adsorption configuration to the surface. The molecular resonance is similar to the charge-transfer effect, but rather is when an excitation wavelength matches the inherent molecular resonance of the molecule.

The charge-transfer effect is the most commonly cited chemical enhancement effect and has taken the majority role in SERS research. The effect is caused by the electron transfer between the molecular orbitals of the metal and of the molecule of interest [63,76,77]. The electron transfer modulates the bandgap of the system, generating electronic transitions in the visible or near infrared range. By exciting the system with energy resonant with the charge-transfer electronic transitions, a chemical enhancement is produced. The effect has been utilized to detect the Raman signal of a single molecule by fabricating a geometry in which a single molecule is functionalized in between a gold film and gold nanoparticle. The charge-transfer enhancement occurred only for the isolated molecule, while the other molecules remained inactive from the charge-transfer resonance. Thus, the SERS signal was a product of a single molecule caused by the charge-transfer resonance [78].

The static polarizability chemical enhancement effect, in which the molecular orientation of a molecule designates Raman modes to either be amplified or reduced, has also been studied in SERS research. The static polarizability effect is dependent on the adsorption properties of the molecule to the metal and determines the resulting

enhanced Raman signal. Previously, this effect has been employed to detect the chemical transformation of *para*-Aminothiophenol functionalized to silver electrodes, as the measured SERS signal was sensitive to the surface reaction of the electrodes [79]. Similarly to the charge-transfer effect, the chemical enhancement of 10 to 10^3 is dependent on the molecular properties of the system and can be tuned accordingly.

The third chemical effect is based on the inherent properties of the molecule, such that an excitation energy is selected to excite the natural molecular resonance of the molecule itself. Termed surface-enhanced resonance Raman spectroscopy (SERRS), the process consists of molecules with strong absorption in the visible and near-infrared range, such as dyes, that are able to produce massive Raman signal enhancement when the excitation wavelength is tuned to match the absorption of the molecule. SERRS has been responsible for achieving extremely high enhancement factors when detecting dye molecules, as dye molecules such as Rhodamine 6G can be excited by visible light [80].

2.5. SERS Chemical Effect for Nucleic Acids

Nucleic acids are of particular interest in SERS, as SERS has long been expected to be a label-free identification probe of nucleic acid sequences given that a large number of SERS substrates with consistent local field enhancements for improved chemical detection have been designed and fabricated (metal nanoparticles, [23,81,82] nanoplasmonic resonators, [83–85] *etc.*). Additionally, researchers were able to detect a single molecule of adenine with SERS in 1998 [86],

demonstrating label-free single molecule detection with single molecule SERS (SM-SERS). In addition to the work of SERS of nucleic acids and DNA strands, there has been a significant amount of research on nucleic acids functionalized to silver nanoparticles. Nucleic acids bound to nanoscale metallic devices have produced unique and interesting plasmonic properties that make them ideal SERS systems to study in this dissertation.

Initial interest in nucleic acids functionalized to silver nanoparticles was generated by the discovery that the systems produced fluorescence, despite neither isolated silver nanoparticles or nucleic acids inherently having fluorescent properties. By attaching DNA strands to silver nanoparticles, researchers found that the fluorescence was dependent on the DNA sequence and that the emission could identify a single mutation within the DNA strand [87,88]. Eventually, it was determined that the fluorescent properties are caused by the electronic transitions generated between the molecular orbitals of the nucleic acids and the silver nanoparticles, in which the transition can be excited by an incident resonant wavelength and lead to fluorescence generation.

At the same time as the fluorescence discovery of nucleic acids or DNA functionalized to silver, SERS studies on nucleic acid-silver composites suggested that the Raman signals of nucleic acid fluctuated based on experimental design and substrate fabrication, as independent results displayed significant variance. The experimental outcomes in SERS experiments have been discouraging as the four bases of DNA (adenine, cytosine, guanine, and thymine) gave far different Raman intensity

signals [89] and adenine was the only base that demonstrated single molecule SERS, [86] making Raman sequencing seemingly impossible. More importantly, signal domination from bases have changed from experiment [90] to experiment, [91] with different excitation wavelengths showing extreme variance of the measured Raman intensities and the Raman intensity never correlating to the concentration of the bases. [92]

Multiple explanations had been provided for these discrepancies, ranging from the magnitude difference of the Raman cross-sections of the bases [93] to the orientation of the molecules on the substrate leading to non-resonant enhancement. [92] The conclusion was drawn that determining a DNA sequence with SERS was unrealistic due to this inability in accurately measuring the SERS signature of nucleic acids. Although there are many challenges we face before realizing a Raman based DNA sequencing method, such as spatial resolution and poor signal-to-noise ratio, we must first resolve why there have been inconsistencies in SERS measurements of the DNA bases. As no confident conclusion has been developed to explain the inconsistent SERS amplification of nucleic acids or DNA bound to silver, this dissertation seeks to explain the discrepancies of the SERS signals of nucleic acid bound to silver nanoparticles.

2.6. Structure of Chapters

The SERS chemical effect can be classified into multiple categories. Of interest to this thesis, the static polarizability (Chapters 3-4) and charge-transfer effect (Chapters 5-6) are the focus of this work. The static polarizability offers unique

insight into the molecular orientation of the system. Depending on how nucleic acids bind to the silver structures, Raman modes are either enhanced or reduced based on the polarizability of the system. Thus, the static polarizability offers information on the geometrical properties of the system. The charge-transfer effect plays a different role in this study, as the charge-transfer effect causes a chemical resonance effect that enables chemical enhancement based on the excitation energy used and can thus be harnessed to selectively enhance specific nucleic acids. By tuning the excitation wavelength to match the electronic transitions of various systems, the systems can be discriminated against by switching the wavelengths. In this dissertation, we use the static polarizability effect to determine the preferential binding atoms of nucleic acids to silvers. Then, we show how we can take advantage of the charge-transfer between nucleic acids and silver to selectively enhance or reduce the SERS signatures based on excitation wavelength.

Chapter 3

Molecular Orientation Effect on Raman Signatures of Nucleic Acid-Silver Composites

3.1. Introduction

In this chapter, we begin our study on the static Raman polarizability effect as it pertains to nucleic acids functionalized to silver nanoparticles. The static Raman polarizability effect is critical to the understanding of molecular orientation and geometrical chemisorption binding properties as the polarization of the system is expressed in the Raman signatures measured. The Raman signal is dependent on the molecular structure of the system, in which bond lengths and angles can yield information on the stress and strain of the system and describe the molecular coordinates.

By attaching nucleic acids to silver nanoparticles or other plasmonic structures, the optical properties of such systems can be tuned in order to modify the function of these systems. Thus, certain characteristics can be either attenuated or amplified by understanding and controlling the way in which nucleic acids bind to the surface, as experienced when detecting the chirality of DNA strands grown on silver nanocrystals [94] and controlling the plasmonic properties of silver nanoparticles incubated with nucleic acids [95]. While there have been reports of finding the preferred binding sites of nucleic acids to silver, such as adenine binding to silver via the amino group [96], N1 [97], N3 [98], or N7 [99] atoms, the reports are often inconclusive, contradictory, and limited to qualitative analysis. There exists a need to quantitatively analyze the multiple potential binding sites of nucleic acids to silver, while also exploring the favorable optical properties that such systems provide

When nucleic acids bind to silver, the orientation of the molecule with respect

to the metal surface determines the polarizability of the system, leading to either enhanced or reduced Raman signal frequency modes depending on the molecular orientation with respect to the silver surface [29]. Therefore, by analyzing the calculated Raman signals of various atoms of nucleic acids bound to silver and comparing to experimental measurements, the preferred binding composition can be found and the nucleic acid silver system can be characterized quantitatively. In this chapter, we examine 18 simulated nucleic acid-silver composite structures (5 Adenine-Ag, 4 Cytosine-Ag, 5 Guanine-Ag, and 4 Thymine-Ag) and discuss the qualitative comparison between single binding site simulated Raman spectra to experimental Raman measurements [100].

3.2. Time-Dependent Density Functional Theory (TD-DFT) Simulations

To calculate the Raman frequency modes of molecular systems, we employ time-dependent density functional theory simulations (TD-DFT). TD-DFT simulations have become relevant in the field of SERS during the past 15 years, as advancement in computational power and memory have provided researchers the ability to simulate the vibrational frequencies of complex systems. Specifically, researchers have used TD-DFT methods to study the effects on Raman signatures of benzenethiol bound to silver clusters [101] and to measure the factor of static chemical enhancement of benzene bound to gold nanoparticles [29]. The TD-DFT method is based on density functional theory (DFT), in which the quantum system can be described by the density of the system. TD-DFT is an *ab initio* technique, derived purely from theoretical

principles and not requiring any experimental data input for calculations. The method has been commonly employed for estimating SERS chemical enhancement as it can be used to described excited state systems.

The 20 atom silver tetrahedral (Ag20) model has been the standard TD-DFT model for the past 10 years when representing silver nanoparticles. The model has three potential binding sites: the surface (S), the vertex (V), or the edge (E). The surface and edge represent the face-centered cubic (111) lattice and the vertex represents the adatom site. Due to the size of the silver films used in our experimental work, the adatom site is an unrealistic model for this system and thus will not be used. The nucleic acids can then bind to either the surface or the edge, with the surface being the common preferential binding site with the minimum energy geometry. To start, a preliminary TD-DFT study on adenine functionalized to the 20 atom silver tetrahedral structure is shown in section 3.3. The simulated Raman spectra for the 18 systems under study can be found in section 3.4, followed by experimental measurements in section 3.5. The available binding sites for each nucleic acid are determined by the presence of the most stable tautomers of adenine, cytosine, guanine, and thymine in water.

3.3. Static Polarizability Effect on Raman Signatures

In this section, we discuss the static polarizability effect on Raman signatures for nucleic acid-silver composites. We begin with a simple study to compare the TD-DFT simulations of two similar systems that yield significantly different results. For example, in the case of adenine, the molecular configuration bound via the N1 atom

results in significant changes in the Raman signature compared to the case of adenine bound via the N3 atom, as shown in Figure 3.1.

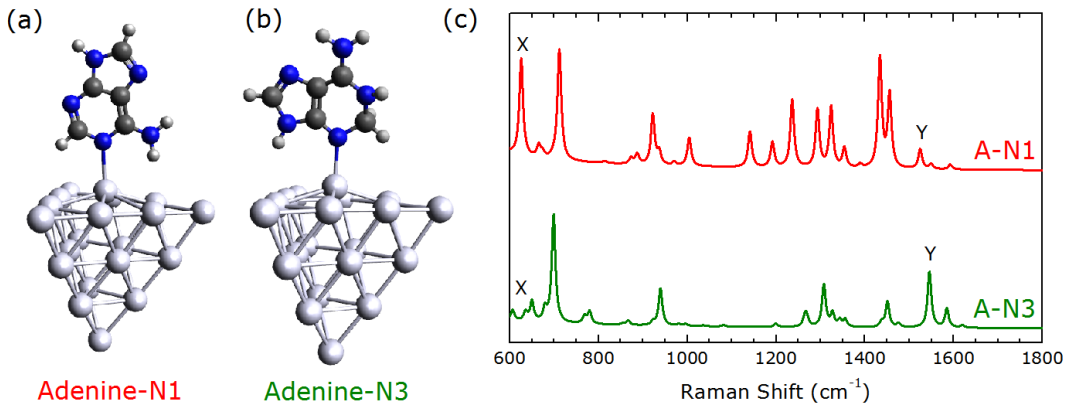

Figure 3.1. TD-DFT comparison of A-N1 and A-N3. Optimized geometrical structures for (a) adenine bound via N1 to silver (A-N1), (b) adenine bound via N3 to silver (A-N3). (c) The simulated Raman spectra of A-N1 and A-N3 with the ring deformation mode labeled as X and the ring stretching and amino deformation mode labeled as Y.

Here, we see that the ring deformation mode (~625 cm^{-1}) for N1 is significantly enhanced compared to the ring deformation mode of N3 based on the geometrical configuration. Alternatively, the ring stretching and amino deformation mode (~1550 cm^{-1}) for N1 is reduced compared to that mode for N3. By analyzing the Raman signatures of nucleic acids functionalized to silver nanoparticles, information regarding the binding configurations of atoms to silver can be extracted by studying the static polarizability effect. In this chapter, we study the simulated Raman spectra calculated from various configurations of nucleic acids to silver nanoparticles.

To determine the molecular orientation and polarizability, we use TD-DFT to geometrically optimize the structures and calculate the electronic transitions and vibrational frequencies. The geometry optimization repositions the atomic structure of

the system to reach an energy minimum, the electronic transition calculations apply an external potential and compute the change in charge density, and the vibrational frequency calculations vary the induced energy of the system and output the coordinates of the atomic vibrations for each frequency mode. As an example, depending on the adenine atom (N3, N7, or N9) that binds to the surface of the Ag20 tetrahedral surface (Figure 3.2a), the simulated Raman signal (Figure 3.2b), ultraviolet-visible absorption (Figure 3.2c) and circular dichroism (Figure 3.2d)

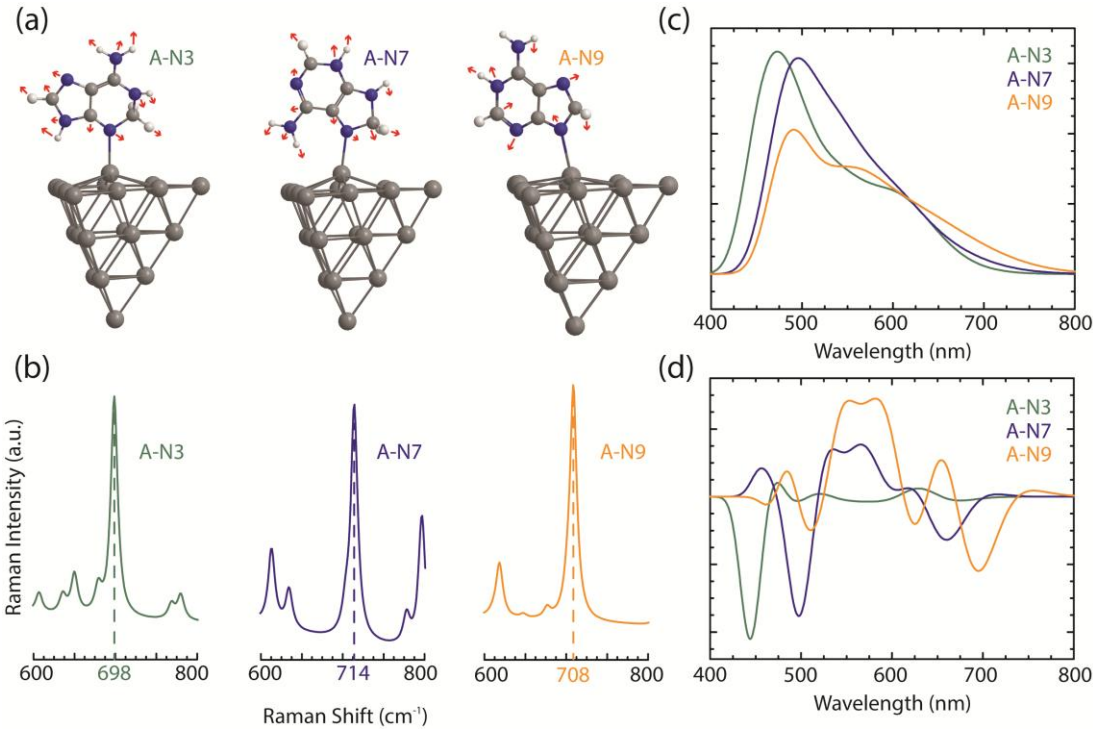

Figure 3.2. Variation of optical signals dependent on binding sites. (a) Optimized geometrical structures for 3 systems: A-N3 (green), A-N7 (blue), and A-N9 (orange) using TD-DFT calculations. The red arrows demonstrate the force displacement vectors for the ring-breathing-mode. (b) Simulated Raman spectra of the three systems for the ring-breathing-mode. The geometrical strain on the systems cause slight shifts in the location of Raman modes. (c) UV-VIS absorption (d) and circular dichroism simulated spectra for the 3 systems, demonstrating modulation of absorption dependent on binding site.

spectra demonstrate differing results due to the change in the polarizability, density of states and molecular orbitals of the systems, respectively. Although the UV-VIS absorption spectra are fairly similar, there are small changes in the intensity of the oscillator strength and bandwidth of each system. Circular dichroism spectroscopy simulations, used to study the chirality of molecules with polarized light, indicate significant changes in the optical properties caused by the change in geometrical structure and electron density of the systems. Thus, nucleic acids functionalized to silver composites induce distinct and notable transformations to the optical characteristics compared to isolated nucleic acids or silver nanoparticles.

As seen in this section, the different binding properties of nucleic acids to silver can have a significant impact on the Raman signatures of our systems. Thus, we want to utilize the simulated and measured Raman spectra to understand how the nucleic acids are binding to silver. Using TD-DFT simulations, we calculate the Raman frequencies for the 18 unique systems and then perform experimental Raman measurements of nucleic acids functionalized to random silver films. The results are qualitatively analyzed in section 3.6.

3.4. Simulated Raman Spectra of 18 Nucleic Acid-Silver Composite Systems

For the simulated Raman spectra, we use TD-DFT to first geometrically optimize our 18 systems under study. By considering every possible tautomer of each nucleic acid found in water [102–105], there are 18 potential nucleic acid-silver

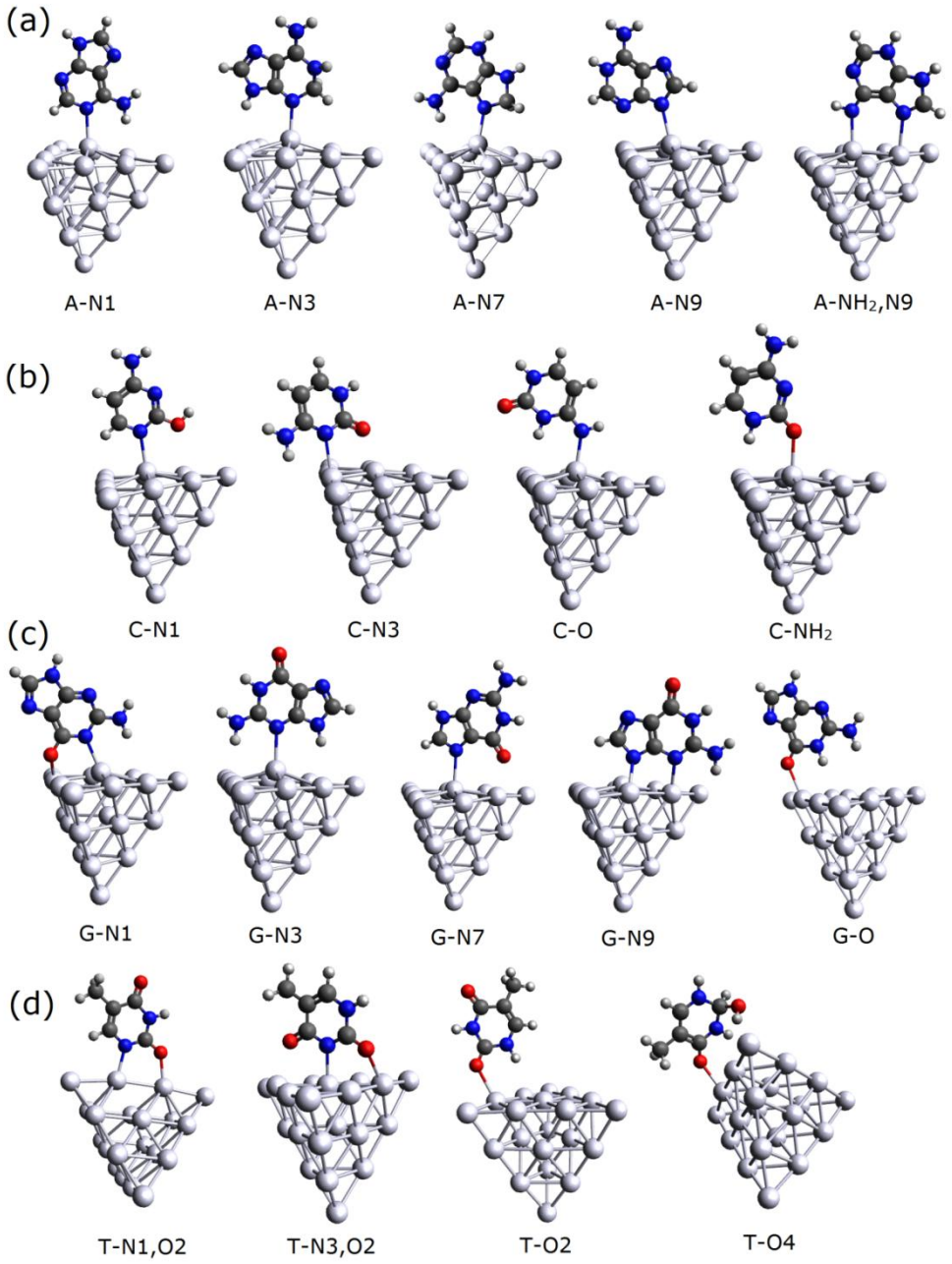

Figure 3.3. TD-DFT optimized geometries. Optimized geometrical structures of (a) adenine, (b) cytosine, (c) guanine, and (d) thymine bound to the Ag20 tetrahedral structure for each binding site.

configurations that undergo TD-DFT geometrical optimization and Raman frequency simulations (5 for A-Ag, 4 for C-Ag, 5 for G-Ag, and 4 for T-Ag). In accordance with

our previous simulations, the TD-DFT calculations are performed using Gaussian 09 [106] software on the Gordon supercomputer at the University of California, San Diego [107]. The 18 structures under study are geometrically optimized using the B3LYP method [108] and LANL2DZ [109] basis set. B3LYP is chosen as the density functional theory method as it uses both generalized gradient approximations and the local-density approximation and has been shown to be an accurate model for molecules attached to the Ag20 structure. LANL2DZ is used to account for the silver atoms. A very tight convergence criterion is used and a super fine grid of 150,974 and 225,974 is required for the nucleic acid atoms and silver atoms, respectively. Once optimized, each structure is confirmed to have no negative frequency, showing successful convergence. The optimized geometrical figures are shown in Figure 3.3.

The electronic transitions and Raman frequencies are calculated via Gaussian 09, using the same basis set and method as the geometric optimization. The electronic transition calculations apply an external potential and compute the change in charge density and the vibrational frequency calculations vary the induced energy of the system and output the coordinates of the atomic vibrations for each frequency mode. TD-DFT calculates Raman optical activities for each mode, which are converted to Raman intensities using the following relationship [110]:

$$\frac{\partial \sigma_j}{\partial \Omega} = \left(\frac{2^4\pi^4}{45}\right)\left(\frac{\left(\nu_0 - \nu_j\right)^4}{1 - e^{\left[\frac{-hc\nu_j}{kT}\right]}}\right)\left(\frac{h}{8\pi^2 c\nu_j}\right)S_j$$

$$S_j = 45\left(\frac{d\alpha}{dQ_j}\right)^2 + 7\left(\frac{d\gamma}{dQ_j}\right)^2$$

Where σ is the Raman cross-section, Ω is the depolarization ratio, ν_0 is the frequency of the incident light, ν_j is the frequency of the vibrational mode, S_j is the Raman scattering factor, α is the polarizability, γ is the anisotropic polarizability, and Q_j is the normal coordinate. An incident wavelength of 785nm and a temperature of 293K are used to match experimental conditions. The simulated Raman spectra is plotted by applying a Lorentzian fit for each Raman intensity mode, using a total of 3000 points between 400 cm^{-1} and 4000 cm^{-1} with a full-width half maximum of 10 cm^{-1}. Because TD-DFT overestimates the location of the frequency mode due to the neglect of electron correlation and anharmonicity [111], a scaling factor of 0.9891 for 600 cm^{-1} to 1000 cm^{-1} and of 0.9568 for 1000 cm^{-1} to 1800 cm^{-1} is used, as determined for the B3LYP method and LANL2DZ basis set [112]. Simulated Raman spectra are obtained for each of the 18 systems and can be found in Figure 3.7, in which they are directly compared to experimental measurements.

3.5. Experimental Silver Nanoparticles and Raman Measurements

The SERS substrates used for experimental measurements, represented best by the Ag20 model, are random silver films (RSFs) in which an electron beam evaporation system is used to deposit 30 nm of silver onto a silicon substrate. At this thickness, the silver nanoparticles merge together to become irregular shaped islands (Figure 3.4). The resulting SERS substrates generate a fairly consistent electromagnetic field enhancement across a broad excitation wavelength range. The

silver films have a face centered cubic (111) surface which is represented by the silver 20 atom tetrahedral structure surface (S) side.

The random silver films adopt the face-centered cubic (111) surface [113] and demonstrate a consistent electromagnetic field enhancement effect at an excitation wavelength of 785 nm. The extinction spectra of random silver films with thicknesses of 30 nm have shown to have weak to non-existent surface plasmon resonance at excitation wavelengths of 785 nm [114], so the electromagnetic enhancement does not factor into the experimental Raman spectra. As studied previously, the surface of a 20 atom silver tetrahedral surface is the model system to use in TD-DFT simulations when representing the fcc (111) surface [115], and thus random silver films are the ideal substrate to use for our experimental measurements.

Random silver films have a broad extinction profile in the visible range which has a weak surface plasmon resonance in the near-infrared range. Thus, the electromagnetic effect has a minimal effect on the measured Raman spectra. The extinction profile for silver films is shown in Figure 3.5, in which two excitation wavelengths (514 nm and 785 nm) are displayed with their corresponding Raman frequency modes. While an excitation wavelength of 514 nm shows a slight increase in the 1335 cm^{-1} mode compared to the 720 cm^{-1} mode, the frequency modes excited by the 785 nm wavelength show consistent enhancement based on the extinction profile. So, Raman modes measured with an excitation wavelength of 785 nm have consistent Raman mode enhancement across the spectral range.

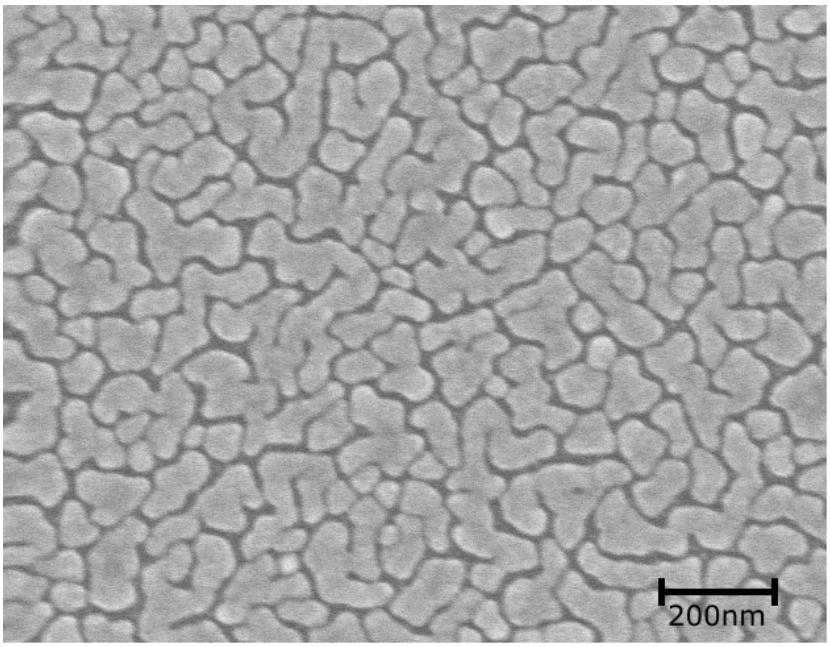

Figure 3.4. SEM of random silver films. Scanning electron microscope image of random silver films.

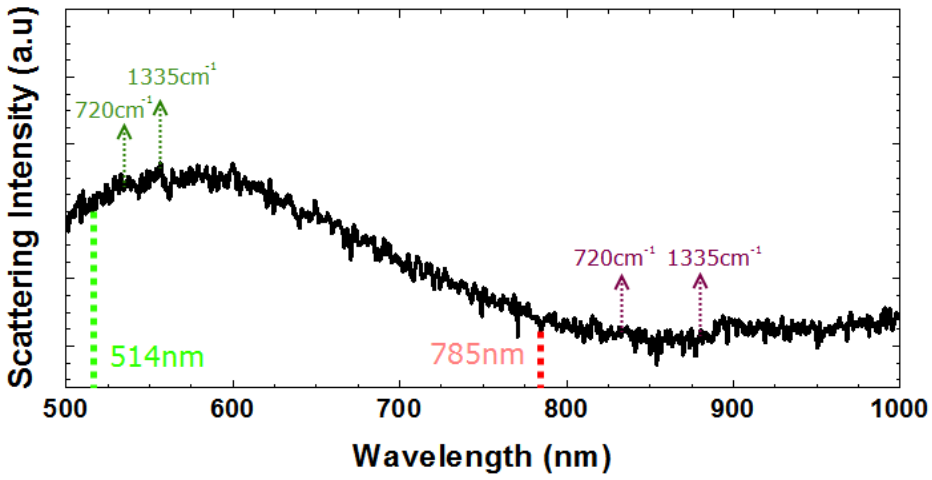

Figure 3.5. Extinction spectrum of silver films. Extinction spectrum of silver films showing two excitation wavelengths and the corresponding Raman shifts.

To further demonstrate the consistency of the electromagnetic field enhancement across the substrate, Raman maps are acquired of 1 mM of adenine

dissolved on random silver films at excitation wavelengths of 514 nm and 785 nm. An area of approximately 50 microns by 50 microns was analyzed via a raster scan with spot sizes of approximately 10 by 10 microns. For analysis, the peak intensity ratio of the single stretching mode (~1335 cm^{-1}) to the ring breathing mode (~720 cm^{-1}) was calculated at each spot and a colored Raman map based on the intensity ratio was plotted. Figure 3.6 shows the resulting Raman maps for 514 nm (blue) and 785 nm (red). The Raman maps show consistent peak intensity ratio at each spot along the map for both wavelengths, with an average 1335 cm^{-1} to 720 cm^{-1} ratio of 0.29 (σ = 0.020) for 514 nm and 0.23 (σ = 0.019) for 785 nm. Thus, the electromagnetic field enhancement effect is fairly consistent across the substrate.

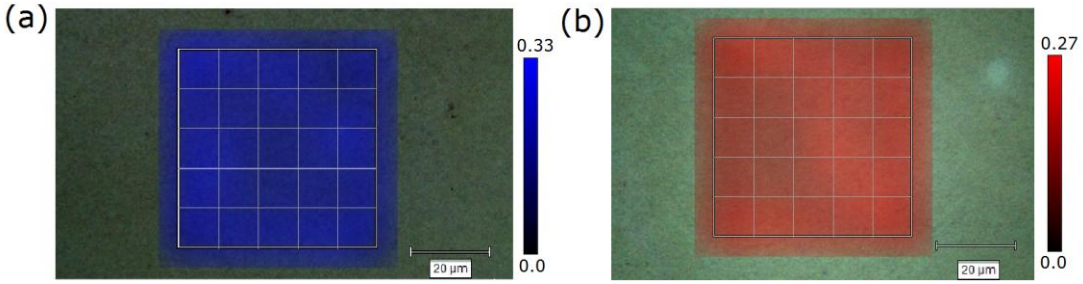

Figure 3.6. Raman map of silver films. Raman map of 50 microns by 50 microns area of adenine functionalized on random silver films for excitation wavelengths of (a) 514 nm and (b) 785 nm.

To emulate the simulated Raman calculations we performed in section 3.4 and ensure the accuracy of our experimental results, nucleic acids are dissolved in water and functionalized to silver films to permit the formation of multiple tautomers that could bind to the silver surface. For the experimental nucleic acid Raman data, silver

films are fabricated by depositing 300 Å of silver using an e-beam evaporator (Temescal BJD, UCSD Nano3 Cleanroom) on a silicon wafer. Nucleic acids are deposited at a concentration of 1 mM and are incubated on the silver films overnight. Before measuring the Raman spectra, the samples are rinsed with H_2O to remove any large particles. The Raman measurements are acquired using a Renishaw Raman spectrometer at a wavelength of 785nm. The sample is imaged using a 40x objective and the spectra are recorded with the hyperSpec program. A 60s acquisition time is used with a Raman spectral range of 550 cm^{-1} to 2000cm^{-1}. Baseline subtraction is performed to ensure all spectra are aligned with the x-axis. The experimental Raman measurements are then compared to the simulated Raman calculations in section 3.6 in Figure 3.7.

3.6. Simulated and Experimental Raman Measurements Comparison

The Raman spectra for the simulated Raman frequencies of the 18 nucleic-acid silver composites and the experimental Raman measurements can be found in Figure 3.7, followed by a brief qualitative comparison between the experimental measurements and corresponding simulated Raman spectra. The complete results of the Raman frequency modes for all nucleic acid-silver composites can be found in the appendix (Tables A.1 to A.4).

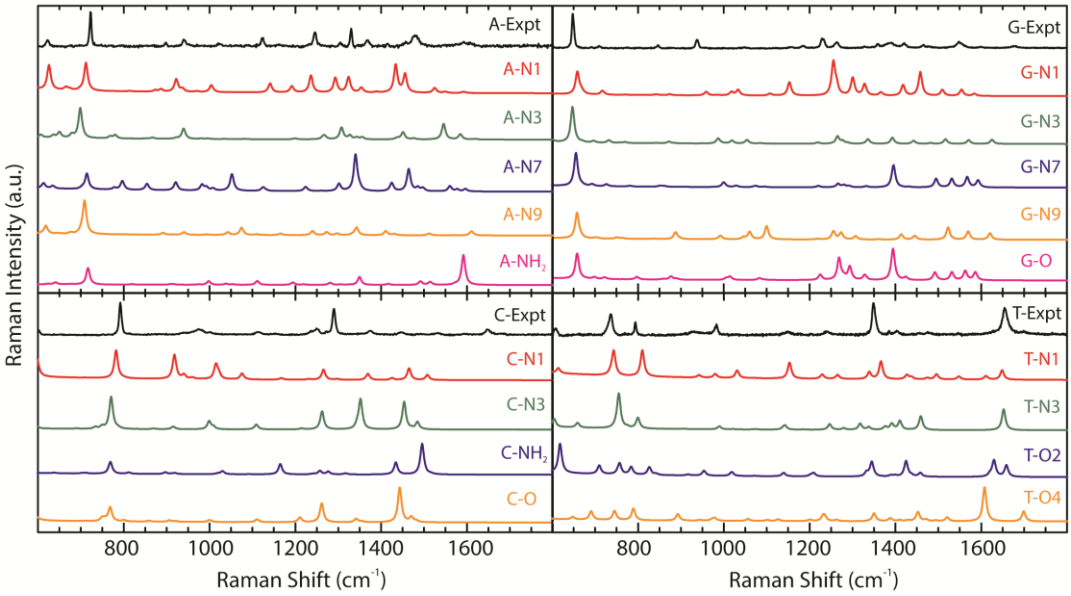

Figure 3.7. Raman spectra of 18 NA-Ag systems and experimental results. Experimental Raman spectrum measurements (black) of the 4 nucleic acids (A - adenine, C - cytosine, G - guanine, T - thymine) attached to silver and simulated Raman spectra of binding atoms (red, green, blue, orange, magenta) of the 18 systems under study.

The prominent features of adenine's surface-enhanced Raman spectrum include the ring-breathing mode (720 cm^{-1}), stretching modes of carbon atoms to the NH_2 group and N3 and N9 atoms (1125 cm^{-1}), stretching modes of carbon to N1 and N7 atoms (1310 cm^{-1}), and the scissor mode of NH_2 (1485 cm^{-1}). The most similar calculated Raman spectra to the experimental measurement is A-N3. In this spectrum, the ring-breathing mode, carbon stretching modes to N atoms, and the scissor NH_2 modes are enhanced. Modes including the deformation mode of the ring structures (625-697 cm^{-1}), C-H wag mode (938 cm^{-1}) and NH_2 rock mode (980-1081 cm^{-1}) are fairly weak in comparison, agreeing well with experimental results. The other potential binding sites (A-N1, A-N7, A-N9 and A-NH_2,N7) show differences with

respect to the experimental spectrum. The A-N1 spectrum has a strongly enhanced ring deformation mode (625 cm^{-1}). The A-N7 spectrum shows a weaker ring-breathing-mode (713 cm^{-1}) and a stronger C-NH_2 wag mode (991 cm^{-1}). The A-N9 spectrum shows several similarities to the experimental measurements, including a strong ring-breathing-mode (708 cm^{-1}) and weak C-H wag (940 cm^{-1}) and NH_2 (993 cm^{-1}) rock modes, but it also shows weak stretching modes of C-N atoms (1041 cm^{-1}). The A-NH_2,N7 spectrum also shows dramatic differences with the NH_2 scissor mode (1591 cm^{-1}) greatly enhanced in the simulation.

The most intense modes of the experimental Raman spectrum of cytosine on silver films are the ring-breathing-mode (790 cm^{-1}) and the C-N3 and C-NH_2 stretching modes (1290 cm^{-1}). In addition, there are some moderately expressed modes including the ring deformation mode (975 cm^{-1}), the NH_2 rock and N1-C-H bend modes (1248 cm^{-1}) and the NH_2 scissor mode (1648 cm^{-1}). Weakly expressed modes include the C-H bend mode (1000 cm^{-1}) and the C=C stretching mode (1448 cm^{-1}). The most similar simulated spectrum is when the N3 atom binds to the surface of Ag20 (C-N3). This spectrum is dominated by the ring-breathing-mode (688-748 cm^{-1}) and has a high contribution from the C-N stretching modes (1343-1351 cm^{-1}). The spectrum has moderate Raman intensities for the ring deformation mode (998 cm^{-1}), the C-N1 stretching mode (1100-1108 cm^{-1}), and the NH_2 scissor mode (1484 cm^{-1}). The other three cytosine spectra show significant variance with respect to the experimental spectrum. The C-N1 spectrum has an enhanced ring deformation mode (1014-1021cm^{-1}) and a weak C-N stretching mode (1297cm^{-1}). The C-NH_2 spectrum

shows an enhanced NH_2 scissor mode (1516cm^{-1}) and the C-O spectrum shows an overly enhanced C-N stretching mode (1442cm^{-1}).

Of the 5 potential binding sites for guanine, multiple binding sites have been proposed, with the double bond N ring atoms being suggested as the primary potential binding sites. The spectrum of guanine attached to silver films, like adenine and cytosine's, is dominated by the ring-breathing-mode (646 cm^{-1}). This is the strongest Raman mode by a significant amount. There are some moderately enhanced modes, including the 5-atom ring deformation mode (937 cm^{-1}), the C-N7 and C-N9 stretching mode (1229 cm^{-1}), and the C=C, C-N2, and C-N3 stretching modes (1548 cm^{-1}). The G-N3 spectrum has the most similar features to the experimental result. The ring-breathing-mode is the most dominant mode (646-669 cm^{-1}) and stands as the only strong Raman mode. There are some moderately enhanced modes, including the 5 atom ring deformation mode (986-996 cm^{-1}) and the C-N stretching modes (1265-1288 cm^{-1}). The other spectra show many differences. The G-N1 spectrum shows a moderate ring-breathing-mode (658 cm^{-1}) and an enhanced C-N stretching mode (1255 cm^{-1}). The G-N7 spectrum is fairly similar to experimental spectrum with a strong ring-breathing-mode (654-667 cm^{-1}), but has an overly enhanced C-N7 and C-N9 stretching mode (1395 cm^{-1}). The G-N9 spectrum is the most similar to the experimental measurement, second only to G-N3, but the deformation modes (1099 cm^{-1} and 1273 cm^{-1}) are overly enhanced. The G-O spectrum is very inconsistent, with the C-N stretching mode (1394 cm^{-1}) dominating over the ring-breathing-mode (657-696 cm^{-1}).

The experimental spectrum of thymine functionalized to silver films shows a strong ring-breathing-mode (735 cm^{-1}), C-CH_3 stretching mode (1348 cm^{-1}), and C=O stretching mode (1656 cm^{-1}). There is also a moderate contribution from the ring deformation mode (795 cm^{-1}) and C=C stretching mode (983 cm^{-1}). There is significant variance in the simulated spectra of the four potential binding atoms. The T-N1,O2 spectrum has a strongly enhanced ring-breathing-mode (742 cm^{-1}), but that mode is weaker than the ring deformation mode (808 cm^{-1}). The C=O stretching mode is also weaker (1564-1601 cm^{-1}). The T-N3,O2 spectrum has a weak deformation mode (799 cm^{-1}) and an overly enhanced CH3 wag mode (1458 cm^{-1}). The T-O2 spectrum results in an overly enhanced deformation of C-CH3 mode (617 cm^{-1}). The T-O4 spectrum has a very strong dominant C=O stretching mode (1607-1698 cm^{-1}), but has a weak ring-breathing-mode (744 cm^{-1}).

3.7. Conclusion

The simulated Raman spectra calculated in this chapter show clear deviations from the experimental measurements that were recorded. Thus, it is necessary to quantitatively evaluate the data. In the next chapter, we detail the simulated Raman correlation spectroscopy (SRCS) process in which we apply an algorithm to estimate the percent composition of preferential binding sites of nucleic acids to silver composites.

This chapter is, in part, a reprint that the dissertation author was the principal researcher and author of. The material appears in *Scientific Reports.* (L.M. Freeman,

A. Smolyaninov, L. Pang, Y. Fainman, "Simulated Raman correlation spectroscopy for quantifying nucleic acid-silver composites" *Scientific Reports*, 6, 23535, 2016.)

Chapter 4

Simulated Raman Correlation Spectroscopy (SRCS) Analysis

4.1. Introduction

While there have been many publications regarding comparison between experimental Raman measurements and TD-DFT vibrational frequency analysis, the published results have neglected to include quantitative analysis and have instead been supported by qualitative statements [65,101,103,115,116]. Additionally, we see from chapter 3 that qualitative analysis is insufficient for making conclusions about the preferred binding sites. Here, we demonstrate the development of a quantitative comparison method for directly contrasting the simulated Raman spectra with the experimental Raman measurements of nucleic acids functionalized to silver nanoparticles.

We begin with determining the correlation between the experimental measurement and the simulated Raman spectrum of a single binding site. Due to the poor correlation between the experimental data and the Raman frequencies of a single binding site, we implement the simulated Raman correlation spectroscopy (SRCS) analysis in which we statistically compare the simulated Raman spectra of several binding configurations with experimental measurements of nucleic acids on silver and then implement the SRCS method. The SRCS method optimizes the coefficient of determination between the simulated and experimental measurements by calculating the ideal weighted composition of binding configurations that results in the highest correlation. We perform the SRCS process for the four nucleic acids, demonstrating that nucleic acids preferentially bind to silver as a combination of weighted configurations, rather than by single binding sites.

4.2. Raman Mode Assignment

Before performing the quantitative correlation calculations, the calculated vibrational frequency modes are aligned with experimental measurements and are normalized with respect to the total Raman intensities of the system. The intensity of the Raman frequency modes are used rather than the location of the Raman frequency modes due to the incomplete basis set and neglect of anharmonicity [117]. The prominent Raman frequency modes are assigned discrete values by visualizing each mode in GaussView. The computed vibrational frequencies are slightly off-set from each other because the frequency modes for each system vary slightly in location dependent on the orientation of the molecule with respect to the surface, as the molecular strain changes the way in which the system vibrates and leads to small shifts in the vibrational frequencies. As an example, the adenine silver systems (A-N1, A-N3, A-N7, A-N9, A-NH_2,N7) have different calculated frequencies for the ring-breathing-mode (RBM) that are determined by the molecular vibrations. GaussView is used to visualize the modes, display the force displacements and appropriately assign each frequency value with the corresponding mode. The frequencies for A-N1, A-N3, A-N7, A-N9, and A-NH_2,N7 have RBM mode locations of 711 cm^{-1}, 698 cm^{-1}, 714 cm^{-1}, 708 cm^{-1} and 716 cm^{-1}, respectively (Figure 4.1).

The minor variation between the vibrational frequencies for the RBM is caused by the molecular strain of the system which modulates the bond force constants of the structure. Thus, despite the difference in frequency values, the frequencies from 698-716 cm^{-1} are assigned to the RBM by visualizing the force displacements of the

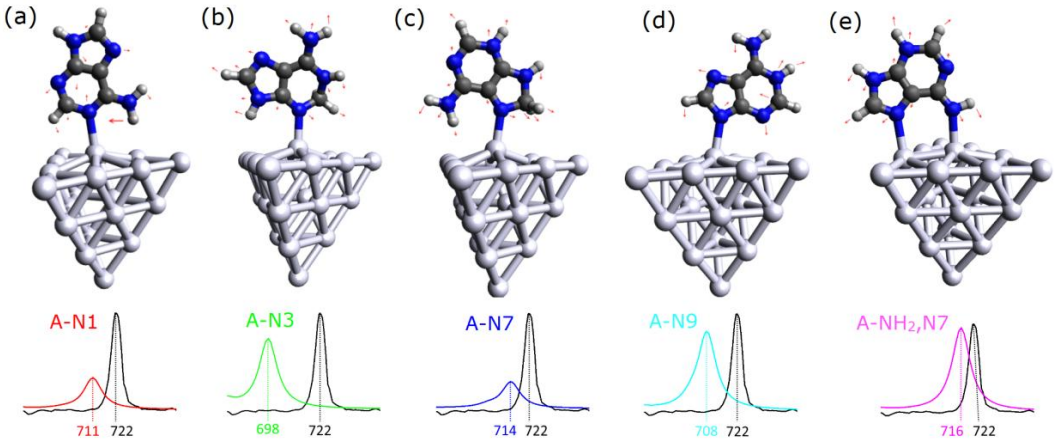

Figure 4.1. Raman RBM of A-Ag. The simulated Raman ring breathing mode locations for A-N1 (red, 711 cm^{-1}), A-N3 (green, 698 cm^{-1}), A-N7 (blue, 714 cm^{-1}), A-N9 (cyan, 708 cm^{-1}), and A-NH_2,N7 (magenta, 716 cm^{-1}) in comparison to the experimental ring breathing mode location (black, 722 cm^{-1})

modes. The experimental measurements have the RBM slightly red-shifted compared to the simulated measurements due to the scaling factor used in the calculations, with the experimental RBM band ranging from 715 cm^{-1} to 743 cm^{-1}. The strongest 10 to 12 frequency modes for each nucleic acid, such as the RBM, are selected for analysis using GaussView to visualize the force displacement vectors. The list of modes can be found in appendix A (Tables A.1 to A.4).

4.3. Raman Mode Comparison for Single Binding Sites

To begin the quantitative comparison, we start with the simple case of statistically comparing the normalized modal intensities of a single binding site to experimental measurement in which the coefficient of determination for each single atom binding site (e.g. A-N1 compared to experimental measurement) is calculated. We assign the Raman frequencies into discrete modes for both the experimental

spectrum and corresponding simulated binding site spectra, where the experimental Raman spectrum mode for a nucleic acid NA and a mode of *i* is defined as E_i^{NA} and the simulated Raman spectrum mode for a nucleic acid NA, a binding site of b, and a mode of *i*, is defined as $S_{i,b}^{NA}(v)$. We consider the case of a nucleic acid that has an experimental Raman spectrum, $\underline{e}^{NA}$, and multiple corresponding simulated Raman spectra, $\underline{s_b}^{NA}$, in which the potential binding sites are described as b=1,2,...,B and the discrete frequency modes as m=1,2,...,M. The discrete frequency modes are extracted from the continuous Raman spectra $\hat{e}^{NA}$ and $\hat{s}_b^{NA}$, in which the GaussView program is used to visualize and assign the frequency modes to discrete values (section 4.2). We denote the modal intensities of the experimental measured spectra $\underline{e}^{NA} = [e_1^{NA}, \dots e_i^{NA}, \dots e_M^{NA}]$ and the modal intensities of the simulated spectra $\underline{s_b}^{NA} = [s_{1,b}^{NA}, \dots s_{i,b}^{NA}, \dots s_{M,b}^{NA}]$, in which b designates the binding site (e.g., N1, N3).

We then normalize the Raman intensity of each frequency mode with respect to the sum of the Raman modal intensities of the selected Raman mode for each spectrum. The experimental Raman intensity of the frequency mode *i* is normalized to E_i^{NA} with the following equation:

$$E_i^{NA} = \frac{e_i^{NA}}{\sum_{m=1}^{M} e_m^{NA}} \qquad (4.1)$$

in which e_i^{NA} is the experimental Raman intensity at a specific frequency mode *i*, $\sum_{m=1}^{M} e_m^{NA}$ is the sum of the experimental Raman intensities of frequency modes from 1 through M, and E_i^{NA} is the normalized experimental Raman intensity for mode *i*. The

normalized modal intensities for the experimental Raman measurement can be designated as:

$$\underline{E}^{NA} = [E_1^{NA}, \dots E_i^{NA}, \dots, E_M^{NA}] \qquad (4.2)$$

For the case of the simulated Raman intensities, assuming the simulated spectrum is for a nucleic acid bound to silver via the binding site *b*, the normalized Raman intensity for mode *i* is represented by the following equation:

$$S_{i,b}^{NA} = \frac{s_{i,b}^{NA}}{\sum_{m=1}^{M} s_{m,b}^{NA}} \qquad (4.3)$$

in which $s_{i,b}^{NA}$ is the simulated Raman intensity of a nucleic acid bound via binding site *b* at a specific frequency mode *i*, $\sum_{m=1}^{M} s_{m,b}^{NA}$ is the sum of the simulated Raman intensities of a nucleic acid bound via binding site *b* from modes 1 to *M*, and $S_{i,b}^{NA}$ is the normalized simulated Raman intensity mode of a nucleic acid bound via binding site *b* for mode *i*. Thus, the normalized modal intensities for a simulated Raman measurement can be designated as:

$$\underline{S}_b^{NA} = [S_{1,b}^{NA}, \dots, S_{i,b}^{NA}, \dots, S_{M,b}^{NA}] \qquad (4.4)$$

The discrete mode assignment and normalization of the frequency modes are shown in Figure 4.2, in which the continuous Raman spectrum $\hat{s}_b^{NA}$ is assigned discrete modes $\underline{s}_b^{NA} = [s_{1,b}^{NA}, \dots s_{i,b}^{NA}, \dots s_{M,b}^{NA}]$ and then normalized to generate $\underline{S}_b^{NA}$.

To determine the correlation between $\underline{E}^{NA}$ and $\underline{S}_b^{NA}$, we calculate the coefficient of determination (r^2) according to the following equation:

$$r^2 = \left(\frac{\sum_{m=1}^{M} E_m^{NA} S_{m,b}^{NA} - \sum_{m=1}^{M} E_m^{NA} \sum_{m=1}^{M} S_{m,b}^{NA}}{\sqrt{\left\{\sum_{m=1}^{M} (E_m^{NA})^2 - (\sum_{m=1}^{M} E_m^{NA})^2\right\}\left\{\sum_{m=1}^{M} (S_{m,b}^{NA})^2 - (\sum_{m=1}^{M} S_{m,b}^{NA})^2\right\}}} \right)^2 \qquad (4.5)$$

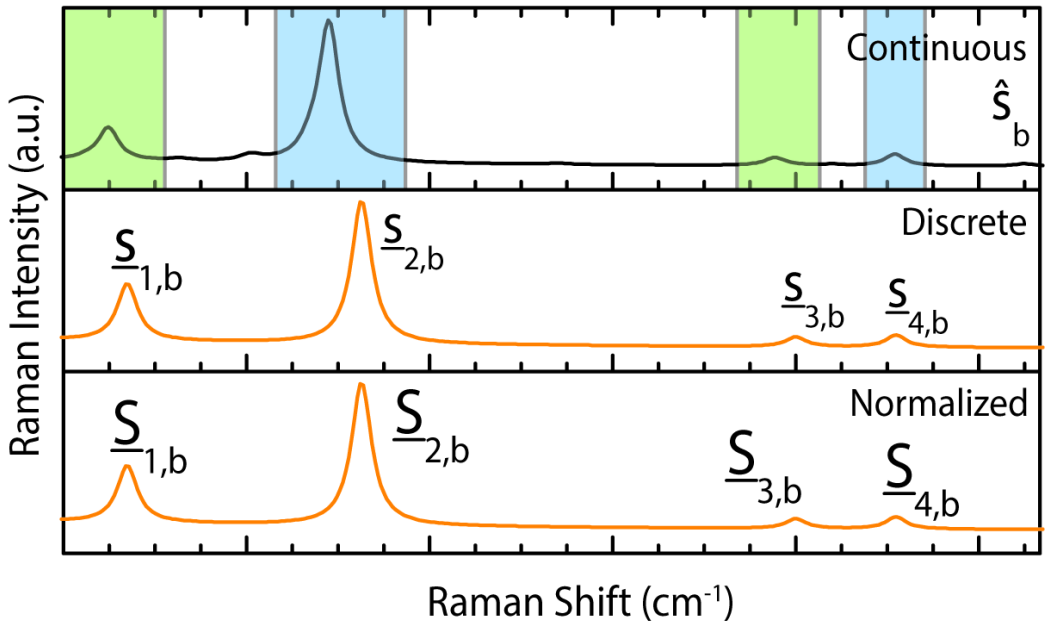

Figure 4.2. Discrete mode analysis. The normalization procedure for each spectrum, in which the continuous spectrum $\hat{s}_b^{NA}$ (top) is assigned discrete modal values m=[1,2,…,M] and aligned with the corresponding experimental discrete modes $\underline{e}^{NA}$, described as a vector $\underline{s}_b^{NA}$ (middle). The Raman intensity of each mode is then normalized using equation 4.3 to generate $\underline{S}_b^{NA}$ (bottom).

Here, the coefficient of determination represents the correlation of the simulated Raman spectrum of a single binding site to the experimental Raman spectrum, with a value $r^2 = 1$ constituting perfect correlation. The residuals for each mode are shown in Figure 4.3, determined by the equation $\varepsilon = \left|E_m^{NA} - S_{m,b}^{NA}\right|$ for each mode *m*. The bar plots represent the absolute deviation of the simulated mode with respect to the experimental mode and the dotted line shows the mean of the absolute deviation. The scatter plots display the relative deviation for each mode compared to the experimental result (y=0) with the coefficient of determination (r^2) displayed on the plot. The coefficient of determination ranges from very poor (A-NH_2,N7, 0.022) to fairly strong

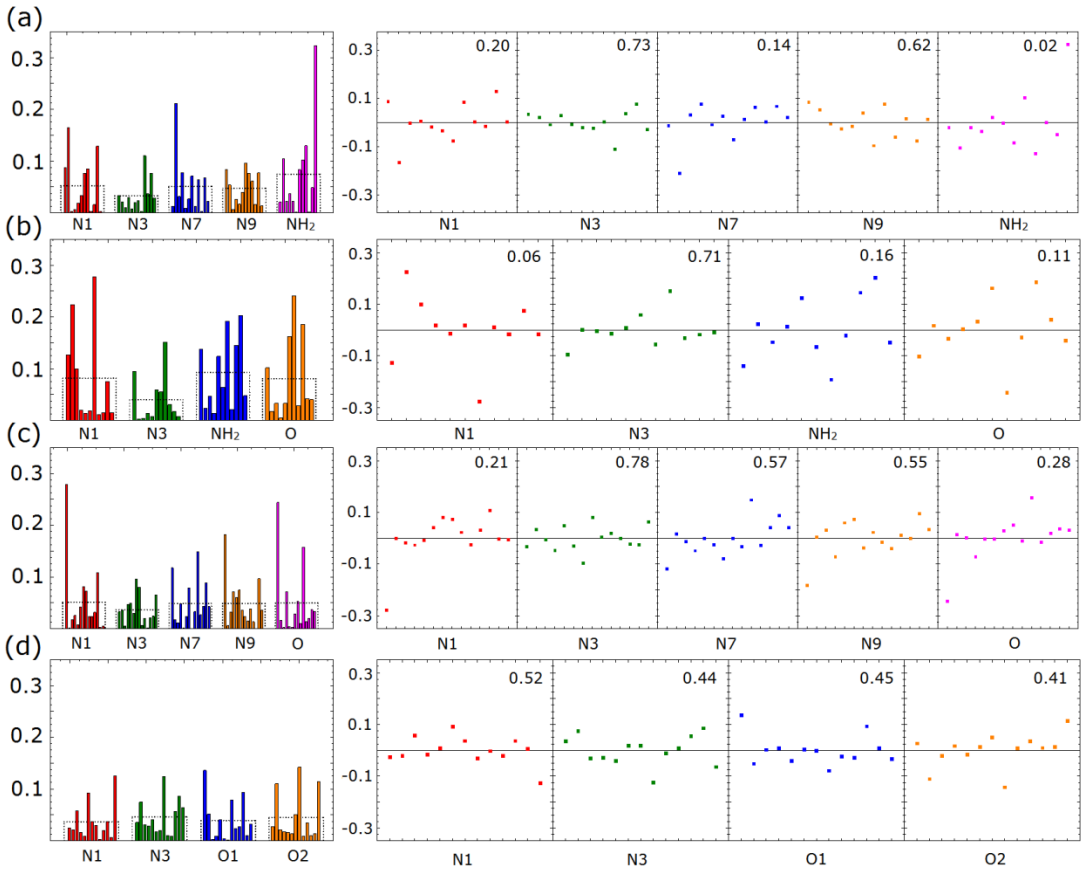

Figure 4.3. Deviation of Raman modes. The absolute deviation of the simulated normalized Raman mode intensities for (a) adenine, (b) cytosine, (c) guanine, and (d) thymine. Each individual bar represents a mode, starting from the shortest (~600 cm^{-1}) to the longest (~1700 cm^{-1}) frequency mode. The dotted line represents the average deviation for all modes in that system. Residual plots are shown for each individual system with the coefficient of determination stated in the inset.

(G-N3, 0.78), with the N3 binding atom showing decent correlation for adenine, cytosine, and guanine. Thymine is very ambiguous, with each atom showing a poor coefficient of determination.

Despite the above average correlation for A-N3, C-N3, and G-N3, there are still some simulated modes in these systems that show significant deviation from the experimental values. For example, the C-N stretching mode for A-N3 is greatly

enhanced in experimental measurements, but significantly reduced in the simulation results. The C-NH_2 stretching mode for C-N3 is strong in simulations, but very weak in the experimental spectra. Additionally, the C-NH_2 bending mode is absent in the C-N3 simulations. These discrepancies reveal that there is more than one binding site responsible for the Raman signatures in experimental measurements and that the experimental measurements are superimposed spectra of the possible binding sites. To improve the coefficients of determination, the SRCS process is performed in which the coefficient of determination is maximized by finding the optimal weighted coefficient constants for each nucleic acid. When comparing the simulated spectra to the experimental spectrum for each nucleic acid (NA), we conclude that single binding site simulations have deviations with respect to the experimental measurement, as determined by linear regression analysis, and thus the experimental measurement cannot be deduced to a single binding site.

4.4. Simulated Raman Correlation Spectroscopy (SRCS) Process

When comparing the simulated spectra to the experimental spectrum for each nucleic acid (NA), we conclude that single binding site simulations have deviations with respect to the experimental measurement, as determined by linear regression analysis, and thus the experimental measurement cannot be deduced to a single binding site. Thus, SRCS is employed to determine the weighted composition of binding sites by optimizing the calculated correlation. The SRCS process for each

nucleic acid consists of 1) assigning the continuous Raman frequency spectral modes to discrete values for the experimental spectrum and all simulated binding site spectra; 2) normalizing the Raman intensity of each frequency mode with respect to the sum of the Raman modal intensities of the selected Raman modes for each spectrum, and 3) calculating the weighted coefficients for each binding site that yield the optimal coefficient of determination in terms of all binding sites, r^2, when comparing the cumulative weighted simulated Raman spectra to the experimentally detected Raman spectrum.

Upon completion of steps 1 and 2, as described in sections 4.3 (equations 4.1-4.4), and given the experimental discrete Raman mode intensities $\underline{E}^{NA}$, we assume that there is a set of corresponding weighted constants that maximize the correlation of $\underline{E}^{NA}$ with respect to a linear superposition of a set of weighted spectra $\underline{S}_b^{NA}$, where b=1,2,...B. We define the weighted superimposed simulated spectra $\underline{S}_{tot}^{NA}$ as:

$$\underline{S}_{tot}^{NA} = \sum_{b=1}^{B} k_b^{NA} \underline{S}_b^{NA} \qquad (4.6)$$

where each value of k_b^{NA} represents the weighted constants for the corresponding simulated spectrum based on binding site b. The weighted constants are normalized as:

$$\sum_{b=1}^{B} k_b^{NA} = 1 \qquad (4.7)$$

Then, we vary the values of k_b^{NA} in equation 4.6 in order to optimize the correlation between the weighted spectral modes $\underline{S}_{m,tot}^{NA}$ of the simulated data $\underline{S}_{tot}^{NA}$ and the measured spectral modes E_m^{NA} of the experimental data $\underline{E}^{NA}$ by using the following equation for the coefficient of determination:

$$r^2 = \left(\frac{\sum_{m=1}^{M} E_m^{NA} S_{m,tot}^{NA} - \sum_{m=1}^{M} E_m^{NA} \sum_{m=1}^{M} S_{m,tot}^{NA}}{\sqrt{\left\{\sum_{m=1}^{M} (E_m^{NA})^2 - (\sum_{m=1}^{M} E_m^{NA})^2\right\}\left\{\sum_{m=1}^{M} (S_{m,tot}^{NA})^2 - (\sum_{m=1}^{M} S_{m,tot}^{NA})^2\right\}}} \right)^2 \qquad (4.8)$$

The value of r^2 is optimized by varying the weighted constants of k_b^{NA} in equation 4.6 and calculating the value of $\underline{S}_{tot}^{NA}$ (Figure 4.4). The coefficient of determination given by r^2 measures the linear correlation between an experimental spectrum $\underline{E}^{NA}$ and weighted calculated spectrum $\underline{S}_{tot}^{NA}$, with $r^2 = 1$ corresponding to perfect correlation. By applying signal processing techniques [118], the weighted constants k_b^{NA} which produce an $\underline{S}_{tot}^{NA}$ that maximizes r^2 are calculated and represent the best possible compositional analysis of experimental binding sites within the limits and numerical accuracy of the simulated binding sites and determine how well the chosen weighted spectra works as a least squares estimator for the experimental spectrum.

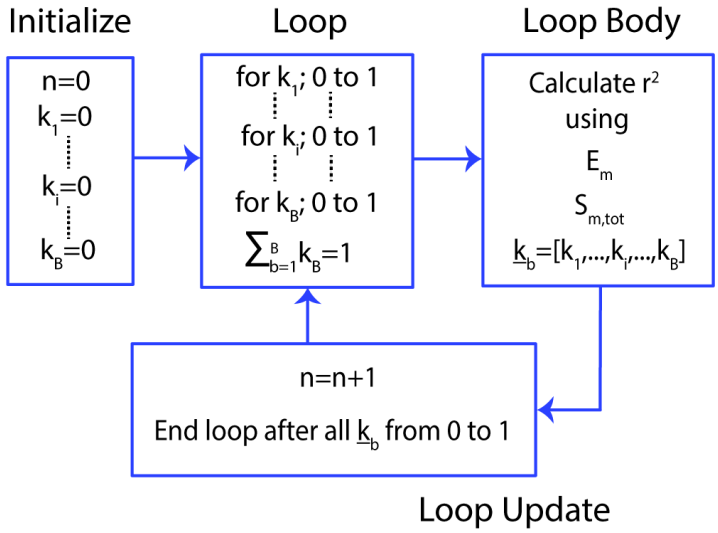

Figure 4.4. Schematic diagram of SRCS. Flow diagram describing the SRCS process, in which the values of k_b^{NA} are varied while calculating r^2 using E_m^{NA} and $S_{m,tot}^{NA}$ given by equation 4.2 and equation 4.6, respectively.

The SRCS process is applied to all four nucleic acids, in which approximately 175,000 iterations of varying k_b^{NA} to calculate $\underline{S}_{tot}^{NA}$ and optimize r^2 is conducted per nucleic acid (Figure 4.5a), determining the optimized binding site compositions for each nucleic acid (Figure 4.5b, Table 4.1). The r^2 value between the optimized, weighted composition of the simulated Raman spectra in comparison to the experimental measurement is higher for each nucleic acid when compared to the single binding site values of r^2.

Table 4.1. Optimized molecular composition and corresponding r^2. Coefficients of determination for 18 single atom binding systems and the 4 optimized weighted composition binding site systems. The coefficient of determination increases when accounting for a mixture binding sites for each nucleic acid, such as thymine which went from a r^2 value of 0.52 (T-N1) to a value of 0.84 (48% T-N1, 14% T-N3, 9% T-O2, 29% T-O4).

Binding Site	r^2 of Adenine	r^2 of Cytosine	r^2 of Guanine	r^2 of Thymine
N1	0.20	0.06	0.21	0.52
N3	0.73	0.71	0.78	0.44
N7	0.14		0.57	
N9	0.62		0.55	
NH_2	0.02	0.16		
O2		0.11	0.28	0.45
O4				0.41
Weighted Mixture	**0.85**	**0.81**	**0.91**	**0.84**
Optimized Compositions	37% N3 31% N7 30% N9 2% NH2	9% N1 63% N3 26% NH2 2% O	32% N1 40% N3 12% N7 16% N9	49% N1 13% N3 9% O2 29% O4

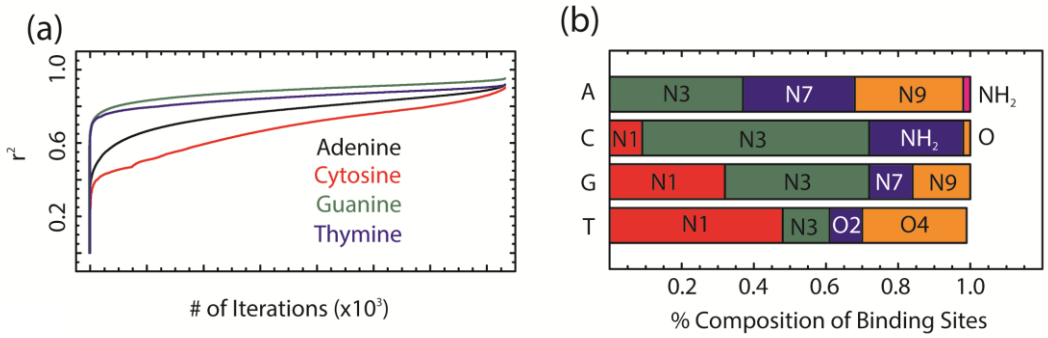

Figure 4.5. Optimizing r^2 with SRCS. (a) The increase in the coefficient of determination (r^2) as the number of iterations increases, resulting in r^2 near 1, for the nucleic acids adenine (black), cytosine (red), guanine (green), and thymine (blue). (b) The optimized percent composition of each binding site to silver at the maximum coefficient of determination for each nucleic acid. Adenine shows the majority of binding comes from N3, N7, and N9. Cytosine is primarily bound to silver via the N3 atom. Guanine's strongest binding atoms are N1 and N3. Thymine is strongly bound via the N1 and O4 atoms.

To visually compare the effectiveness of the SRCS process, the individual weighted binding site Raman spectra $k_b^{NA}\underline{S}_b^{NA}$, the superimposed cumulative simulated Raman spectrum $\underline{S}_{tot}^{NA}$, and the experimental Raman spectrum $\underline{E}^{NA}$ are plotted (Figure 4.6). When comparing the superimposed simulated Raman correlation spectrum to the experimental measurement, qualitative analysis clearly shows that the weighted composition calculated spectrum (gray) for each nucleic acid is in good agreement with the experimental Raman signature (black).

The high coefficients of determination and corresponding superimposed spectra demonstrate the efficiency of the SRCS process as a method to discover the preferential binding sites of each nucleic acid to silver. The preferential binding sites of adenine to silver are N3, N7, and N9, with limited binding from NH_2 and none from

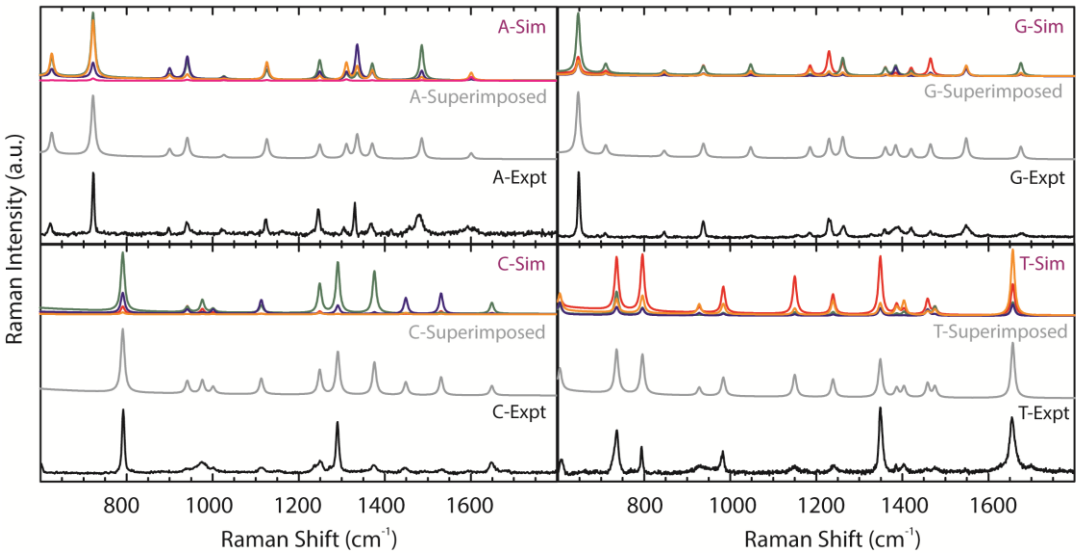

Figure 4.6. Superimposed simulated and experimental Raman spectra. The weighted simulated Raman spectra $k_b^{NA}\underline{S}_b^{NA}$ for each binding site (top in A, C, G and T; multicolored), the superimposed simulated Raman spectra $\underline{S}_{tot}^{NA}$ for all the binding sites (middle in A, C, G and T; gray), and the experimental measured Raman spectra $\underline{E}^{NA}$ for each nucleic acid (bottom in A, C, G and T; black).

N1. For cytosine, the preferred binding site is N3 with moderate binding from NH_2 and limited binding from N1 and O. The results of guanine demonstrate that there is no binding via the O atom, with moderate bonding from N1 and N3 and limited binding from N7 and N9. Finally, the N1 atom of thymine demonstrates the strongest binding to silver with roughly half of the molecules binding via the N1 site, with moderate bonding from O4 and limited bonding from N3 and O2.

To explain the preference of specific binding sites to nucleic acids, we examine the physical existence of nucleic acid tautomers in water. Because nucleic acids exist as several tautomers upon interaction with water, there are a significant number of potential binding atoms available to bind to silver depending on the location of the hydrogen atom for each tautomer. The tautomers determine the available binding sites,

such as when the N9H adenine tautomer enables the doubly bonded ring nitrogens to act as the preferential binding sites and electron donors, while prohibiting the N9 atom from binding to the silver surface. Thus, the composition of the preferential binding atoms is dependent on the prevalence of specific tautomers of the nucleic acids in water. For example, in the case of cytosine, it can be deduced that the N3H tautomer is present in a limited form in water because of the dominance of the N3 and NH_2 as binding sites. This agrees well with a previous study, which determined that upon cytosine hydration, the N1H tautomer formed much more frequently than the N3H tautomer, enabling the doubly bonded ring nitrogen group on N3 to bind, while prohibiting the N1H site to bind to silver [103]. Therefore, in addition to determining the composition of binding sites of nucleic acids to silver, the SRCS method can yield insight into the population of specific tautomers in water. Additional factors that can determine preferential binding sites are the electron densities of the molecules and the geometrical constraints caused by steric effects and will be addressed in future work.

4.5. Conclusion

In this chapter, we have developed and applied an SRCS statistical analysis method for determining the composition of binding atoms of nucleic acids to silver using a quantitative statistical analysis process that compares calculated Raman spectra to experimental measurements. We have demonstrated that the SRCS method can deduce the relative composition of binding sites and quantitatively determine that certain sites (e.g. N1 in adenine, O in cytosine) do not play a significant role in binding to silver, while others (e.g. N3 in adenine, N3 in cytosine), are the primary

binding sites with additional, less active binding sites (e.g. N7 and N9 in adenine, N1 in cytosine).

Using a weighted simulated Raman correlation spectroscopy method, we have developed a process to optimize the coefficient of determination for comparing simulated Raman data to experimental measurements by adjusting the composition of binding sites. By optimizing the composition of the potential binding sites, we show that a mixture of orientations and configurations occur during experimental measurements and provide a method to use for binding analysis. Additionally, we demonstrate the efficiency of our method by comparing the experimental measurements to the superimposed simulated Raman spectra, showing excellent agreement and a high coefficient of determination. Finally, we compare the composition of binding atoms to previously published results. This method lays the foundation for using computational simulations to study the assembly and surface chemistry of molecules on the nanoscale level and can be applied to many fields of study, including near-field characterization of molecule alignment and configuration of molecules with respect to metal surfaces.

This chapter is, in part, a reprint that the dissertation author was the principal researcher and author of. The material appears in *Scientific Reports.* (L.M. Freeman, A. Smolyaninov, L. Pang, Y. Fainman, "Simulated Raman correlation spectroscopy for quantifying nucleic acid-silver composites" *Scientific Reports*, 6, 23535, 2016.)

Chapter 5

Excitation of the Charge-Transfer Resonance of Nucleic Acids

5.1. Introduction

While the static polarizability effect offers unique insight into the molecular configuration of the nucleic acids binding to silver, the charge-transfer effect provides information regarding the optical properties of the systems themselves and supplies the explanation behind the Raman signature excitation energy dependence of nucleic acids functionalized to silver. Because adenine, cytosine, guanine, and thymine have unique molecular structures, the electron transfer between their molecular orbitals and the molecular orbitals of silver varies depending on the properties of each nucleic acid. Thus, the charge-transfer effect is wavelength dependent and can be optimized or eliminated by selecting the appropriate excitation wavelengths. In this chapter, we look at how the charge-transfer effect is dependent on two excitation wavelengths (532 nm and 785 nm) and the corresponding impact the charge-transfer effect has on the Raman signatures of cytosine and guanine.

Here, we report our findings on why there have been repeated discrepancies regarding the surface-enhanced Raman signal of DNA bases. We hypothesize that the differences in SERS nucleic acid intensities at different excitation wavelengths is caused by the charge-transfer effect that leads to resonance Raman scattering in which the excitation wavelength is resonant with the newly generated electronic transitions. Using cytosine and guanine as examples, we first perform time-dependent density functional theory (TD-DFT) calculations to determine the electronic transitions created between silver atoms and cytosine and guanine, and observe a clear shift as the absorption changes from the UV range for the base to the visible range for the base

metal system. We then verify the new absorption spectra using optical absorption measurements. [76] The resonance dependence on the electronic transition shift of cytosine and guanine metal systems reveal strong wavelength-dependent behavior of SERS signals. By matching plasmonic resonances of SERS substrates to the shifted electronic transitions of cytosine and guanine conjugated to the metal surface, we verify that the SERS signals can be modulated by selecting the appropriate excitation wavelength.

5.2. TD-DFT of Silver Cytosine and Guanine Systems

To demonstrate the differing optical properties of nucleic acids, cytosine and guanine are selected as the nucleic acids of interest. Cytosine, which has a single ring structure from the pyramidine group, has a single six-membered ring consisting of carbon and nitrogen. Guanine is composed of a double ring structure from the purine group and has a six-membered ring fused with a five-membered ring, both containing nitrogen and carbon atoms. Despite both being components of nucleic acids, they offer unique differences in molecular structure that reveal themselves in SERS charge-transfer measurements. By tuning the excitation wavelength, the Raman signature enhancement of cytosine and guanine can be selectively attenuated by matching the excitation wavelength with the electronic transitions of the respective systems.

Time-dependent density functional theory studies on the absorption properties of metal atom clusters with attached molecules have been previously utilized for understanding the charge-transfer effect that leads to a chemical enhancement when

the excitation energy is resonant with the electronic transition. [119,120] The studies that have been done on the chemical enhancement effect have used simple molecules such as pyridine [119] or benzenethiol, [29] and TD-DFT studies on nucleic acids primarily have been focused on geometrical adsorption studies with silver and adenine. [116,121] In order to calculate what electronic transitions are created when cytosine and guanine bind to silver atoms that lead to chemical enhancement in SERS, we perform TD-DFT simulations to measure the electronic transitions and relate the results to the chemical enhancement occurring in SERS experiments.

As previously discussed, TD-DFT simplifies density-functional theory to a time-dependent situation in which the system is exposed to a time-dependent perturbation, causing a change in the system's external potential. By measuring the response of the charge density to a perturbation, the oscillator strengths and transition energies can be calculated, in which the oscillator strength is defined as the probability of absorption between the energy levels of the molecule. [122] TD-DFT energy level calculations (Figure 5.1) are performed on cytosine, guanine, cytosine-silver (C-Ag), and guanine-silver (G-Ag) using the Gaussian 09 software. Geometry optimization, in which atoms are re-positioned until reaching an energy minimum, is performed on each system before TD-DFT calculations are used to ensure the systems are stable with no imaginary frequencies. [123] The silver cluster model chosen for the calculations is the 20-atom silver tetrahedral structure, as this has shown to have similar electronic properties as silver nanoparticles used in experiments [29,119,120] and is previously reported on in chapter 4 of this work.

Based on previous comparisons of simulations to experimental results, the flat side of the structure is chosen in which the molecule binds to the (111) surface of the Ag20 face-centered cubic (fcc) lattice structure. For TD-DFT simulations, B3LYP (Becke, 3-parameter, Lee-Yang-Parr) [108] is chosen as the DFT method as it employs both generalized gradient approximations and local-density approximations that are suitable for molecule-metal systems. [66,124] Based on the molecular

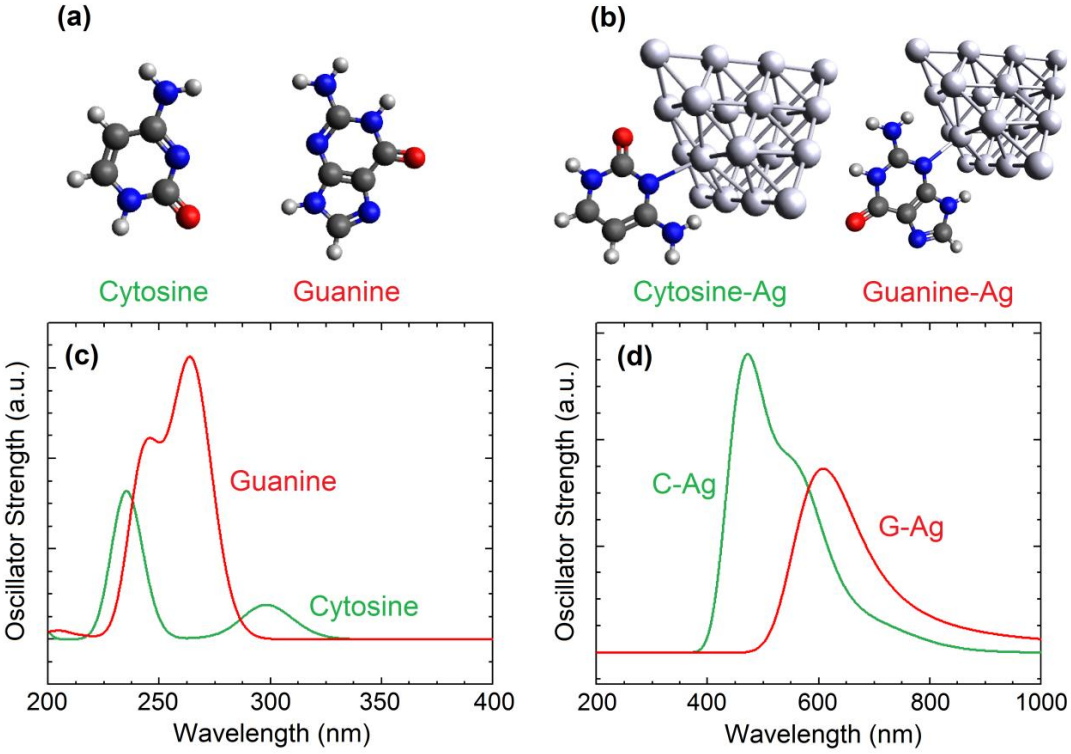

Figure 5.1. TD-DFT calculations of NA and NA-Ag. (a) Cytosine and guanine structures geometrically optimized, (b) C-Ag and G-Ag structures geometrically optimized, (c) UV-VIS absorption spectra of cytosine and guanine, and (d) UV-VIS absorption spectra of C-Ag and G-Ag. Cytosine and guanine have optical absorptions in the ultraviolet range, as expected based on previous experimental and simulation results. The addition of silver generates new electronic transitions in the visible range, with maximum oscillation strengths at 472 nm and 609 nm for C-Ag and G-Ag, respectively.

structures, a 6-31G(d,p) basis set is used for the isolated nucleic acids and a split basis set of 6-31G(d,p) and LANL2DZ is used for the nucleic acid molecules and silver atoms, respectively, for the DNA base metal systems.

As expected, the UV-visible absorptions for both cytosine (Figure 5.1c, green, with a peak at wavelength of 235 nm) and guanine (Figure 5.1c, red, with a peak at wavelength of 263 nm) are in the ultraviolet range as these are the natural electronic transitions of the molecules. However, when the nucleic acids are attached to the silver cluster, the absorption shifts into the visible range for C-Ag (Figure 1d, green, with a peak at wavelength of 472 nm) and G-Ag (Figure 1d, red, with a peak at wavelength of 609 nm), respectively.

The change in the absorption maxima corresponds to a change in the electronic transitions of the system, showing that new charge-transfer bands are created between the Fermi energy level of the metal and the highest occupied molecular orbital (HOMO) of the nucleic acids (Figure 5.2a). In order to confirm the calculated C-Ag and G-Ag electronic transitions, optical absorption measurements are performed on thin 20 nm Ag films with cytosine, guanine, and a mixture functionalized to the surface (Figure 5.2b). The measured C-Ag CT band (green) and G-Ag CT band (red) absorption intensity maxima occur at wavelengths of 566 nm and 662 nm, respectively. A Mix-Ag CT is also recorded (black), and correlates well to when the experimental measurements of C-Ag and G-Ag are combined (blue dotted line).

The experimentally measured absorption spectra show that the CT bands corresponding to the experimental data are fairly consistent with the absorption spectra

simulations (Figure 1c,d). However, there are some differences in the simulation results and experimental measurements because only one adsorption configuration is used for the absorption band calculations. First, the experimental measurements show a red-shift of peak wavelength by 94 nm for C-Ag (simulation peak at wavelength of 472 nm, experimental peak at wavelength of 566 nm) and 53 nm for G-Ag (simulation peak at wavelength of 609 nm, experimental peak at wavelength of 662 nm). Second, using only one adsorption configuration results in narrower absorption bands ($FWHM_{C\text{-}Ag}$ = 161 nm, $FWHM_{G\text{-}Ag}$ = 135 nm) as opposed to experimental results ($FWHM_{C\text{-}Ag}$ = 192 nm, $FWHM_{G\text{-}Ag}$ = 204 nm). It is expected that additional adsorption configurations, such as attachment of the nucleic acid atom to the vortex of the silver atom cluster rather than to the surface face, or attachment *via* atoms other than the nitrogen ring atoms, would lead to shifts in the absorption bands. The

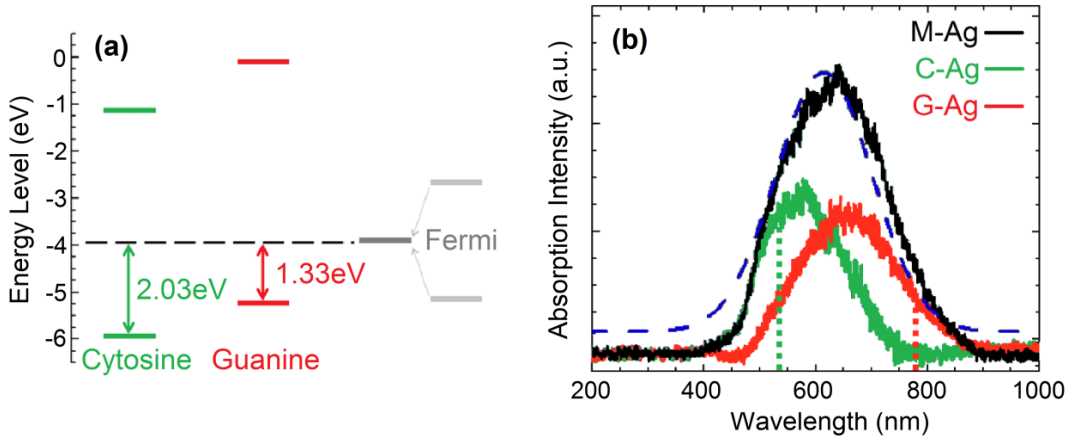

Figure 5.2. Fermi levels and experimental absorption measurements. (a) The electronic transitions created during electron transfer between the HOMO of the molecule and the Fermi energy of the silver. (b) Optical absorption measurements of cytosine (green), guanine (red), and mixture (black) on 20 nm Ag thickness, with values of 566 nm and 662 nm for C-Ag and G-Ag, respectively. The addition of C-Ag and G-Ag measurements is represented by the blue dotted line. The Raman excitation wavelengths (532 nm and 785 nm) are marked by the vertical dotted lines.

convolution of the calculated absorption bands of all adsorption configurations would lead to the simulation results matching the experimental measurements. For this reason, the measured experimental results are assumed to be more representative of the CT bands of the system as opposed to the simulation results.

The regions where the C-Ag and G-Ag show strong oscillation strength and absorption intensities correlate to the new electronic transitions created by the charge-transfer between the metal and nucleic acids. The optical absorption spectra have full-width half maxima (FWHM) of ~250 nm, in which case there will be a chemical enhancement mechanism occurring between approximately 441 nm to 691 nm for C-Ag and 537 nm to 787 nm for G-Ag. From these results, we can substantiate our hypothesis that the enhancement difference found between the two nucleic acids in previously published results was caused by the induced Raman scattering in different excitation wavelengths used in the experiments, rather than by the difference in Raman-cross sections or orientation of the molecules.

5.3. Localized Surface Plasmon Resonance (LSPR) of Silver Island Films

In order to demonstrate the effect charge-transfer bands have on enhanced Raman signals when in resonance with the excitation wavelength, surface-enhanced Raman spectroscopy is performed with nucleic acids functionalized on silver islands. Due to experimental constraints, the laser wavelengths chosen are 532 nm and 785 nm (marked in Figure 5.2b, vertical dotted lines). Based on optical absorption measurements shown in Figure 5.2b, the 532 nm excitation wavelength will show

strong chemical resonance of C-Ag and weak chemical resonance of G-Ag, while the 785 nm excitation wavelength will demonstrate no chemical resonance of C-Ag and weak chemical resonance of G-Ag. The silver island films are fabricated in such a way that their plasmonic resonance, which leads to a local electric field enhancement, is in the same wavelength range as the Raman excitation wavelength. In this way, both the plasmonic electromagnetic enhancement and charge-transfer chemical enhancement will be resonant in the same wavelength range, offering the maximum possible resonance Raman effect with the appropriate wavelength selection.

Silver island films (AgIFs) are chosen as SERS substrates because they offer highly controllable, uniform and reproducible surfaces that can be tuned for electromagnetic enhancement at any wavelength using Nanosphere Lithography (NSL). [125] Two substrates are designed: substrate #1 has a 300 nm bead mask (75 nm side length) and a 45 nm silver thickness and substrate #2 has a 500 nm bead mask (135 nm side length) and a 60 nm silver thickness. The corresponding SEM images of substrate #1 and #2 are shown in Figure 5.3a. Finite element modeling (FEM) simulations are performed (COMSOL Multiphysics software package) to calculate the local electric field enhancement of both substrates (Figure 5.3b). COMSOL simulations with silver islands are modeled in an air environment (refractive index n = 1) on a silicon substrate (n = 3.5) with light propagation in the z-direction using incident wavelengths of 532 nm (1) and 785 nm (2) and an initial unpolarized electric field strength of 1 V/m. A spherical perfectly matched layer (PML) with a radius of 1 μm and a thickness of 200 nm absorbs scattered light. The silver islands use extremely

fine meshing. Simulations show strong field enhancement at the tips of the silver islands.

For the silver island films to enhance the Raman signal, the two substrates must support localized surface plasmon resonances (LSPR) that lead to local electric field enhancement. The wavelength range in which the silver island films support the LSPR depends on the size and shape of the silver particles and can be determined by measuring the scattering of the particles with broadband excitation. Optical absorption and scattering spectra are recorded using a broadband UV-visible fiber optic illuminator and spectrometer (Ocean Optics HR4000). Spectra are normalized with respect to the background silicon signal. Five spectra are taken for scattering

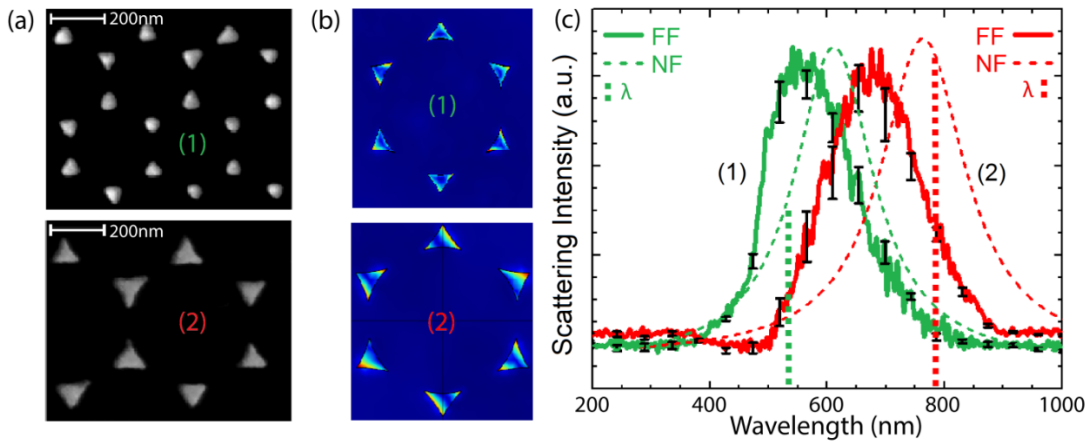

Figure 5.3. SEM, COMSOL simulations, and extinction spectra of AgIFs. (a) SEM images of substrates. (b) COMSOL simulations of substrate #1 (300 nm bead mask, 75 nm side length, 45 nm thickness) and of substrate #2 (500 nm bead mask, 135 nm side length, 60 nm thickness). (c) Localized surface plasmon resonance scattering far field (FF) spectra of substrate #1 (green line, λ_{LSPR} = 569 nm) and substrate #2 (red line, λ_{LSPR} = 679 nm) and near field (NF) spectra of substrate #1 (green dashed line, λ_{NF} = 622 nm) and of substrate #2 (red dashed line, λ_{NF} = 763 nm). The excitation wavelengths for the SERS experiments are represented by the green (532 nm) and red (785 nm) vertical dotted lines. Error bars represent the scattering intensity deviation of the 5 LSPR measurements recorded.

measurements and the mean intensity is plotted with respect to wavelength. Error bars represent the standard deviation of the five intensity measurements. The scattering spectra for the two silver island film substrates are shown in Figure 5.3c, with a larger feature size for substrate #2 leading to a red-shift of the λ_{LSPR}.

When we use the above fabricated silver island film as the substrates for DNA (*e.g.*, cytosine, guanine) Raman measurements, both the chemical enhancement from the induced resonance Raman from C-Ag or G-Ag and the electromagnetic enhancement from the LSPR would contribute to the total Raman scattering signal. By measuring the intensity of the absorption of the nucleic acid silver systems (Figure5.2b) and the scattering of the LSPR from the pure silver island films (Figure 5.3c), the respective chemical enhancement and electromagnetic enhancement contributions can be estimated.

For calculating the electromagnetic contribution, the near field intensity distribution should be considered. The scattering results shown in Figure 5.3c in green and red (solid lines) are actually far field measurements. Fortunately, it is known that the far field spectra response deviates from the near field spectral distribution due to internal and radiative damping,[24] in which the near field local intensity enhancement maximum is red-shifted from the far field LSPR measurement. Using the model based on damped harmonic oscillators,[25] we calculate the damping factor for substrates #1 and #2. The damping factor (β) is found using the relationship $\beta=w/(2\pi)$, where w is the full width at half maximum (FWHM) of the Lorentzian fit of the far field measurements. The red-shifted near field ω_{NF} is then calculated from $\omega_{NF}=(\omega_0^2-$

$\beta^2/2)^{1/2}$. The damping effect leads to near field resonant wavelengths of 622 nm and 763 nm from far field resonant wavelengths of 569 nm and 679 nm, for substrates #1 and #2, respectively. The shifted near field intensity spectra are shown in Figure 5.3c (dashed lines).

The results of the chemical and electromagnetic contributions based on the absorption intensities and LSPR intensities with near field red-shift corrections are shown in table 5.1, with the intensities normalized to the maximum total contribution (G-Ag on substrate #2 at 785 nm). For example, the absorption intensity for 532 nm C-Ag is 203 a.u. and the scattering intensity is 164 a.u., resulting in chemical and plasmonic contributions of 0.48 and 0.39, respectively. From the total contribution estimation, we expect to see the Raman enhancement results at 532 nm to be C-Ag > G-Ag and at 785 nm to be G-Ag > C-Ag.

Table 5.1. Chemical and plasmonic contributions. Chemical and plasmonic contributions for the SERS excitation wavelengths of 532 nm and 785 nm, with the intensities normalized with the total maximum of the two contributions

	Chemical Contribution	**Plasmonic Contribution**	**Total**
532 nm C-Ag	0.48	0.39	0.87
532 nm G-Ag	0.21	0.39	0.60
785 nm C-Ag	0	0.75	0.75
785 nm G-Ag	0.25	0.75	1

5.4. Surface-enhanced Raman Spectroscopy Measurements

To demonstrate the dependence of the enhanced Raman signatures of cytosine silver and guanine silver on the excitation intensity, surface-enhanced Raman measurements of the systems are performed. Both the 532nm and 785nm wavelengths are employed, in which the 532nm is expected to have a strong and moderate charge-transfer effect for cytosine and guanine, respectively, while the 785nm is expected to have a minimal and weak charge-transfer effect for C and G, respectively.

For SERS measurements, cytosine and guanine (VWR International) are dissolved in H_2O for resulting concentrations of 3 mM. This solution is then drop coated on the 1 cm^2 silver island film substrates (substrate #1 and #2) and allowed to be incubated overnight. The samples are then rinsed to remove bulk unattached nucleic acids on the surface, leaving behind approximately a monolayer of adsorbed cytosine or guanine molecules on the silver islands.

Raman spectroscopy is performed using a Renishaw Raman spectrometer at the wavelengths of 532 nm and 785 nm. Spectra are recorded using the hyperSpec program. The sample is imaged using a 40x objective, and the area which data are acquired is confirmed to contain silver island films with nucleic acids by using markers and SEM verification. The laser power of each wavelength is calibrated by comparing the intensity of the 500 cm^{-1} mode of a Si wafer. A 10 second acquisition time is used with a Raman spectral range of 600 cm^{-1} to 2000 cm^{-1} to eliminate the 500 cm^{-1} line from Si. Baseline subtraction is then performed to ensure that all spectra are level with the x-axis.

Raman spectroscopy is performed at 532nm and 785nm for C-Si, G-Si, C-Ag, and G-Ag, where concentrated cytosine and guanine are functionalized on silicon for SERS comparison to normal Raman scattering (NRS). For analysis, the ring-breathing modes (RBM) of cytosine and guanine (~790 cm^{-1} and ~650 cm^{-1}, respectively), the single bond stretching modes (SSM) of cytosine and guanine (~1290 cm^{-1} and ~1230 cm^{-1}, respectively), and the double bond stretching modes (DSM) of cytosine and guanine (~1650 cm^{-1} and ~1550 cm^{-1}, respectively) are selected for analysis as these are the standard modes used for DNA Raman spectroscopy measurements. [92,93]

With an excitation wavelength of 532 nm on substrate #1 (Figure 5.4a), cytosine (C-Ag) is shown to have a stronger surface-enhanced Raman signal than guanine (G-Ag) based on the RBM, SSM and DSM. The bulk Raman signals of cytosine (C-Si) and guanine (G-Si) functionalized on a clean silicon wafer are also taken for comparison, showing that the NRS signals have consistent intensities between the two nucleic acids at both wavelengths. The results are directly opposite for an excitation wavelength of 785 nm on substrate #2 (Figure 5.4b), in which the surface-enhanced signals of the RBM, SSM, and DSM for substrate #2 of G-Ag are shown to be larger than that of C-Ag due to the signal enhancement caused by the chemical enhancement, a resonance Raman effect. The NRS shows the RBM of C-Si and G-Si to have approximately the same intensity, as expected, due to the absence of silver and thus no charge-transfer resonance.

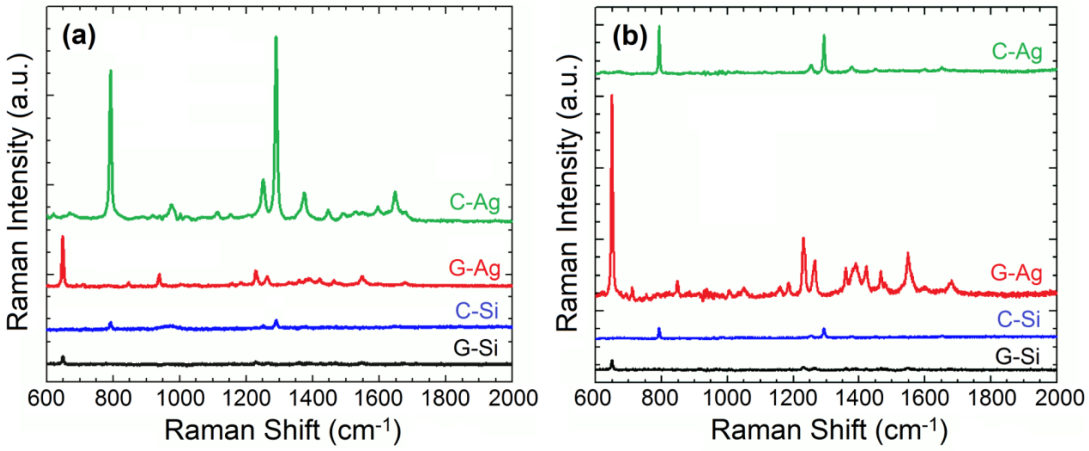

Figure 5.4. SERS and Raman spectra of cytosine and guanine. (a) Raman spectra of cytosine and guanine on Raman and SERS substrates with an excitation wavelength of 532 nm using substrate #1, with NRS measurements on silicon showing low Raman intensities and SERS measurements showing that C-Ag has a greater intensity than G-Ag. (b) Raman spectra of cytosine and guanine on Raman and SERS substrates with an excitation wavelength of 785 nm using substrate #2, with NRS measurements on silicon showing low Raman intensities and SERS measurements showing that G-Ag has a greater SERS intensity than C-Ag.

The ratios of the surface-enhanced Raman intensities (C-Ag, G-Ag) to the normal Raman scattering intensities (C-Si, G-Si) for the RBM, SSM and DSM modes at both 532 nm (green) and 785 nm (red) excitation wavelengths give quantitative evidence that all modes are consistently higher for C-Ag at 532 nm and G-Ag at 785 nm. The measured ratios of the Base-Ag to the Base-Si for all modes and wavelengths are shown in Figure 5.5. At 532 nm, C-Ag shows higher enhancement than G-Ag, with a RBM intensity ratio over C-Si and G-Si to be 18.0 and 5.53, respectively. At 785 nm, the opposite is seen as the ratio of RBM intensity of C-Ag to C-Si and G-Ag to G-Si are 4.38 and 19.1, respectively. The SSM and DSM results are also consistent with these findings.

We conclude that this change in Raman intensity magnitude of the RBM, SSM, and DSM of the nucleic acids is caused by the presence of the nanoscale metal substrate, as the normal Raman scattering (NRS) shows approximately equivalent intensities of the RBMs for C-Si and G-Si at 532 nm (453 a.u. and 454 a.u., respectively, in Figure 5.4a) and for C-Si and G-Si at 785 nm (301 a.u. and 281 a.u., respectively, in Figure 5.4b). This further confirms that the discrepancy seen in literature in which nucleic acids have varying SERS intensities at different wavelengths while having the same NRS intensities at these wavelengths is caused by the charge-transfer between the metal and nucleic acid, known as the chemical enhancement effect of SERS.

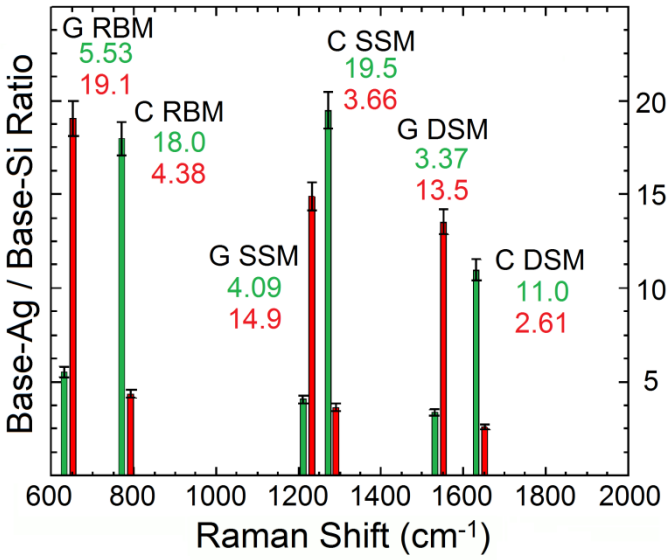

Figure 5.5. Bar graph of Base-Ag and Base-Si ratios. Bar graph displaying the ratios of Ag-Base to Si-Base at 532 nm (green) and 785 nm (red) excitation wavelengths for the guanine RBM (650 cm^{-1}), cytosine RBM (790 cm^{-1}), guanine SSM (1230 cm^{-1}), cytosine SSM (1290 cm^{-1}), guanine DSM (1550 cm^{-1}), and cytosine DSM (1650 cm^{-1}). The modes for cytosine have greater enhancement at 532 nm excitation and the modes for guanine have greater enhancement at 785 nm excitation.

5.5. Conclusion

Although SERS has previously been performed with nucleic acids, the measured intensities for each nucleic acid have varied significantly depending on the SERS substrate and excitation wavelength. We have demonstrated that the charge-transfer (CT) mechanism, also known as the chemical enhancement of SERS, is responsible for the discrepancies previously reported in literature. The electronic states of cytosine and guanine attached to silver atoms are computationally calculated and experimentally measured to be in the visible range, which leads to a resonance Raman effect at the corresponding maximum wavelengths. The resulting SERS measurements are in good agreement with the simulated values, in which silver cytosine shows stronger enhancement at 532 nm and silver guanine shows stronger enhancement at 785 nm. These findings suggest the optimal SERS signal can be achieved by tuning the excitation wavelength to match both the electromagnetic and chemical resonances, paving the way for future single molecule detection of nucleic acids other than adenine. In this next chapter, we further corroborate our findings using thin films of aluminum oxide to eliminate the charge-transfer effect.

This chapter, in part, is a reprint that the dissertation author was the principal researcher and author of. The material appears in *ACS Nano*. (L.M. Freeman, L. Pang, Y. Fainman, "Maximizing the electromagnetic and chemical resonances for surface-enhanced Raman spectroscopy of nucleic acids" *ACS Nano*, 8, 8, 8383-8391, Aug. 2014.)

Chapter 6

Elimination of the Chemical Resonance via Atomic Layer Deposition

6.1. Introduction

To further understand the role the charge-transfer effect has on the chemical enhancement in SERS for nucleic acid silver systems, we introduce aluminum oxide as a material capable of preventing charge-transfer from occurring. By eliminating the ability of electrons to transfer from the molecular orbitals of the molecules to the silver, the generation of new electronic transitions does not occur and thus the chemical resonance caused by the charge-transfer of electrons is reduced. Therefore, we can extrapolate the effect the chemical resonance has on nucleic acids. In this chapter, we use a thin layer of aluminum oxide to prevent electron transfer and thus remove the resonance CT band, and then experimentally validate our results with SERS measurements to predict the chemical enhancement factor

Multiple mechanisms have been proposed to not only prevent charge-transfer from occurring, but to also measure the distance dependence of SERS as molecules move further away from the localized electromagnetic field hot spot. Early research utilized Langmuir-Blodgett monolayers, in which monolayers would be grown on the surface of metal island films and the corresponding SERS signals of phthalocyanine were measured [126]. As expected, the more spacer layers that self assemble onto the surface leads to a decrease in SERS signal intensity as the molecules move further from the electromagnetic field. Additionally, polymers [127] and self assembled monolayers (SAMs) [128] can be used for the distance dependence measurements or the elimination of the chemical enhancement. However, these can have strong Raman signatures which can interfere with the detected SERS signals. In this chapter, we

utilize aluminum oxide (Al_2O_3) as our spacer layer that prevents the electron transfer to occur and suspends the chemical enhancement effect measured in SERS.

In order to estimate this chemical enhancement effect, it is possible to sputter an atomic layer of aluminum oxide *via* atomic layer deposition (ALD) on the metal nanostructures that will prevent electron transfer between the metal and molecules [15]. In this way, the chemical resonance effect would be removed as there would be no charge-transfer bands created by electron re-distribution, causing a significant drop in the SERS intensities. Although Al_2O_3 or other thin films might cause a portion of the silver to oxidize and can be porous, researchers have successfully utilized Al_2O_3 for the elimination of the charge-transfer effect as well as for distance dependence studies, showing excellent correlation between simulations and experimental results [129,130]. The layer of aluminum oxide, compared to conventional thin film coatings, is actually highly stable to oxidation and temperature changes.

Previously published results have demonstrated the efficacy of using Al_2O_3 to measure the electromagnetic field decay as molecules move away from the surface. By adding several layers of Al_2O_3, Van Duyne *et al.* monitored the SERS intensity decay as the molecules were placed further away from the surface and experimentally measured the electromagnetic field strength as a function of distance from the surface [131]. In addition to the decrease caused by the distance between the nanostructure and molecule, there will also be a LSPR shift that will change the LSPR contribution. However, previous work has shown that only thick layers result in a

substantial LSPR shift (~30 nm for 120 nm shift) [132], thus an ultrathin layer will have a minimal impact on the LSPR shift. [129,133–135] Based on the successful demonstrations of using Al_2O_3 as a spacer layer, a 1 nm thick layer of aluminum oxide is assembled onto the substrates in order to eliminate the charge-transfer between the metal and molecules.

6.2. Electromagnetic Field Reduction from Thin Film Deposition

Aluminum oxide was selected as the electron transfer prevention material because of its controllable deposition, compatibility with the substrates, and weak Raman signal interference. Additionally, the aluminum oxide prevents silver oxidation and has shown to have a minimal effect on reduction of electromagnetic enhancement. Aluminum oxide is the ideal material to use for determining the impact the prevention of the chemical enhancement effect and what order of magnitude the chemical enhancement effect has in SERS.

To begin, we use COMSOL simulations to calculate the dampening of the electromagnetic effect caused by a thin 1 nm layer of Al_2O_3 for silver island films (Figure 6.1). COMSOL simulations with silver islands are modeled in an air environment (refractive index n = 1) on a silicon substrate (n = 3.5) with light propagation in the z-direction using incident wavelengths of 532 nm (1) and 785 nm (2) and an initial unpolarized electric field strength of 1 V/m. A spherical PML with a radius of 1 μm and a thickness of 200 nm absorbs scattered light. The silver islands

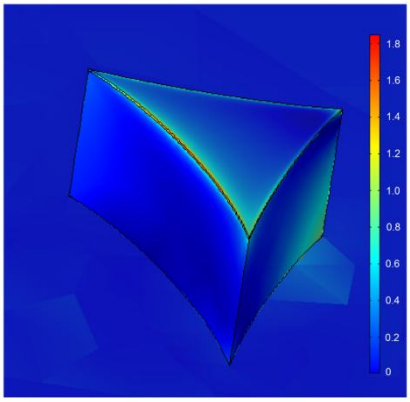

Figure 6.1. COMSOL Simulations of AgIFs. COMSOL result of silver island films with the Al_2O_3 layer

and 1 nm thick layer of aluminum oxide use extremely fine meshing and all other elements use fine meshing.

The 1 nm thick layer results in a decreased electromagnetic effect as the molecules rest 1 nm away from the maximum localized electric field. The simulation results show a decrease by 26.9% for substrate #1 and 23.0% for substrate #2, meaning the dampened plasmonic resonance will cause a moderate dip in the enhanced Raman signals due to the reduction of the electromagnetic field enhancement. The simulation results agree well with previously published experimental measurements of the electromagnetic field decay caused by spacer layers. [130,131] Because the aluminum oxide prevents electron transfer and thus prevents a chemical enhancement from occurring, we expect to see a much more significant decrease in the Raman signals for substrates which previously demonstrated strong chemical enhancement (Chapter 5, C-Ag at 532 nm, G-Ag at 785 nm).

To determine the field enhancement decay experimentally, aluminum oxide is sputtered onto silver island films. The fabrication process for the silver island films is outlined in Chapter 5 for both substrates #1 and #2. After the fabrication process is complete, aluminum oxide is sputtered onto the silver island films using ALD (Beneq TFS200, Calit2 Nano3 Cleanroom, UCSD) to a thickness of 0.99 nm in order to eliminate the chemical enhancement effect. Trimethylaluminum (TMA) and H_2O vapors are alternatively pulsed through the chambers at a temperature of 250° C with an average rate of 0.9 Å/cycle for 11 cycles.

To experimentally measure the effect aluminum oxide has on the electromagnetic field enhancement, we use fluorescent dye to detect the intensity decay between samples. Two samples are fabricated: silver islands without aluminum oxide and silver islands with a 0.99 nm layer of aluminum oxide, both of which are optimized for a 785 nm excitation wavelength (substrate #2 from Chapter 5). Alexa Fluor 790 dye was used to measure the fluorescent intensity with an excitation wavelength of 785nm using a standard fluorescent microscope.

Figure 6.2 shows the bright field images of the substrate with and without ALD, as well as the corresponding fluorescence image. Under bright field, the bright spots represent the areas where the beads did not dissolve and the dark areas are the sections where the silver island films are located. The fluorescence measurements display strong fluorescent intensities where the dark spots are in the bright field images due to the presence of the silver islands. The fluorescent measurements of Figure 6.2b and 6.2d are converted to grayscale values. The average pixel intensity is

found after ignoring all dark spots (pixel intensity >5), with average values of 107 and 91 found for Figure 6.2b and 6.2d, respectively. Thus, the 1 nm thick layer of Al2O3 shows a ~18% decrease in the fluorescent intensity, agreeing well with the simulation results.

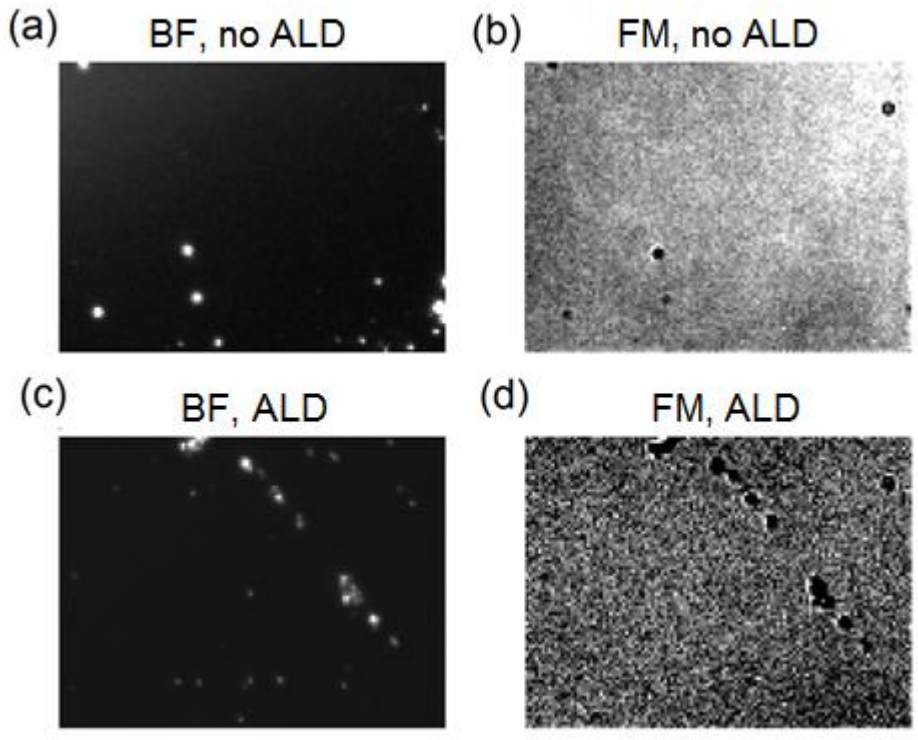

Figure 6.2. Field enhancement of AgIFs with and without Al2O3. (a) Bright field (BF) of silver islands without aluminum oxide layer, (b) corresponding fluorescent measurement (FM) of silver islands without aluminum oxide layer, (c) BF of silver islands with 1 nm layer of aluminum oxide, (d) FM of silver islands with 1 nm layer of aluminum oxide, showing decrease in fluorescent intensity compared with a to b.

6.3. Elimination of the Charge-Transfer Effect for SERS

As reported previously, the oxidation caused by this process will lead to a slight red shift of the λ_{LSPR} by ~13 nm, [135] which would slightly decrease the

plasmonic resonance effect by roughly 10%. With the dampened plasmonic resonance and LSPR shift, we expect to see a decrease of ~30% - 40% when there is no chemical resonance present. If there is a chemical resonance, such as at 532 nm with C-Ag, we expect to see a much larger drop as new electronic transitions are not formed by the exchange of electrons. To measure the change in SERS intensity, 8 silver island film samples are prepared; 4 for 532 nm (substrate #1) and 4 for 785 nm (substrate #2). Two samples at each wavelength are sputtered with Al_2O_3 (1 with cytosine and 1 with guanine) and two are left clean without an Al_2O_3 layer. The resulting Raman measurements are shown in Figure 6.3.

From the 532 nm (substrate #1) results (Figure 6.3a), the clean cytosine sample shows a high RBM magnitude. When a 1 nm thick Al_2O_3 layer is added to the surface, this intensity decreases by 83.4% , which is a much higher drop than expected and is caused by the elimination of the charge-transfer band that leads to a chemical enhancement. However, for guanine, which sees a weak chemical enhancement at 532 nm, the 1 nm thick layer only causes a RBM Raman intensity decrease by 48.3% compared to the clean guanine sample, which agrees well with the effect on the plasmonic resonance caused by distance dependence and elimination of a weak chemical resonance. For the 785 nm results (substrate #2, Figure 4c), the opposite is seen as the guanine SERS measurement decreases by 84.7% compared to the clean sample and the cytosine Al_2O_3 measurement decreases by 36.1% compared to the clean sample. This confirms that cytosine does not have a strong chemical

enhancement at 785 nm, while guanine does have some chemical enhancement at 785nm.

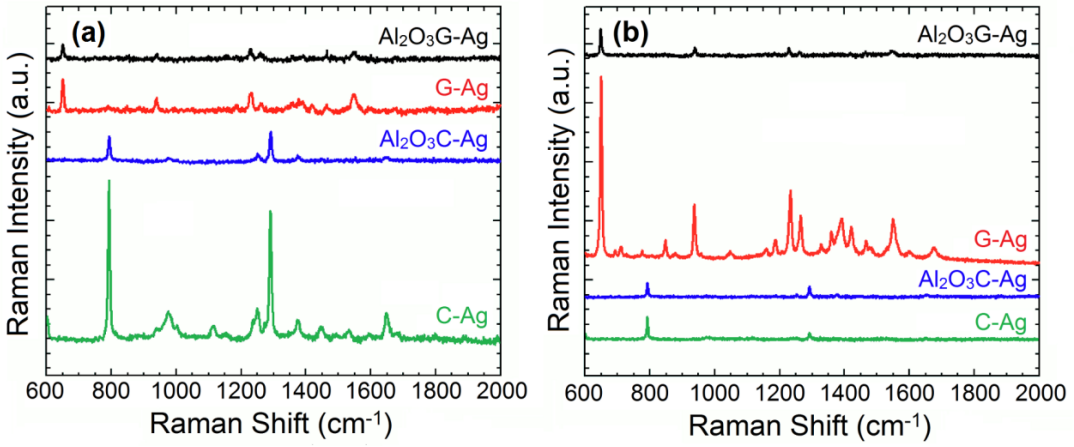

Figure 6.3. SERS spectra with and without Al_2O_3, (a) SERS results of cytosine and guanine at an excitation wavelength of 532 nm (substrate #1) with a clean sample and a sample with an aluminum oxide coating. C-Ag shows a much larger drop with the addition of the aluminum oxide layer. (b) SERS results of cytosine and guanine at an excitation wavelength of 785 nm (substrate #2) with a clean sample and a sample with an aluminum oxide coating. Unlike at 532 nm, G-Ag shows a much larger drop than C-Ag after ALD.

A summary of the percent decrease for all Raman modes can be found in Figure 6.4. The SSM and DSM of cytosine at 785 nm have the least amount of percent change when adding the atomic layer of aluminum oxide because these modes lie further from the excitation line (1290 cm^{-1} and 1650 cm^{-1}). Based on the values in Figure 6.4, the chemical enhancement appears to be less than 10, which correlates well to previously published research results. [136] Although this value seems low, it leads to a dramatic difference in Raman spectra, particularly because the plasmonic resonance will always have the same order of magnitude effect on different molecules.

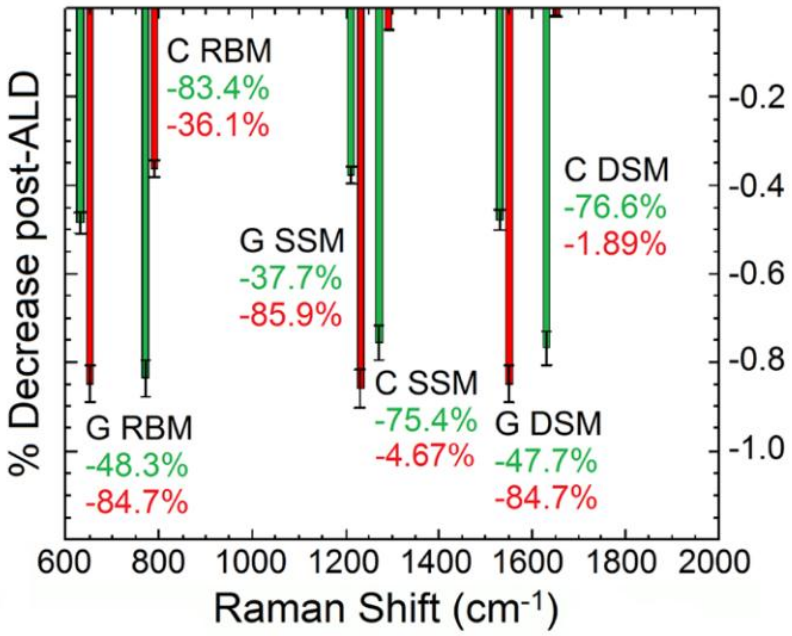

Figure 6.4. Bar graph of decrease in Raman intensities. Bar graph displaying the percent decrease in Raman intensities of the RBM, SSM, and DSM of cytosine and guanine after addition of atomic layer of aluminum oxide. G-Ag modes show much larger drops with the 785 nm excitation wavelength (red) and C-Ag modes show much larger drops with the 532 nm excitation wavelength (green). This correlates with our findings, as the atomic layer prevents electron transfer and leads to a more dramatic decrease in Raman intensity for substrates that previously displayed strong chemical resonances.

The chemical resonance, since it varies from molecule to molecule, can lead to drastic differences in the SERS signal and thus can make some molecules undetectable.

6.4. Conclusion

We have shown that the charge-transfer mechanism has been responsible for the failure to obtain accurate SERS measurements on DNA bases, as well as the inability to perform SM-SERS measurements on nucleic acids other than adenine. We have successfully demonstrated that new electronic states of nucleic acid silver systems are created in the visible range and differ for different nucleic acid metal

systems. We then experimentally verified the creation of new electronic transitions by performing optical absorption measurements on cytosine and guanine attached to silver. We showed that by tuning the excitation frequency, the enhancement of the SERS signal for C-Ag and G-Ag will change based on the charge-transfer bands of each molecule-metal system being resonant with the excitation frequency. These results confirm that the variance of the SERS signal in nucleic acids comes from the charge-transfer mechanism, rather than differences in the Raman cross-section or orientation of the molecules. This chemical enhancement effect can vary dramatically for two similar molecules, as seen with cytosine and guanine. By identifying the reason of amplification differentiation, we believe that future work would enable all nucleic acids to be measured using SERS by tuning the excitation wavelength. With additional TD-DFT studies and optical absorption measurements on the other nucleic acids in conjunction with these results, we predict that it will be possible to perform SM-SERS when the excitation energy is appropriately optimized for the nucleic acid in question.

Broadband SERS substrates or multi-resonances SERS substrates can be utilized as tools for achieving the amplified SERS charge-transfer band intensities at multiple wavelengths and thus will be the focus of our future work. Only two nucleic acids were chosen for this work to simplify the results, so future work must also take into account the other two nucleic acids (adenine and thymine). While there are many challenges that remain for a Raman based sequencing method such as spatial resolution and poor signal-to-noise ratio (SNR) which can be addressed by statistical

analysis, the issue of surface-enhanced Raman intensity can be resolved as being wavelength dependent and caused by the charge-transfer resonances of the system.

This chapter, in part, is a reprint that the dissertation author was the principal researcher and author of. The material appears in *ACS Nano*. (**L.M. Freeman**, L. Pang, Y. Fainman, "Maximizing the electromagnetic and chemical resonances for surface-enhanced Raman spectroscopy of nucleic acids" *ACS Nano*, 8, 8, 8383-8391, Aug. 2014.)

Chapter 7

Final Thoughts and Future Directions

7.1. Summary of Contributions

In this dissertation, I have studied the static Raman polarizability and charge-transfer effect of the chemical enhancement SERS mechanism as it pertains to nucleic acid-silver composites. A method was developed to estimate the preferential binding atoms of nucleic acids to silver by quantitatively comparing experimental Raman measurements with simulated time-dependent density functional theory calculations of Raman frequencies. The charge-transfer effect was then analyzed as it pertains to nucleic acid-silver composites and determined that the chemical enhancement of cytosine and guanine functionalized to silver is a function of the Raman excitation wavelength.

After introducing Raman spectroscopy, surface-enhanced Raman spectroscopy, and the unique properties of nucleic acid-silver composites in Chapter 2, the simulated time-dependent density functional theory Raman spectra of 18 nucleic acid-silver composite systems are shown in Chapter 3. The TD-DFT plots are complimented by experimental measurements of nucleic acids functionalized to random silver films, which offer a minimal Raman electromagnetic effect at a wavelength excitation of 785 nm. Thus, the experimental Raman signatures are primarily a function of the static polarizability effect. The spectral features of each plot were discussed in detail, and the conclusion that the simulated Raman spectra varied from the corresponding experimental measurement was made.

In Chapter 4, a new approach to analyzing the TD-DFT spectra with respect to the experimental measurements was introduced. The simulated Raman correlation

spectroscopy process was described in detail. For each system, the individual TD-DFT spectrum was statistically compared to the experimental measurement, indicating poor correlation. A weighted composition of the simulated Raman spectra was then calculated by varying the weighted constants in order to optimize the coefficient of determination of the superimposed spectrum with the experimental measurement. The results are then shown, in which multiple binding sites for each nucleic acid are shown to contribute to binding.

The charge-transfer effect is discussed in Chapter 5, in which a hypothesis is made that the variation of nucleic acid Raman signals is caused by the new electronic transitions generated when nucleic acids bind to silver. Silver island films are fabricated that have an electromagnetic resonance with both the 532 nm and 785 nm excitation wavelength. Cytosine and guanine are functionalized onto the substrates and the SERS signals are measured, in which cytosine is shown to have amplification at 532 nm and guanine is shown to have amplification at 785 nm. The ratios of the ring breathing mode, single stretching mode, and double stretching mode for the two conditions are shown in the form of a bar graph.

The results of the charge-transfer effect for nucleic acid-silver composites are further corroborated in Chapter 6, in which a thin film of aluminum oxide is implemented to prevent electron transfer from occurring and isolate the chemical enhancement effect. An approximately 1 nm thick film of aluminum oxide is deposited on silver island films, and the effect on the Raman signal is measured. The prevention of electron transfer from occurring eliminates the charge-transfer

enhancement and leads to a reduction in the Raman signal. Thus, the charge-transfer effect on nucleic acid-silver composites is confirmed, in which the enhancement is dependent on the excitation wavelength.

7.2. Future Work

The chemical enhancement effect reveals important information about nucleic acid-silver composites that assists with characterization of the systems. For future work, I am interested in measuring the Raman signatures of linearized DNA strands on a smooth silver structure and detecting the dependence of the Raman signatures on the excitation wavelength. Because the electron structure varies between the nucleic acids, the charge-transfer effect will also change depending on the electron transfer. I hope to identify the composition of nucleic acids within a DNA strand by acquiring the Raman signature at multiple wavelengths and performing statistical analysis. Preliminary results are shown in Figure 7.1, in which normal Raman spectra and surface-enhanced Raman spectra for a DNA strand are shown.

Here, DNA strands of GACTGCGACCAACCTAGCCT is functionalized to a silver film and Raman spectra are acquired at excitation wavelengths of 488 nm, 514 nm, 633 nm, and 785 nm. The NRS spectra show consistent Raman signatures at each of the wavelengths. In contrast, the SERS spectra display significant differences with the different modes being enhanced or reduced as the excitation wavelength changes. However, these results are preliminary as I work to fabricate a uniformly smooth substrate and appropriately linearize the DNA. The fabrication process for ultra smooth silver films is being perfected, in which I use a germanium film to act as a

nucleation layer [137]. For the linearization of the DNA, I am looking at using the molecular combining process to extend and linearize the strands on the silver [138].

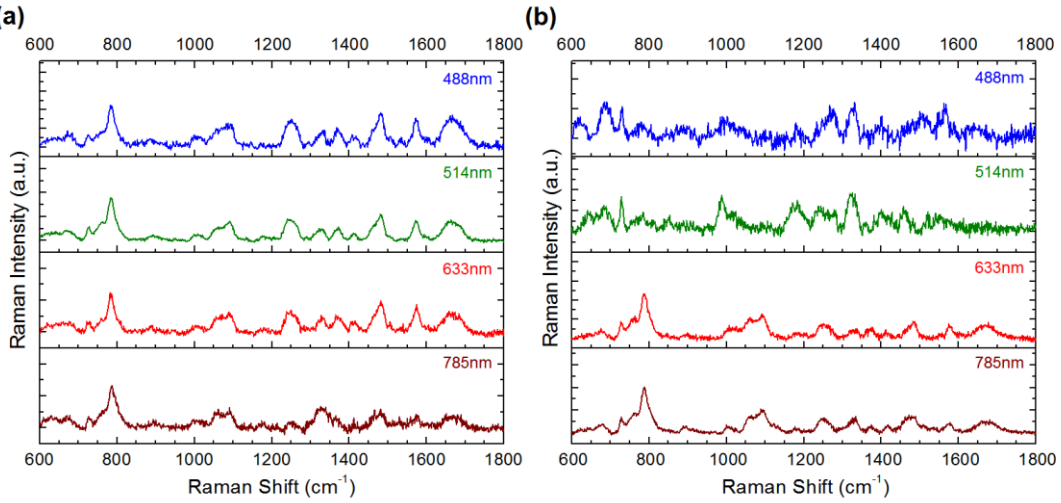

Figure 7.1. NRS and SERS of DNA strand. (a) Normal Raman spectra and (b) surface-enhanced Raman spectra of DNA strands at multiple excitation wavelengths.

7.3. Final Thoughts

As improvements and advancements are made for the field of plasmonics and surface-enhanced Raman spectroscopy, the chemical enhancement effect needs to be taken into account when analyzing Raman spectra. Particularly in the case of nucleic acid-silver composites, the static polarizability and charge-transfer effect have a strong impact on the resulting measurements. By fully understanding the impact the chemical enhancement effect has on the Raman signatures of nucleic acid-silver composites, additional information regarding nucleic acid composition of DNA strands can ideally be extracted from the Raman data as a label-free method.

Appendix

Table A.1. Raman modes of adenine. Experimental and calculated frequency modes (top row of each mode) and intensity ratios (bottom row of each mode) of adenine on multiple binding sites

Mode	Expt	N1	N3	N7	N9	NH_2
605-700 cm^{-1} def R5 (sqz group C5-N7-C8), R6 (sqz group C4-C5-C6, N1-C6-N10), rock NH_2	625	625-697	605-649	611-633	609-700	623-676
	0.0559	0.143	0.0892	0.0439	0.140	0.0352
678-779 cm^{-1} ring-breathing mode	721	710	678-779	713	708	716
	0.300	0.135	0.322	0.0890	0.354	0.196
777-935 cm^{-1} def R5 (sqz group N7-C8-N9, str C5-N7, C4-N9), R6 (sqz group N1-C2-N3), bend N9-H	899	886-935	853-921	777-796	890-914	819-854
	0.0303	0.0276	0.0211	0.0617	0.0239	0.00862
853-991 cm^{-1} wag C2-H, def R5 (sqz group N7-C8-N9)	940	921	938	853-991	940	908-974
	0.0559	0.0615	0.0857	0.133	0.0296	0.0915
969-1081 cm^{-1} rock NH_2, bend C2-H	1025	969	980-1081	1007-1040	993	997
	0.0224	0.00405	0.0147	0.0132	0.00575	0.0444
1003-1264 cm^{-1} str C6-N10, N3-C4, C4-N9, bend N9-H, C2-H, N10-H11, C8-H	1125	1003-1046	1198-1264	1051	1041-1073	1037-1110
	0.0687	0.0352	0.0485	0.0951	0.108	0.0671
1109-1306 cm^{-1} rock NH_2, str C5-N7, N1-C2, C2-N3, N7-C8, bend N9-H, C8-H	1248	1140	1306	1124-1259	1109-1165	1193-1219
	0.121	0.0439	0.0975	0.0494	0.0246	0.0372
1190-1349 cm^{-1} Str C2-N3, C5-N7, N1-C2, C5-C6	1310	1190-1235	1326	1301	1272-1332	1280-1349
	0.0288	0.114	0.0306	0.0411	0.105	0.131
1292-1416 cm^{-1} Str N1-C2, C6-N1, C4-C5, N3-C4, C5, N7, C8-N9, bend N9-H, C2-H, C8-H	1335	1292-1323	1342-1355	1340	1342	1416
	0.143	0.146	0.0327	0.207	0.0819	0.0134

Table A.1. Raman modes of adenine, continued

Mode	**Expt**	**N1**	**N3**	**N7**	**N9**	**NH_2**
1352-1491 cm^{-1} str C5-N7, C6-N10, N1-C2, C6-N1, C8-N9, N3-C4, bend C2-H, N9-H, N10-H12, C8-H	1370	1352-1388	1437-1475	1349-1424	1410-1430	1491
	0.0440	0.0284	0.0804	0.0470	0.0602	0.0430
1433-1572 cm^{-1} sciss NH_2, bend C2-H, N9-H, str C6-N10, C6-N1, C2-N3, N3-C4, C4-C5, C8-N9, N1-C2	1485	1433-1454	1545-1583	1463-1497	1511	1514-1572
	0.0967	0.225	0.173	0.0553	0.0199	0.0479
1524-1619 cm^{-1} sciss NH_2, str C6-N10, C5-C6	1600	1524-1592	1619	1559-1596	1567-1610	1591
	0.0335	0.0358	0.00528	0.0553	0.0469	0.357

Table A.2. Raman modes of cytosine. Experimental and calculated frequency modes (top row of each mode) and intensity ratios (bottom row of each mode) of cytosine on multiple binding sites

Mode	**Expt**	**N1**	**N3**	**NH_2**	**O**
636-810 cm^{-1} ring-breathing-mode	790	781	688-748	636-810	711-799
	0.358	0.232	0.264	0.220	0.257
858-959 cm^{-1} rock NH_2, str C2-N1, C2-N3	940	917-959	839-916	895-918	858-920
	0.0221	0.246	0.0242	0.0452	0.0393
975-1021 cm^{-1} def C5-H, C6-H, tor C5-C6	975	1014-1021	998	1018	998-1001
	0.0591	0.158	0.0560	0.0124	0.0266
1000-1110 cm^{-1} Bend C5-H, C6-H, tor C4-C5	1000	1075	1008	1029	1110
	0.0303	0.0498	0.0167	0.0444	0.0349
1100-1209 cm^{-1} bend C6-C5-H, str C6-N1	1112	1167	1100-1108	1164	1209
	0.0262	0.0128	0.0340	0.150	0.0589
1213-1265 cm^{-1} rock NH_2, bend N1-C6-H, str C6-N1	1248	1230-1265	1213-1261	1240	1261
	0.0720	0.0901	0.131	0.00773	0.234
1256-1351 cm^{-1} str C2-N3, str C4-NH_2	1290	1297	1343-1351	1256-1276	1341
	0.284	0.00707	0.229	0.0926	0.0430
1316-1452 cm^{-1} str C4-NH_2, bend C5-C6-H	1375	1368	1452	1316	1354
	0.0390	0.0507	0.190	0.0178	0.0103
1425-1448 cm^{-1} str C4-N3, C6-N1, C4-C5, bend C4-NH_2	1448	1425	-	1433	1442
	0.0302	0.0152	0	0.175	0.216
1464-1530 cm^{-1} Bend C2-O, str C4-NH_2, C4-N3, C5-C6, sciss NH_2	1530	1464	1470	1495	1470
	0.0215	0.0967	0.00448	0.224	0.0629
1481-1648 cm^{-1} sciss NH_2, str C2-O	1648	1507	1484	1516	1481
	0.0571	0.0420	0.0493	0.00953	0.0170

Table A.3. Raman modes of guanine. Experimental and calculated frequency modes (top row of each mode) and intensity ratios (bottom row of each mode) of guanine on multiple binding sites

Mode	**Expt**	**N1**	**N3**	**N7**	**N9**	**O**
646-696 cm^{-1} ring-breathing-mode	646	658	646-669	654-667	657-665	657-696
	0.408	0.130	0.375	0.291	0.227	0.164
692-797 cm^{-1} def N3-C2-N1, N1-C6-O	710	716-769	692-769	692-780	699-764	698-797
	0.0243	0.0252	0.0597	0.0421	0.0303	0.0398
839-907 cm^{-1} def C4-N9-C8	846	839-873	842-883	850-907	836-887	852-889
	0.0300	0.0127	0.0248	0.0187	0.0619	0.0321
937-1053 cm^{-1} def N7-C8-N9	937	958-1032	983-996	998-1028	963-991	966-1013
	0.103	0.0776	0.0558	0.0554	0.0319	0.0318
1045-1107 cm^{-1} str C2-N1, C2-N3, C2-NH_2	1047	1107	1018-1053	1072-1094	1045-1059	1082-1094
	0.0186	0.0113	0.0680	0.0177	0.0790	0.0152
1099-1224 cm^{-1} def C8-H	1185	1152	1083-1092	1220	1099	1224
	0.0364	0.0781	0.00686	0.0127	0.111	0.0339
1217-1268 cm^{-1} def N1-H, str C8-N7, C8-N9, C6-N1, C5-N7	1229	1255	1218	1266	1217-1255	1268
	0.110	0.191	0.0134	0.0304	0.0738	0.138
1261-1300 cm^{-1} def C8-H, str C8-N9, C5-C6, C4-N9, C6-N1	1261	1300	1264-1288	1279-1291	1273	1293
	0.0314	0.104	0.112	0.0308	0.0551	0.0839
1306-1360 cm^{-1} str C2-N1, C4-N3, C5-C6	1360	1327	1335	1331	1306	1328
	0.0430	0.0667	0.0487	0.0103	0.0280	0.0328
1360-1395 cm^{-1} str C4-N9, C5-N7, C8-N9	1384	1366	1392	1395	1360	1394
	0.0430	0.0196	0.0629	0.192	0.00444	0.200
1413-1442 cm^{-1} def N1-H, str C2-N3, C5-C6, C8-N9	1420	1417	1442	1431	1413	1423
	0.0309	0.0625	0.0318	0.00425	0.0439	0.0175

Table A.3. Raman modes of guanine, continued

Mode	**Expt**	**N1**	**N3**	**N7**	**N9**	**O**
1444-1494 cm^{-1} def C8-H, str C2-N1, C2-N3, C8-N7, C8-N9	1465	1457	1481	1494	1444	1491
	0.0308	0.138	0.00940	0.0736	0.0310	0.0503
1509-1570 cm^{-1} def N1-H, sciss NH_2, str C2-N2, C4-C5, C4-N9, C6-O, N3-C2, N3-C4	1548	1509-1553	1516	1531-1567	1522-1569	1531-1562
	0.0730	0.0707	0.0490	0.161	0.169	0.109
1583-1675 cm^{-1} sciss NH_2, str C2-N1, C2-N3	1675	1583	1570-1625	1592	1620	1586
	0.0178	0.0124	0.0826	0.0603	0.0532	0.0509

Table A.4. Raman modes of thymine. Experimental and calculated frequency modes (top row of each mode) and intensity ratios (bottom row of each mode) of thymine on multiple binding sites

Mode	**Expt**	**N1**	**N3**	**O2**	**O4**
603-690 cm^{-1} def C5-CH_3, wag CH_3	603	612	603-657	617	647-690
	0.0576	0.0329	0.0927	0.193	0.0848
708-756 cm^{-1} ring-breathing-mode	735	742	754	708-756	744
	0.179	0.156	0.254	0.128	0.0689
795-841 cm^{-1} def C5-C6-N1	795	808	799	783-841	788
	0.109	0.167	0.0780	0.111	0.0879
892-953 cm^{-1} bend C-O	927	940	905	916-953	892
	0.0319	0.0163	0.00312	0.0408	0.0493
944-1073 cm^{-1} def N1-C2-N3, str C5-C6	983	978-1001	988-1073	1017-1070	944-1053
	0.0690	0.0781	0.0284	0.0286	0.0525
1119-1200 cm^{-1} str C5-CH_3, C5-C6, C6-N1	1149	1119	1137-1142	1139	1126-1200
	0.0192	0.111	0.0371	0.0234	0.0321
1193-1262 cm^{-1} rock CH_3, tor CH_3	1238	1193-1228	1246	1209	1231-1262
	0.0222	0.0588	0.0416	0.0210	0.0725
1279-1349 cm^{-1} C5-CH_3	1348	1300-1326	1279-1337	1332-1344	1349
	0.202	0.172	0.0778	0.124	0.0598
1375-1429 cm^{-1} bend C5-CH_3, N3-H	1386	1385	1375	1389	1387-1429
	0.320	0.0297	0.0222	0.00841	0.0404
1391-1452 cm^{-1} bend C6-N1, rock CH_3	1403	1395	1391	1398	1452
	0.0354	0.0154	0.0442	0.00802	0.0703
1410-1493 cm^{-1} bend C5-CH_3	1458	1431-1452	1410	1424	1471-1493
	0.00935	0.0462	0.0653	0.103	0.0193
1457-1520 cm^{-1} def C5-C4-N3, wag CH_3	1475	1503	1458	1457	1520
	0.0158	0.0218	0.102	0.0253	0.0299
1464-1698 cm^{-1} str C2-O2	1656	1564-1601	1652	1629-1658	1607-1698
	0.218	0.0920	0.154	0.186	0.332

References

1. M. A. Cooper, "Optical biosensors in drug discovery," Nat. Rev. Drug Discov. **1**, 515–528 (2002).

2. D. Erickson, S. Mandal, A. H. J. Yang, and B. Cordovez, "Nanobiosensors: optofluidic, electrical and mechanical approaches to biomolecular detection at the nanoscale," Microfluid. Nanofluidics **4**, 33–52 (2008).

3. R. A. Tripp, R. A. Dluhy, and Y. Zhao, "Novel nanostructures for SERS biosensing," Nano Today **3**, 31–37 (2008).

4. A. S. Aricò, P. Bruce, B. Scrosati, J. M. Tarascon, and W. van Schalkwijk, "Nanostructured materials for advanced energy conversion and storage devices," Nat. Mater. **4**, 366–77 (2005).

5. X. Zhao, B. M. Sánchez, P. J. Dobson, and P. S. Grant, "The role of nanomaterials in redox-based supercapacitors for next generation energy storage devices," Nanoscale **3**, 839–55 (2011).

6. M. Deubel, G. von Freymann, M. Wegener, S. Pereira, K. Busch, and C. M. Soukoulis, "Direct laser writing of three-dimensional photonic-crystal templates for telecommunications," Nat. Mater. **3**, 444–7 (2004).

7. M. T. Harrison, S. V. Kershaw, M. G. Burt, A. L. Rogach, A. Kornowski, A. Eychmüller, and H. Weller, "Colloidal nanocrystals for telecommunications," Pure Appl. Chem. **72**, 295–307 (2000).

8. Z. Zhang, A. Weber-Bargioni, S. W. Wu, S. Dhuey, S. Cabrini, and P. J. Schuck, "Manipulating nanoscale light fields with the asymmetric bowtie nano-colorsorter," Nano Lett. **9**, 4505–9 (2009).

9. J. A. Schuller, E. S. Barnard, W. Cai, Y. C. Jun, J. S. White, and M. L. Brongersma, "Plasmonics for extreme light concentration and manipulation," Nat. Mater. **9**, 193–204 (2010).

10. P. F. Wright, E. Nilsson, E. M. Van Rooij, M. Lelenta, and M. H. Jeggo, "Standardisation and validation of enzyme-linked immunosorbent assay techniques for the detection of antibody in infectious disease diagnosis," Rev. Sci. Tech. **12**, 435–50 (1993).

11. R. A. Heller, M. Schena, A. Chai, D. Shalon, T. Bedilion, J. Gilmore, D. E. Woolley, and R. W. Davis, "Discovery and analysis of inflammatory disease-related genes using cDNA microarrays," Proc. Natl. Acad. Sci. **94**, 2150–2155 (1997).

12. S. A. Maier and H. A. Atwater, "Plasmonics: Localization and guiding of electromagnetic energy in metal/dielectric structures," J. Appl. Phys. **98**, 011101 (2005).

13. P. K. Jain, X. Huang, I. H. El-Sayed, and M. A. El-Sayed, "Review of Some Interesting Surface Plasmon Resonance-enhanced Properties of Noble Metal Nanoparticles and Their Applications to Biosystems," Plasmonics **2**, 107–118 (2007).

14. L. Pang, H. M. Chen, L. Wang, J. M. Beechem, and Y. Fainman, "Controlled detection in composite nanoresonant array for surface plasmon resonance sensing," Opt. Express **17**, 14700–9 (2009).

15. P. L. Stiles, J. a Dieringer, N. C. Shah, and R. P. Van Duyne, "Surface-enhanced Raman spectroscopy," Annu. Rev. Anal. Chem. (Palo Alto. Calif). **1**, 601–26 (2008).

16. S. Abalde-Cela, P. Aldeanueva-Potel, C. Mateo-Mateo, L. Rodríguez-Lorenzo, R. A. Alvarez-Puebla, and L. M. Liz-Marzán, "Surface-enhanced Raman scattering biomedical applications of plasmonic colloidal particles," J. R. Soc. Interface **7**, S435–50 (2010).

17. B. Han and E. Wang, "DNA-templated fluorescent silver nanoclusters," Anal. Bioanal. Chem. **402**, 129–38 (2012).

18. M. Fan, G. F. S. Andrade, and A. G. Brolo, "A review on the fabrication of substrates for surface enhanced Raman spectroscopy and their applications in analytical chemistry," Anal. Chim. Acta **693**, 7–25 (2011).

19. D. L. Jeanmaire and R. P. Van Duyne, "Surface raman spectroelectrochemistry," J. Electroanal. Chem. Interfacial Electrochem. **84**, 1–20 (1977).

20. M. G. Albrecht and J. A. Creighton, "Anomalously intense Raman spectra of pyridine at a silver electrode," J. Am. Chem. Soc. **99**, 5215–5217 (1977).

21. F. W. King, R. P. Van Duyne, and G. C. Schatz, "Theory of Raman scattering by molecules adsorbed on electrode surfaces," J. Chem. Phys. **69**, 4472 (1978).

22. K. Kneipp, Y. Wang, H. Kneipp, L. Perelman, I. Itzkan, R. Dasari, and M. Feld, "Single Molecule Detection Using Surface-Enhanced Raman Scattering (SERS)," Phys. Rev. Lett. **78**, 1667–1670 (1997).

23. S. R. Emory and S. Nie, "Screening and Enrichment of Metal Nanoparticles with Novel Optical Properties," J. Phys. Chem. B **102**, 493–497 (1998).

24. O. Lyandres, N. C. Shah, C. R. Yonzon, J. T. Walsh, M. R. Glucksberg, and R. P. Van Duyne, "Real-time glucose sensing by surface-enhanced Raman spectroscopy in bovine plasma facilitated by a mixed decanethiol/mercaptohexanol partition layer," Anal. Chem. **77**, 6134–9 (2005).

25. J. Gersten and A. Nitzan, "Electromagnetic theory of enhanced Raman scattering by molecules adsorbed on rough surfaces," J. Chem. Phys. **73**, 3023 (1980).

26. A. Otto, J. Timper, J. Billmann, and I. Pockrand, "Enhanced Inelastic Light Scattering from Metal Electrodes Caused by Adatoms," Phys. Rev. Lett. **45**, 46–49 (1980).

27. Q. Zhou, X. Li, Q. Fan, X. Zhang, and J. Zheng, "Charge transfer between metal nanoparticles interconnected with a functionalized molecule probed by surface-enhanced Raman spectroscopy," Angew. Chem. Int. Ed. Engl. **45**, 3970–3 (2006).

28. L. Xia, M. Chen, X. Zhao, Z. Zhang, J. Xia, H. Xu, and M. Sun, "Visualized method of chemical enhancement mechanism on SERS and TERS," J. Raman Spectrosc. **45**, 533–540 (2014).

29. N. Valley, N. Greeneltch, R. P. Van Duyne, and G. C. Schatz, "A Look at the Origin and Magnitude of the Chemical Contribution to the Enhancement Mechanism of Surface-Enhanced Raman Spectroscopy (SERS): Theory and Experiment," J. Phys. Chem. Lett. **4**, 2599–2604 (2013).

30. E. Cortés, P. G. Etchegoin, E. C. Le Ru, A. Fainstein, M. E. Vela, and R. C. Salvarezza, "Strong correlation between molecular configurations and charge-transfer processes probed at the single-molecule level by surface-enhanced Raman scattering," J. Am. Chem. Soc. **135**, 2809–15 (2013).

31. T. Vosch, Y. Antoku, J.-C. Hsiang, C. I. Richards, J. I. Gonzalez, and R. M. Dickson, "Strongly emissive individual DNA-encapsulated Ag nanoclusters as single-molecule fluorophores," Proc. Natl. Acad. Sci. U. S. A. **104**, 12616–21 (2007).

32. I. Díez and R. H. A. Ras, "Fluorescent silver nanoclusters," Nanoscale **3**, 1963–70 (2011).

33. A. P. de Silva, H. Q. N. Gunaratne, T. Gunnlaugsson, A. J. M. Huxley, C. P. McCoy, J. T. Rademacher, and T. E. Rice, "Signaling Recognition Events with Fluorescent Sensors and Switches," Chem. Rev. **97**, 1515–1566 (1997).

34. M. I. J. Stich, L. H. Fischer, and O. S. Wolfbeis, "Multiple fluorescent chemical

sensing and imaging," Chem. Soc. Rev. **39**, 3102–14 (2010).

35. A. Burns, P. Sengupta, T. Zedayko, B. Baird, and U. Wiesner, "Core/Shell fluorescent silica nanoparticles for chemical sensing: towards single-particle laboratories," Small **2**, 723–6 (2006).

36. S. W. Thomas, G. D. Joly, and T. M. Swager, "Chemical sensors based on amplifying fluorescent conjugated polymers," Chem. Rev. **107**, 1339–86 (2007).

37. L. Basabe-Desmonts, D. N. Reinhoudt, and M. Crego-Calama, "Design of fluorescent materials for chemical sensing," Chem. Soc. Rev. **36**, 993–1017 (2007).

38. J. P. Hare, H. W. Kroto, and R. Taylor, "Preparation and UV / visible spectra of fullerenes C60 and C70," Chem. Phys. Lett. **177**, 394–398 (1991).

39. G. V. Andrievsky, V. K. Klochkov, A. B. Bordyuh, and G. I. Dovbeshko, "Comparative analysis of two aqueous-colloidal solutions of C60 fullerene with help of FTIR reflectance and UV–Vis spectroscopy," Chem. Phys. Lett. **364**, 8–17 (2002).

40. R. Brause, H. Möltgen, and K. Kleinermanns, "Characterization of laser-ablated and chemically reduced silver colloids in aqueous solution by UV/VIS spectroscopy and STM/SEM microscopy," Appl. Phys. B Lasers Opt. **75**, 711–716 (2002).

41. R. E. Wrolstad, T. E. Acree, E. A. Decker, M. H. Penner, D. S. Reid, S. J. Schwartz, C. F. Shoemaker, D. Smith, and P. Sporns, *Current Protocols in Food Analytical Chemistry* (John Wiley & Sons, Inc., 2001).

42. W. Haiss, N. T. K. Thanh, J. Aveyard, and D. G. Fernig, "Determination of size and concentration of gold nanoparticles from UV-vis spectra," Anal. Chem. **79**, 4215–21 (2007).

43. H. W. Siesler, Y. Ozaki, S. Kawata, and H. M. Heise, *Near-Infrared Spectroscopy: Principles, Instruments, Applications* (John Wiley & Sons, 2008).

44. H. Büning-Pfaue, "Analysis of water in food by near infrared spectroscopy," Food Chem. **82**, 107–115 (2003).

45. Y. J. Chabal, "Surface infrared spectroscopy," Surf. Sci. Rep. **8**, 211–357 (1988).

46. K. Nakanishi, *Infrared Absorption Spectroscopy, Practical* (Holden Day, 1962).

47. K. Kneipp, H. Kneipp, I. Itzkan, R. R. Dasari, and M. S. Feld, "Ultrasensitive chemical analysis by Raman spectroscopy," Chem. Rev. **99**, 2957–76 (1999).

48. J. F. Li, Y. F. Huang, Y. Ding, Z. L. Yang, S. B. Li, X. S. Zhou, F. R. Fan, W. Zhang, Z. Y. Zhou, D. Y. Wu, B. Ren, Z. L. Wang, and Z. Q. Tian, "Shell-isolated nanoparticle-enhanced Raman spectroscopy," Nature **464**, 392–5 (2010).

49. S. Wachsmann-Hogiu, T. Weeks, and T. Huser, "Chemical analysis in vivo and in vitro by Raman spectroscopy--from single cells to humans," Curr. Opin. Biotechnol. **20**, 63–73 (2009).

50. Y. C. Cao, R. Jin, and C. A. Mirkin, "Nanoparticles with Raman spectroscopic fingerprints for DNA and RNA detection," Science **297**, 1536–40 (2002).

51. R. L. McCreery, *Raman Spectroscopy for Chemical Analysis* (John Wiley & Sons, 2005).

52. J. M. Chalmers and P. R. Griffiths, *Handbook of Vibrational Spectroscopy* (John Wiley & Sons, Ltd, 2006).

53. L. A. K. Staveley, *The Characterization of Chemical Purity: Organic Compounds* (Elsevier, 2013).

54. C. V. Raman, "A Change of Wave-length in Light Scattering," Nature **121**, 619–619 (1928).

55. C. V. Raman and K. S. Krishnan, "A New Type of Secondary Radiation," Nature **121**, 501–502 (1928).

56. D. S. Knight and W. B. White, "Characterization of diamond films by Raman spectroscopy," J. Mater. Res. **4**, 385–393 (2011).

57. P. V. Huong, "Structural studies of diamond films and ultrahard materials by Raman and micro-Raman spectroscopies," Diam. Relat. Mater. **1**, 33–41 (1991).

58. A. C. Ferrari, J. C. Meyer, V. Scardaci, C. Casiraghi, M. Lazzeri, F. Mauri, S. Piscanec, D. Jiang, K. S. Novoselov, S. Roth, and A. K. Geim, "Raman Spectrum of Graphene and Graphene Layers," Phys. Rev. Lett. **97**, 187401 (2006).

59. A. C. Ferrari, "Raman spectroscopy of graphene and graphite: Disorder, electron–phonon coupling, doping and nonadiabatic effects," Solid State Commun. **143**, 47–57 (2007).

60. F. Tuinstra, "Raman Spectrum of Graphite," J. Chem. Phys. **53**, 1126 (1970).

61. K. Larsson and R. P. Rand, "Detection of changes in the environment of hydrocarbon chains by raman spectroscopy and its application to lipid-protein systems," Biochim. Biophys. Acta - Lipids Lipid Metab. **326**, 245–255 (1973).

62. M. Fleischmann, P. J. Hendra, and A. J. McQuillan, "Raman spectra of pyridine adsorbed at a silver electrode," Chem. Phys. Lett. **26**, 163–166 (1974).

63. J. R. Lombardi, R. L. Birke, T. Lu, and J. Xu, "Charge-transfer theory of surface enhanced Raman spectroscopy: Herzberg–Teller contributions," J. Chem. Phys. **84**, 4174 (1986).

64. M. Fleischmann, P. J. Hendra, and A. J. McQuillan, "Raman spectra of pyridine adsorbed at a silver electrode," Chem. Phys. Lett. **26**, 163–166 (1974).

65. B. Giese and D. McNaughton, "Surface-Enhanced Raman Spectroscopic and Density Functional Theory Study of Adenine Adsorption to Silver Surfaces," J. Phys. Chem. B **106**, 101–112 (2002).

66. M. Muniz-Miranda, B. Pergolese, and A. Bigotto, "SERS and DFT study of nitroarenes adsorbed on metal nanoparticles," Vib. Spectrosc. **43**, 97–103 (2007).

67. T. Kang, S. M. Yoo, I. Yoon, S. Y. Lee, and B. Kim, "Patterned multiplex pathogen DNA detection by Au particle-on-wire SERS sensor.," Nano Lett. **10**, 1189–93 (2010).

68. M. J. Mulvihill, X. Y. Ling, J. Henzie, and P. Yang, "Anisotropic Etching of Silver Nanoparticles for Plasmonic Structures Capable of Single-Particle SERS," 895–901 (2010).

69. D. P. Fromm, A. Sundaramurthy, A. Kinkhabwala, P. J. Schuck, G. S. Kino, and W. E. Moerner, "Exploring the chemical enhancement for surface-enhanced Raman scattering with Au bowtie nanoantennas," J. Chem. Phys. **124**, 61101 (2006).

70. A. Smolyaninov, L. Pang, L. Freeman, M. Abashin, and Y. Fainman, "Broadband metacoaxial nanoantenna for metasurface and sensing applications," Opt. Express **22**, 22786–93 (2014).

71. J. B. Jackson, S. L. Westcott, L. R. Hirsch, J. L. West, and N. J. Halas, "Controlling the surface enhanced Raman effect via the nanoshell geometry," Appl. Phys. Lett. **82**, 257 (2003).

72. Y. Fang, N.-H. Seong, and D. D. Dlott, "Measurement of the distribution of site

enhancements in surface-enhanced Raman scattering," Science **321**, 388–92 (2008).

73. Y. Wang, H. Chen, S. Dong, and E. Wang, "Surface enhanced Raman scattering of p-aminothiophenol self-assembled monolayers in sandwich structure fabricated on glass," J. Chem. Phys. **124**, 74709 (2006).

74. S. Lee, H. Chon, M. Lee, J. Choo, S. Y. Shin, Y. H. Lee, I. J. Rhyu, S. W. Son, and C. H. Oh, "Surface-enhanced Raman scattering imaging of HER2 cancer markers overexpressed in single MCF7 cells using antibody conjugated hollow gold nanospheres," Biosens. Bioelectron. **24**, 2260–3 (2009).

75. K. Kneipp, M. Moskovits, and H. Kneipp, *Surface-Enhanced Raman Scattering*, Topics in Applied Physics, Vol. 103 (Springer Berlin Heidelberg, 2006).

76. H. Yamada, H. Nagata, K. Toba, and Y. Nakao, "Charge-transfer band and SERS mechanism for the pyridine-Ag system," Surf. Sci. **182**, 269–286 (1987).

77. J. E. Moore, S. M. Morton, and L. Jensen, "Importance of Correctly Describing Charge-Transfer Excitations for Understanding the Chemical Effect in SERS," (2012).

78. W.-H. Park and Z. H. Kim, "Charge transfer enhancement in the SERS of a single molecule," Nano Lett. **10**, 4040–8 (2010).

79. Y.-F. Huang, H.-P. Zhu, G.-K. Liu, D.-Y. Wu, B. Ren, and Z.-Q. Tian, "When the signal is not from the original molecule to be detected: chemical transformation of para-aminothiophenol on Ag during the SERS measurement," J. Am. Chem. Soc. **132**, 9244–6 (2010).

80. P. Hildebrandt and M. Stockburger, "Surface-enhanced resonance Raman spectroscopy of Rhodamine 6G adsorbed on colloidal silver," J. Phys. Chem. **88**, 5935–5944 (1984).

81. K. L. Kelly, E. Coronado, L. L. Zhao, and G. C. Schatz, "The Optical Properties of Metal Nanoparticles: The Influence of Size, Shape, and Dielectric Environment," J. Phys. Chem. B **107**, 668–677 (2003).

82. A. Gopinath, S. V. Boriskina, B. M. Reinhard, and L. Dal Negro, "Deterministic aperiodic arrays of metal nanoparticles for surface-enhanced Raman scattering (SERS)," Opt. Express **17**, 3741 (2009).

83. S. Wang, D. F. P. Pile, C. Sun, and X. Zhang, "Nanopin plasmonic resonator array and its optical properties," Nano Lett. **7**, 1076–80 (2007).

84. K.-H. Su, S. Durant, J. M. Steele, Y. Xiong, C. Sun, and X. Zhang, "Raman enhancement factor of a single tunable nanoplasmonic resonator," J. Phys. Chem. B **110**, 3964–8 (2006).

85. H. M. Chen, L. Pang, A. King, G. M. Hwang, and Y. Fainman, "Plasmonic coupled nanotorch structures leading to uniform surface enhanced Raman scattering detection," Nanoscale **4**, 7664–9 (2012).

86. K. Kneipp, H. Kneipp, V. Kartha, R. Manoharan, G. Deinum, I. Itzkan, R. Dasari, and M. Feld, "Detection and identification of a single DNA base molecule using surface-enhanced Raman scattering (SERS)," Phys. Rev. E **57**, R6281–R6284 (1998).

87. E. G. Gwinn, P. O'Neill, A. J. Guerrero, D. Bouwmeester, and D. K. Fygenson, "Sequence-Dependent Fluorescence of DNA-Hosted Silver Nanoclusters," Adv. Mater. **20**, 279–283 (2008).

88. W. Guo, J. Yuan, Q. Dong, and E. Wang, "Highly sequence-dependent formation of fluorescent silver nanoclusters in hybridized DNA duplexes for single nucleotide mutation identification," J. Am. Chem. Soc. **132**, 932–4 (2010).

89. C. Otto, T. van den Tweel, F. de Mul, and J. Greve, "Surface-enhanced Raman spectroscopy of DNA bases," J. Raman Spectrosc. **17**, 289–298 (1986).

90. E. T. Lagally, I. Medintz, and R. A. Mathies, "Single-Molecule DNA Amplification and Analysis in an Integrated Microfluidic Device," Anal. Chem. **73**, 565–570 (2001).

91. G. McNay, D. Eustace, W. E. Smith, K. Faulds, and D. Graham, "Surface-enhanced Raman scattering (SERS) and surface-enhanced resonance Raman scattering (SERRS): a review of applications," Appl. Spectrosc. **65**, 825–37 (2011).

92. M. Green, F.-M. Liu, L. Cohen, P. Kollensperger, and T. Cass, "SERS platforms for high density DNA arrays," Faraday Discuss. **132**, 269 (2006).

93. A. Barhoumi, D. Zhang, F. Tam, and N. J. Halas, "Surface-enhanced Raman spectroscopy of DNA," J. Am. Chem. Soc. **130**, 5523–9 (2008).

94. G. Shemer, O. Krichevski, G. Markovich, T. Molotsky, I. Lubitz, and A. B. Kotlyar, "Chirality of silver nanoparticles synthesized on DNA," J. Am. Chem. Soc. **128**, 11006–7 (2006).

95. S. Basu, S. Jana, S. Pande, and T. Pal, "Interaction of DNA bases with silver nanoparticles: assembly quantified through SPRS and SERS," J. Colloid

Interface Sci. **321**, 288–93 (2008).

96. J. S. Suh and M. Moskovits, "Surface-enhanced Raman spectroscopy of amino acids and nucleotide bases adsorbed on silver," J. Am. Chem. Soc. **108**, 4711–4718 (1986).

97. S. K. Kim, T. H. Joo, S. W. Suh, and M. S. Kim, "Surface-enhanced Raman scattering (SERS) of nucleic acid components in silver sol: Adenine series," J. Raman Spectrosc. **17**, 381–386 (1986).

98. J. Kundu, O. Neumann, B. G. Janesko, D. Zhang, S. Lal, A. Barhoumi, G. E. Scuseria, and N. J. Halas, "Adenine− and Adenosine Monophosphate (AMP)−Gold Binding Interactions Studied by Surface-Enhanced Raman and Infrared Spectroscopies," J. Phys. Chem. C **113**, 14390–14397 (2009).

99. E. Koglin, J.-M. Séquaris, J.-C. Fritz, and P. Valenta, "Surface enhanced raman scattering (SERS) of nucleic acid bases adsorbed on silver colloids," J. Mol. Struct. **114**, 219–223 (1984).

100. L. M. Freeman, A. Smolyaninov, L. Pang, and Y. Fainman, "Simulated Raman correlation spectroscopy for quantifying nucleic acid-silver composites," Sci. Rep. **6**, 23535 (2016).

101. S. K. Saikin, R. Olivares-Amaya, D. Rappoport, M. Stopa, and A. Aspuru-Guzik, "On the chemical bonding effects in the Raman response: benzenethiol adsorbed on silver clusters," Phys. Chem. Chem. Phys. **11**, 9401–11 (2009).

102. H.-S. Kim, D.-S. Ahn, S.-Y. Chung, S. K. Kim, and S. Lee, "Tautomerization of adenine facilitated by water: computational study of microsolvation," J. Phys. Chem. A **111**, 8007–12 (2007).

103. M. K. Shukla and J. Leszczynski, "Interaction of Water Molecules with Cytosine Tautomers: An Excited-State Quantum Chemical Investigation," J. Phys. Chem. A **106**, 11338–11346 (2002).

104. O. V. Shishkin, O. S. Sukhanov, L. Gorb, and J. Leszczynski, "The interaction of the most stable guanine tautomers with water," Phys. Chem. Chem. Phys. **4**, 5359–5364 (2002).

105. A. K. Chandra, M. T. Nguyen, and T. Zeegers-Huyskens, "Theoretical Study of the Interaction between Thymine and Water," J. Phys. Chem. A **102**, 6010–6016 (1998).

106. J. A. and J. E. P. and F. O. and M. B. and J. J. H. and E. B. and K. N. K. and V. N. S. and R. K. and J. N. and K. R. and A. R. and J. C. B. and S. S. I. and J. T. and M. C. and M. J. Frisch and G. W. Trucks and H. B. Schlegel and G. E.

Scuseria and M. A. Robb and J. R. Cheeseman and G. Scalmani and V. Barone and B. Mennucci and G. A. Petersson and H. Nakatsuji and M. Caricato and X. Li and H. P. Hratchian and A. F. Izmaylov, *Gaussian 09 Revision D.01* (Gaussian Inc., 2009).

107. J. Towns, T. Cockerill, M. Dahan, I. Foster, K. Gaither, A. Grimshaw, V. Hazlewood, S. Lathrop, D. Lifka, G. D. Peterson, R. Roskies, J. R. Scott, and N. Wilkins-Diehr, "XSEDE: Accelerating Scientific Discovery," Comput. Sci. Eng. **16**, 62–74 (2014).

108. A. D. Becke, "A new mixing of Hartree–Fock and local density-functional theories," J. Chem. Phys. **98**, 1372 (1993).

109. P. J. Hay and W. R. Wadt, "Ab initio effective core potentials for molecular calculations. Potentials for the transition metal atoms Sc to Hg," J. Chem. Phys. **82**, 270 (1985).

110. P. L. Polavarapu, "Ab initio vibrational Raman and Raman optical activity spectra," J. Phys. Chem. **94**, 8106–8112 (1990).

111. I. M. Alecu, J. Zheng, Y. Zhao, and D. G. Truhlar, "Computational Thermochemistry: Scale Factor Databases and Scale Factors for Vibrational Frequencies Obtained from Electronic Model Chemistries," J. Chem. Theory Comput. **6**, 2872–2887 (2010).

112. M. K. Kesharwani, B. Brauer, and J. M. L. Martin, "Frequency and zero-point vibrational energy scale factors for double-hybrid density functionals (and other selected methods): can anharmonic force fields be avoided?," J. Phys. Chem. A **119**, 1701–14 (2015).

113. V. Fournée, A. R. Rossa, T. A. Lograsso, and P. A. Thiel, "Orientation relationship between metallic thin films and quasicrystalline substrates," MRS Proc. **805**, LL8.3 (2003).

114. R. Gupta, M. J. Dyer, and W. A. Weimer, "Preparation and characterization of surface plasmon resonance tunable gold and silver films," J. Appl. Phys. **92**, 5264 (2002).

115. L. Zhao, L. Jensen, and G. C. Schatz, "Pyridine-Ag20 cluster: a model system for studying surface-enhanced Raman scattering," J. Am. Chem. Soc. **128**, 2911–9 (2006).

116. R. Huang, H.-T. Yang, L. Cui, D.-Y. Wu, B. Ren, and Z.-Q. Tian, "Structural and Charge Sensitivity of Surface-Enhanced Raman Spectroscopy of Adenine on Silver Surface: A Quantum Chemical Study," J. Phys. Chem. C **117**, 23730–

23737 (2013).

117. Y. Tantirungrotechai, K. Phanasant, S. Roddecha, P. Surawatanawong, V. Sutthikhum, and J. Limtrakul, "Scaling factors for vibrational frequencies and zero-point vibrational energies of some recently developed exchange-correlation functionals," J. Mol. Struct. Theochem. **760**, 189–192 (2006).

118. A. Papoulis, *The Fourier Integral and Its Applications* (McGraw-Hill, 1962).

119. M. Sun, S. Liu, M. Chen, and H. Xu, "Direct visual evidence for the chemical mechanism of surface-enhanced resonance Raman scattering via charge transfer," J. Raman Spectrosc. **40**, 137–143 (2009).

120. M. Sun, S. Wan, Y. Liu, Y. Jia, and H. Xu, "Chemical mechanism of surface-enhanced resonance Raman scattering via charge transfer in pyridine–Ag2 complex," J. Raman Spectrosc. **39**, 402–408 (2008).

121. R. Huang, L.-B. Zhao, D.-Y. Wu, and Z.-Q. Tian, "Tautomerization, Solvent Effect and Binding Interaction on Vibrational Spectra of Adenine–Ag+ Complexes on Silver Surfaces: A DFT Study," J. Phys. Chem. C **115**, 13739–13750 (2011).

122. D. P. Chong, *Recent Advances in Density Functional Methods* (World Scientific, 1995).

123. J. Andzelm and E. Wimmer, "Density functional Gaussian-type-orbital approach to molecular geometries, vibrations, and reaction energies," J. Chem. Phys. **96**, 1280 (1992).

124. L. Zhang, Y. Fang, and P. Zhang, "Experimental and DFT theoretical studies of SERS effect on gold nanowires array," Chem. Phys. Lett. **451**, 102–105 (2008).

125. T. R. Jensen, M. D. Malinsky, C. L. Haynes, and R. P. Van Duyne, "Nanosphere Lithography: Tunable Localized Surface Plasmon Resonance Spectra of Silver Nanoparticles," J. Phys. Chem. B **104**, 10549–10556 (2000).

126. G. J. Kovacs, R. O. Loutfy, P. S. Vincett, C. Jennings, and R. Aroca, "Distance dependence of SERS enhancement factor from Langmuir-Blodgett monolayers on metal island films: evidence for the electromagnetic mechanism," Langmuir **2**, 689–694 (1986).

127. R. Chhabra, J. Sharma, H. Wang, S. Zou, S. Lin, H. Yan, S. Lindsay, and Y. Liu, "Distance-dependent interactions between gold nanoparticles and fluorescent molecules with DNA as tunable spacers," Nanotechnology **20**, 485201 (2009).

128. B. J. Kennedy, S. Spaeth, M. Dickey, and K. T. Carron, "Determination of the Distance Dependence and Experimental Effects for Modified SERS Substrates Based on Self-Assembled Monolayers Formed Using Alkanethiols," J. Phys. Chem. B **103**, 3640–3646 (1999).

129. X. Zhang, J. Zhao, A. V Whitney, J. W. Elam, and R. P. Van Duyne, "Ultrastable substrates for surface-enhanced Raman spectroscopy: Al_2O_3 overlayers fabricated by atomic layer deposition yield improved anthrax biomarker detection," J. Am. Chem. Soc. **128**, 10304–9 (2006).

130. K. A. Willets and R. P. Van Duyne, "Localized surface plasmon resonance spectroscopy and sensing," Annu. Rev. Phys. Chem. **58**, 267–97 (2007).

131. J. A. Dieringer, A. D. McFarland, N. C. Shah, D. A. Stuart, A. V. Whitney, C. R. Yonzon, M. A. Young, X. Zhang, and R. P. Van Duyne, "Surface enhanced Raman spectroscopy: new materials, concepts, characterization tools, and applications," Faraday Discuss. **132**, 9 (2006).

132. W. A. Murray, J. R. Suckling, and W. L. Barnes, "Overlayers on silver nanotriangles: Field confinement and spectral position of localized surface plasmon resonances," Nano Lett. **6**, 1772–7 (2006).

133. J. F. John, S. Mahurin, S. Dai, and M. J. Sepaniak, "Use of atomic layer deposition to improve the stability of silver substrates for in situ, high-temperature SERS measurements," J. Raman Spectrosc. **41**, 4–11 (2010).

134. A. V Whitney, J. W. Elam, S. Zou, A. V Zinovev, P. C. Stair, G. C. Schatz, and R. P. Van Duyne, "Localized surface plasmon resonance nanosensor: a high-resolution distance-dependence study using atomic layer deposition," J. Phys. Chem. B **109**, 20522–8 (2005).

135. G. H. Chan, J. Zhao, G. C. Schatz, and R. P. Van Duyne, "Localized Surface Plasmon Resonance Spectroscopy of Triangular Aluminum Nanoparticles," J. Phys. Chem. C **112**, 13958–13963 (2008).

136. A. T. Zayak, H. Choo, Y. S. Hu, D. J. Gargas, S. Cabrini, J. Bokor, P. J. Schuck, and J. B. Neaton, "Harnessing Chemical Raman Enhancement for Understanding," J. Phys. Chem. Lett. **3**, 1357–1362 (2012).

137. Logeeswaran Vj, N. P. Kobayashi, M. S. Islam, W. Wu, P. Chaturvedi, N. X. Fang, S. Y. Wang, and R. S. Williams, "Ultrasmooth silver thin films deposited with a germanium nucleation layer," Nano Lett. **9**, 178–82 (2009).

138. A. Bensimon, A. Simon, A. Chiffaudel, V. Croquette, F. Heslot, and D. Bensimon, "Alignment and sensitive detection of DNA by a moving interface,"

Science **265**, 2096–2098 (1994).